UNIVERSITY of CALIFORNIA
Santa Barbara

Preserving entanglement during weak measurement demonstrated with a violation of the Bell-Leggett-Garg inequality

A dissertation submitted in partial satisfaction of the
requirements for the degree of

Doctor of Philosophy

in

Physics

by

Theodore C. White

Committee in charge:

Professor John Martinis, Chair
Professor Mark Sherwin
Professor Wim van Dam

September 2015

The dissertation of Theodore C. White is approved:

Professor Mark Sherwin

Professor Wim van Dam

Professor John Martinis, Chair

September 2015

Acknowledgements

To all my family who supported me. To all my friends who kept me sane. To all my lab mates who were there with me in the trenches. Thanks you all, and I couldn't have done it without you.

Curriculum Vitæ

Theodore C. White

Education

(2015) Ph.D., Physics, University of California Santa Barbara

(2010) B.S.

(2006) highschool

First author publications

"Design and characterization of a lumped element single-ended superconducting microwave parametric amplifier with on-chip flux bias line", Josh Mutus, Ted White, et al. *Appl. Phys. Lett.* 103, 122602 (2013)

"Strong environmental coupling in a Josephson parametric amplifier", Josh Mutus, Ted White, et al. *Appl. Phys. Lett.* 104, 263513 (2014)

"Traveling wave parametric amplifier with Josephson junctions using minimal resonator phase matching ", Ted White, Josh Mutus et al. *Appl. Phys. Lett.* 106, 242601 (2015)

"Violating the Bell-Leggett-Garg inequality with weak measurement of an entangled state", Ted White, Josh Mutus et al. *submitted* (2015)

Abstract

Preserving entanglement during weak measurement demonstrated with a violation of the Bell-Leggett-Garg inequality

by

Theodore C. White

Quantum mechanics makes many predictions, such as superposition, projective measurement, and entanglement, which defy classical intuition. For many years it remained unclear if these predictions were real physical phenomena, or the result of an incomplete understanding of hidden classical variables. For quantum entanglement, the Bell inequality provided the first experimental bound on such hidden variable theories by considering correlated measurements between spatially separated photons. Following a similar logic, the Leggett-Garg inequality provides an experimental test of projective measurement by correlating sequential measurements of the same object. More recently, these inequalities have become important benchmarks for the "quantumness" of novel systems, measurement techniques, or methods of generating entanglement. In this work we describe a continuous and controlled exchange of extracted state information and two-qubit entanglement collapse, demonstrated using the hybrid Bell-Leggett-Garg inequality. This effect is quantified by correlating weak measurement results with subsequent projective readout to collect all the statistics of a Bell inequality experiment in a single quantum circuit. This result was made possible by technological ad-

vances in superconducting quantum processors which allow precise control and measurement in multi-qubit systems. Additionally we discuss the central role of superconducting Josephson parametric amplifiers, which are a requirement for high fidelity single shot qubit readout. We demonstrate the ability to measure average Bell state information with minimal entanglement collapse, by violating this hybrid Bell-Leggett-Garg inequality at the weakest measurement strengths. This result indicates that it is possible to learn about the dynamics of large entangled systems without significantly affecting their evolution.

Contents

Chapter 1

The strange predictions of quantum mechanics

1.1 Introduction

At the start of the 20th century, improvements in experimental technology began to reveal strange phenomena at the atomic level. This bizarre behavior, which seemed to have no classical explanation, led to the development of quantum mechanics. Quantum mechanics has since become arguably the most accurate and precise theoretical description of reality ever. Despite this success, questions persist about the physical interpretations of some of the most fundamental aspects of quantum mechanics. This is of particular concern in the field of quantum computing, which depends on this uniquely quantum behavior scaling to larger and more complicated systems. The last 20 years has seen great strides in quantum computing technology

with increases in system size, qubit control, and operation fidelity. Fortunately, the qualities necessary in an advanced quantum processor also make it an excellent setup to test fundamental predictions of quantum mechanics.

1.2 Measurement and entanglement

The counter-intuitive predictions of quantum mechanics, such as measurement back action or long range entanglement, lead some to question the completeness of the theory. Perhaps these predictions were simply artifacts of an otherwise useful mathematical model rather than predictions of reality. Quantum mechanics might then be obscuring a classical theory of undetermined or "hidden" variables, that would be discovered with improved measurements or theoretical understanding.

1.2.1 Superposition and projection

A key difference between classical and Quantum mechanics is the function of measurement. To understand this difference it is helpful to consider a two level system (0 or 1) and the difference between a classical bit and a quantum bit (qubit). In classical mechanics the only function of measurement is to determine that state. Even probabilistic measurements assume the system is in the measured state before any measurement has been performed. For such a system it is usually possible, with a cleverly designed measurement, to determine if the bit is a 0 or 1 without changing that result. This means one can say with confidence that if a 0 is measured it was because the system was in state 0 and remains in that state. Subsequent measurements

of the same system should continue to produce the same result until something changes the system in a deterministic way.

In quantum mechanics the system can exist in the quantum states $|0\rangle$ or $|1\rangle$, as well a superposition of these states $|\Psi\rangle = \alpha|0\rangle + \beta|1\rangle$, where $|\alpha|^2 + |\beta|^2 = 1$. When strongly measuring a superposition state $|\Psi\rangle$, the result will indicate 0 with a probability $|\alpha|^2$ and 1 with a probability of $|\beta|^2$. In addition, if the result is 0, then a second measurement of the same system will also results in 0 and vice versa. If the system starts in a superposition state $|\Psi\rangle$, the interpretation of quantum mechanics is that the act of measuring the state projects it into either $|0\rangle$ or $|1\rangle$.

1.2.2 Entanglement

An equally unintuitive prediction of quantum mechanics is that of entanglement between spatially separated qubits. Entanglement is the result of two qubits existing in a state that is more than the sum of its parts. Given two qubits q_1 and q_2, we can describe each state individually as $|\Psi_1\rangle = \alpha_1|0\rangle + \beta_1|1\rangle$ and $|\Psi_2\rangle = \alpha_2|0\rangle + \beta_2|1\rangle$. The combined state for these two qubits can then be described as

$$\begin{aligned} |\Phi\rangle &= |\Psi_1\rangle \otimes |\Psi_2\rangle \\ &= \alpha_1\alpha_2|00\rangle + \alpha_1\beta_2|01\rangle + \alpha_2\beta_1|10\rangle + \beta_1\beta_2|11\rangle. \end{aligned} \tag{1.1}$$

The fact that we can describe the two qubit state $|\Phi\rangle$ as a product of two single qubit states means that it is separable. In contrast, an entangled state such as $|\Phi\rangle = 1/\sqrt{2}\,(|00\rangle + |11\rangle)$ is not separable. If one were to measure either qubit the result would be evenly split between $|0\rangle$ and $|1\rangle$, but if either qubit is $|0\rangle$ then both qubits are $|0\rangle$ and if either qubit is $|1\rangle$ they are both

$|1\rangle$. The state can only be properly understood a single state which happens to include two qubits. Interestingly, there is no length or time dependence to this entanglement. One could theoretically pull two entangled qubits to opposite sides of the universe and a measurement of either qubit would have an instantaneous effect on the other. In this case, the projective wemeasurement breaks the entanglement as both $|00\rangle$ and $|11\rangle$ can be described as two single qubit states. It was this seemingly impossible action at a distance [1] which led many to believe entanglement was simply the artifact of an incomplete model, with no realistic physical interpretation.

1.3 Inequality measurements

For many years discussions on the nature of projective measurement or entanglement were more philosophy than science. The Bell inequality (BI) [2] provided the first quantitative test to distinguish between quantum entanglement and a yet undiscovered classical hidden variable theory. The core assumption of a Bell inequality is that the measurements of two spatially separated objects cannot affect one another. Bell designed a test for this locality assumption (which was later refined by Clauser, Horne, Shimony, and Holt into an inequality (CHSH) [3]) involving correlated polarization measurements with varying rotation angles between two spatially separated photons. The angle of the polarizer sets the basis for each measurement and allows correlations to be measured in multiple different bases. Entangled photons exhibit stronger correlations across these different bases than what is possible classically, and can violate the inequality.

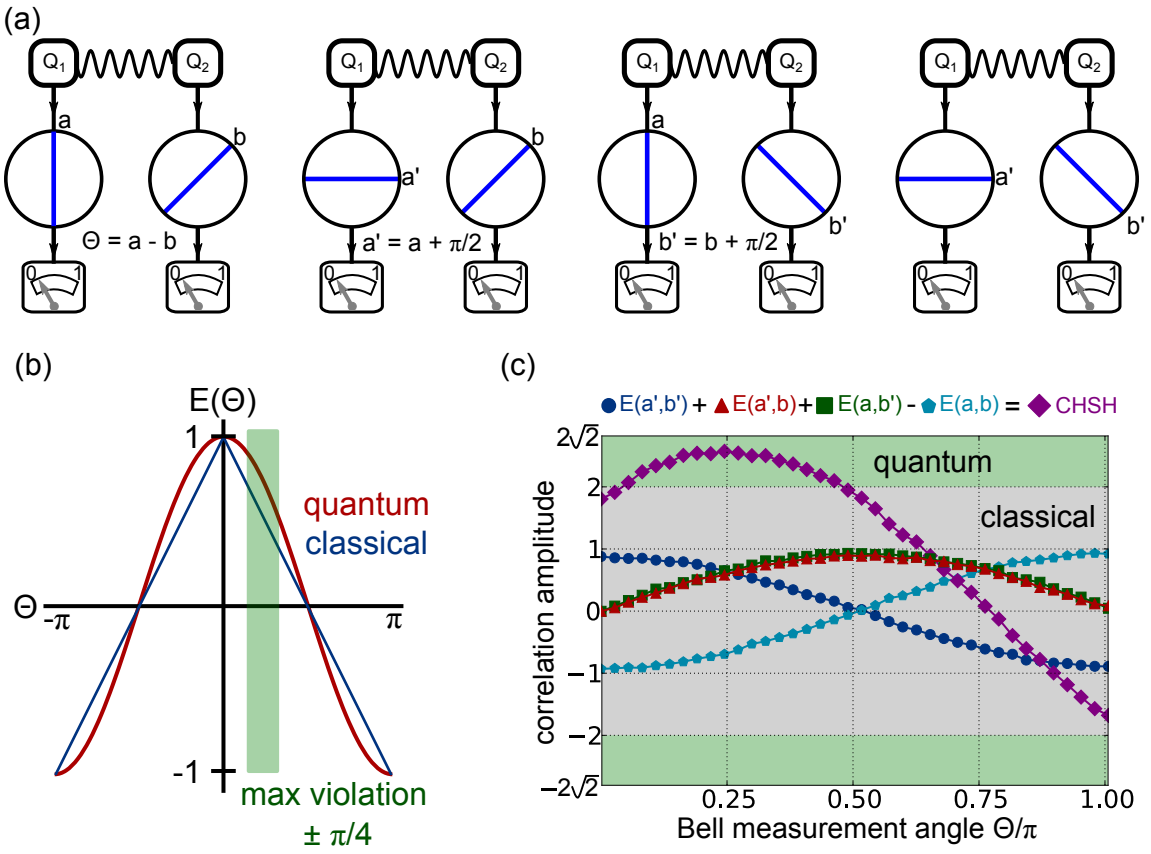

Figure 1.1: Entanglement and the CHSH corralator. (a) Schematic of a typical CHSH experiment. Two qubits are prepared in a maximally entangled Bell state and measurements are conducted at various measurement angles a, b, $a' = a + \pi/2$, and $b' = b + \pi/2$. (b) Dependence of correlation amplitude (Eq. 1.2) on detector angle difference $\theta = a - b$. The difference between quantum and classical correlation is maximized at $\theta = \pi/4$. (c) Measurement data of CHSH correlator using superconducting qubits prepared in a $|\Phi^+\rangle$ Bell state, displaying sinusoidal dependence on the relative measurement angle θ.

The CHSH correlator, designed by Clauser, Horne, Shimony, and Holt [3] as a refinement of the Bell inequality, provides a direct quantitative bound on classical hidden variable theories using correlated measurements between two spatially separated qubits. The correlator combines four different experimental configurations because it can be difficult to tell the difference between potentially classical (un-entangled) qubits and an entangled state in only one basis. The measurement basis can be set in different ways depending on the system being used. In

the first experimental realization of the CHSH correlator [4] the entangled state consisted of polarized photons pairs and the measurement basis was set by rotating polarized filters.

We can extend this idea to a general qubit system by using qubit rotations to map the measurement basis onto the ground ($|0\rangle$) and excited ($|1\rangle$) states of the system. For measurement rotations a (qubit 1) and b (qubit 2), shown in Fig. 1.1(a), the correlation amplitude is given by

$$E(a,b) = P(00) - P(10) - P(01) + P(11), \tag{1.2}$$

where P(00) is the probability both qubits are in the ground state. Given this equation however, we can see that both the Bell state $|\Phi^+\rangle = (|00\rangle + |11\rangle)/\sqrt{2}$ and the prepared state $|00\rangle$ will have a correlation amplitude of 1 if $a = b = 0$. The difference only becomes clear when many different detector angles are considered. The behavior of $E(a,b)$ *vs.* detector rotation, described here as $\theta = a - b$, is shown in Fig. 1.1(b) for both the classical and quantum case. If the orientations of the bits is classically predetermined, then for an average over the correlations for all possible values of a and b E would at most have a linear dependence on θ. Quantum mechanically E has a sinusoidal dependence on θ, who's magnitude depends on both a and b. Specifically in the case of an entangled pair, E has the same sinusoidal dependence for any value of a and b, with with the maximum difference occurring at odd multiples of $\theta = \pi/4$ [2].

When conducting a traditional CHSH experiment, the relative measurement angles for each qubit are held fixed such that $a' = a + \pi/2$ and $b' = b + \pi/2$. To collect the data, shown in Fig. 1.1(c), $\theta = a - b$ was varied from 0 to π, and each individual correlator was measured separately along with the sum given by

$$\text{CHSH} = E(a,b) + E(a',b) + E(a,b') - E(a',b'). \tag{1.3}$$

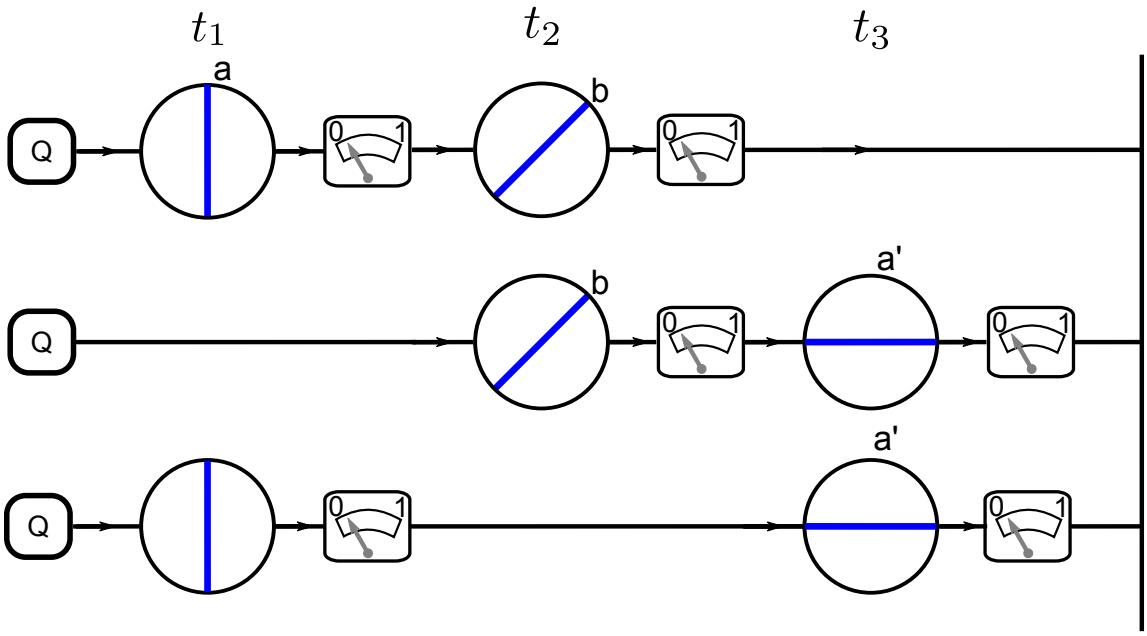

Figure 1.2: Leggett-Garg inequalities. (a) Schematic of an ideal LGI experiment. In this case a single qubit is measured in different bases at times $t_1 < t_2 < t_3$ in different combinations to construct the full LGI correlator. Like the Bell inequality the sum of these correlations is bounded for a classical system.

For any two classical states measured at these angles, we should see a linear dependence for each $E(\theta)$ and a bound on the the CHSH correlator of $|CHSH| \leq 2$. Alternately, if the two qubits are in a maximally entangled Bell state we should see sinusoidal behavior for $E(\theta)$ and a maximum CHSH value of $2\sqrt{2}$. The data, shown in Fig. 1.1(c), display the expected sinusoidal dependence for each individual term, with a maximum CHSH amplitude near $\theta = \pi/4$. While this data shows a robust violation of the classical bound, it fails to reach the theoretical maxium bound of $2\sqrt{2}$. The maximum CHSH amplitude of ~ 2.5 we see here is due to experimental imperfections, which are system dependent.

1.3.1 The Leggett-Garg inequality

Part of the reason why quantum mechanics is so unintuitive is that we don't often observe coherent quantum behavior in large systems. While unlikely to occur in larger systems, it is unclear if there is a scale at which coherent behavior is no longer possible. The Leggett-Garg inequality (LGI) [5] was developed to investigate the quantumness of a larger objects, like macroscopic phase of the SQUID. The LGI is similar to a Bell inequality but involves measurements separated in time rather than in space. Classical theories of measurement assume that the system is always in a definite state, and that an ideal measurement will not change the state of the system. In contrast, if one were to prepare a quantum state in one basis and measure it in a different measurement basis, the act of measurement would project that object into an eigenstate of the new basis. To distinguish one kind of system from the other, measurements are conducted in different bases at different times. For measurements conducted at times $t_1 < t_2 < t_3$, we can construct correlators analogous to Eq. 1.2 but for different measurements of the same qubit,

$$E(t_i, t_j) = P(00) - P(10) - P(01) + P(11). \tag{1.4}$$

The inequality was originally composed of three distinct experiments, shown in Fig. 1.2(a). In the first experiment, the system measured projectively at time t_1, followed by a final projective measurement at time t_3. A second experiment is then carried out where an intermediate measurement in a different basis is conducted at time t_2 instead of time t_3. The third experiment consists of only the measurements at times t_2 and t_3. The LGI is then given by

$$E(t_1, t_2) + E(t_2, t_3) - E(t_1, t_3) \leq 1 \tag{1.5}$$

where $E(t_1, t_3)$ is the experiment in which no measurement is performed at time t_2. Further details for LGIs can be found in the review article by Emary *et al.* [6].

1.4 Experimental loopholes

While there is a great deal of experimental evidence for the violation of Bell's inequality, this data is often questioned on the basis of experimental loopholes [7]. One such loophole is based on the assumption of locality. This locality assumption, fundamental to any Bell inequality, presumes no classical interactions between remote qubits occur during the correlation measurements. In some experiments, the close proximity of adjacent detectors or qubits means this interaction cannot be ruled out. Thus, behavior that appears to be quantum could, at least in principle, be the result of a fast classical interaction between hidden variables in the system. Photon systems, such as those used in the original CHSH [4], are ideal for avoiding local-

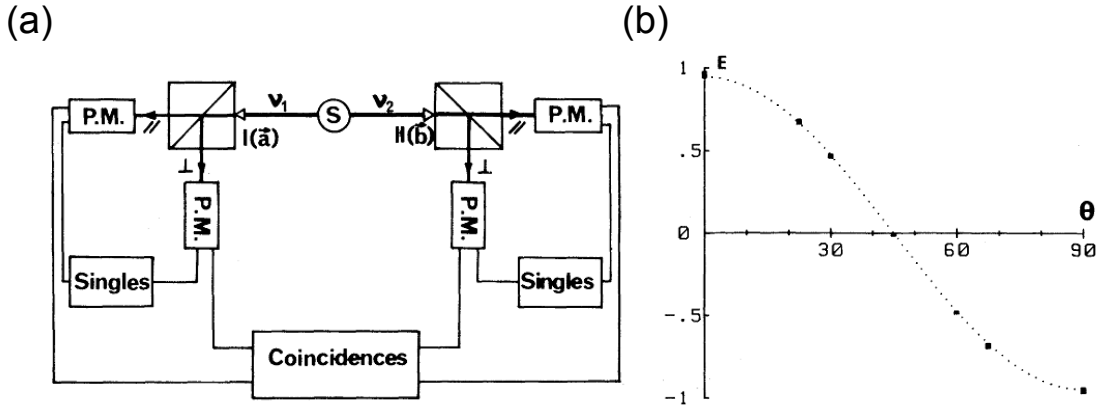

Figure 1.3: Figures of original CHSH experiment taken from reference [4]. (a) Schematic of the experiment involving entangled photons and polorometers which transmit or reflect a photon based on its linear polarization. The results of Photon detectors are correlated to measure the terms E(a,b) for each iteration of the experiment (b) Sinusoidal dependence of Eq. 1.2 on relative angle θ demonstrated by photons in the CHSH experiment.

ity because the coherence length of photons in air or optical fibers is very large[8]. In this case polarization is used as the measurement variable and entangled photons are prepared in a superposition of polarization states. In the experiment, shown in Fig 1.3 (a), the photons eventually reach polarimeters in which vertically polarized photons are transmitted and horizontally polarized photons are reflected depending on the relative angle of the polarimeter. The four detectors then measure which combination detection events occurred. The correlation amplitudes, shown in Fig 1.3 (b), also depend sinusoidally on θ, which in this case is the relative polarizer angle.

There are however, still several problems with optical CHSH experiments. The information for each experiment is carried by a single pair of photons. In many cases the polarimeters and photo detectors are lossy, and can absorb one or both photons before they can be measured. It is often the case that only a small fraction of the total emitted photons are successfully detected. To trust an observed violation, one must be certain that the subset of successful experiments used to measure the CHSH correlator evenly samples the full ensemble. It is possible that bias in a lossy detector could lead one to preferentially collect samples with the desired correlation and discard those without, leading to the fair sampling loophole[9]. If this same detector inefficiency is dependent on measurement basis (polarizer angle), different experiments would be measuring incompatible ensembles. Correlations between such separate classical ensembles could conceivably produce a false violation of the inequality, known as the disjoint sampling loophole[10].

The LGI is subject to the same detector inefficiency loopholes as a Bell inequality, but

there is an additional and more troubling assumption. This assumption is that the intermediate measurement has no classical effect on the state. If the intermediate measurement at t_2 were sufficiently invasive it could affect the measurement at t_3 in the same way a projective measurement affects a quantum system. In this case the classical measurement would simply be perturbing the system through the action of a hidden variable theory just as in the locality loophole. As it is difficult to measure the level of "invasiveness" in such hidden variable theories, this so called clumsiness loophole [11] is difficult to avoid completely.

1.5 Conclusion

The inequalities as detailed were originally conceived of as tests for the validity of quantum theory. As the evidence for quantum mechanics grows more overwhelming, these tests have begun to fill a different role. More modern implementations of both inequalities have been used as verification that a system is behaving quantum mechanically. For instance a violation of the Leggett-Garg inequality could be used to verify a new method method of state measurement. Similarly a violation of bells inequality provides evidence that an entangling gate is in fact entangling. It is this method of validation through violation that we are interested in for this work.

Chapter 2

The Bell-Leggett-Garg inequality

The power of a Bell or Leggett-Garg inequality is that it provides a fundamental physical test of quantum mechanics. A violation of the inequality is ideally possible only if a system behaves in a uniquely quantum way. As such, these experiments are valuable as benchmarks for new systems which might display quantum behavior. Inequality violations have become particularly useful in the world of quantum information, where they can be used to benchmark novel methods of entanglement or measurement. This is perhaps best exemplified by the use of weak measurement in the Leggett-Garg inequality.

2.1 Weak measurement

The standard conception of measurement is that a projection operator measures the state and projects the qubit onto a state in the measurement basis. This can also be thought of as a dephasing process, in which the coherent state $|\Phi\rangle = (|0\rangle + |1\rangle)/\sqrt{2}$ devolves to an probabilistic

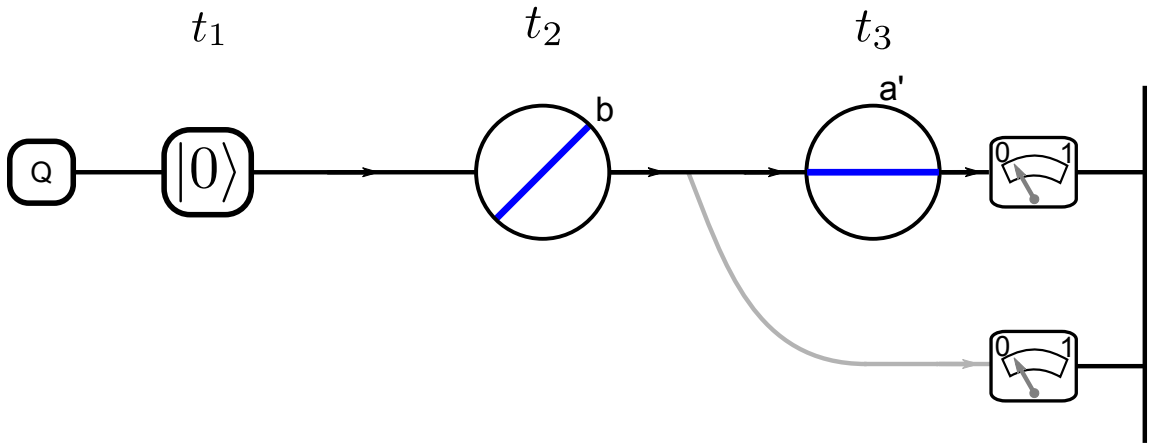

Figure 2.1: Leggett-Garg inequality conducted using weak measurement. The initial measurement is replaced with preparation into a known state. The second measurement is a weak measurement which measures the state with minimal back-action. The final measurement is fully projective readout which measures the final state of the system. This allows all the statistics of an LGI to be collected in a single experimental preparation.

mix of $|0\rangle$ and $|1\rangle$. The magnitude of this effect however, is largely dependent on the method of measurement. In some measurements, the coupling of qubit state to detector can be continuously varied from full projective readout to no readout at all. Turning down the strength of the measurement until the result is only weakly correlated to the qubit state is the basis of weak measurement [12, 13, 14]. These weak measurements are characterized by partial projection operators, which have a strength dependent dephasing effect on the state being measured. Recently this has lead to ground breaking experiments mapping the evolution of single qubit trajectories on the Bloch sphere [15, 16].

Perhaps the most ubiquitous use of weak measurement has been in the violation of Legget-Garg inequalities. This weak measurment LGI, shown in Fig. 2.1, replaces the initial measurement with preparation in a known state at time t_1, followed by a weak measurement at time t_2, and finally fully projective readout at time t_3. As the measurement at time t_2 only

partially projects the state, the correlations for the entire LGI can be measured with only one experimental configuration. This means that the effect from the measurement at time t_2 is always present, eliminating preparation dependent bias in the LGI. Additionally, the weakness of the measurement makes it less likely a classical perturbation is affecting the state in some unknown way. This ideally makes the LGI less susceptible to the clumsy measurement loophole [11] discussed in the previous chapter. Since its initial proposal, the weak measurement LGI has become the standard LGI experiment being conducted across both optical and solid state systems [17, 18, 19, 20, 21, 22, 23, 6].

While the theoretical description of weak measurement is unique, the implementation can vary greatly in different experimental systems. In superconducting qubits readout is often accomplished through a dispersive interaction between the qubit and a resonator [24]. In this case the measurement strength depends on the number of photons used to probe the resonator. In optical systems, often ancilla photons are used to weakly couple to the photon polarization being measured [21, 22]. Similarly, in superconducting qubits ancilla qubits can be weakly entangled with the qubit being measured through a variable strength C-NOT gate [23]. The various implementations are shown in Fig. 2.2.

Just as the Bell violation can be used to judge the fidelity of an entangling operation, the LGI is an excellent way to evaluate the fidelity of a weak measurement protocol. In this case a violation of the LGI requires both that the measurement extracts the desired state information, and that it minimized the back action to the point predicted by partial projection operators. Thus the LGI acts as a benchmark for the effect of measurement on a single qubit.

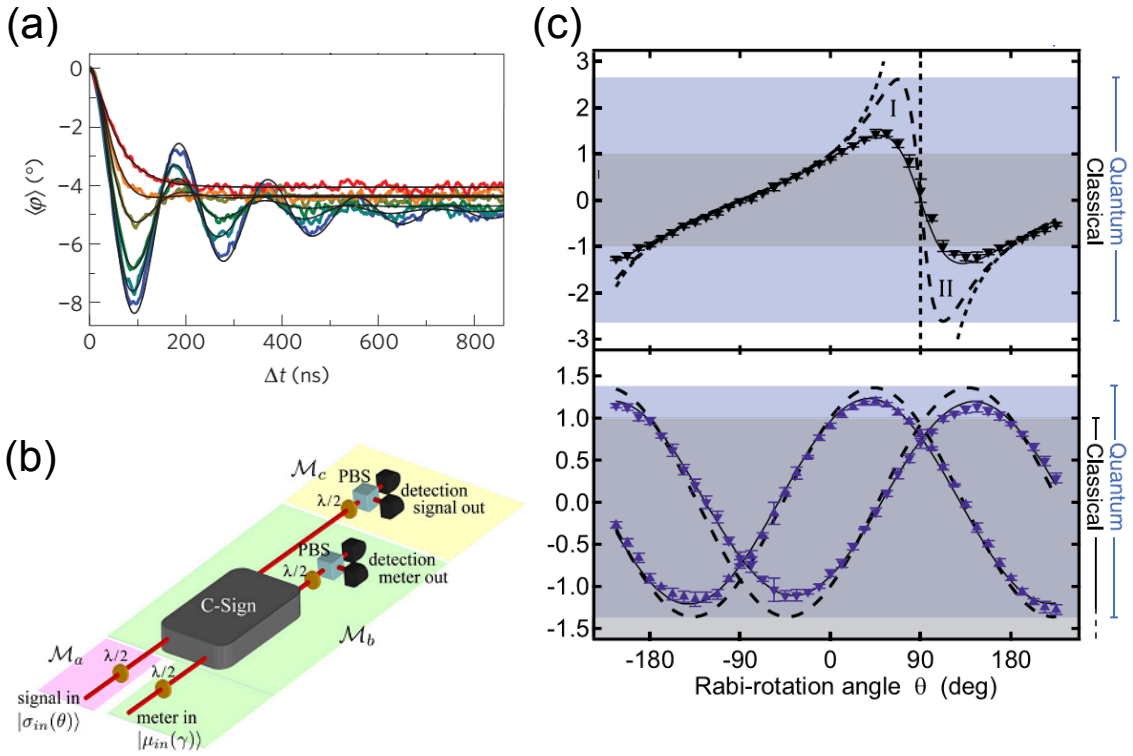

Figure 2.2: Exammples of weak measurements used in various Leggett-Garg inequalities. (a) Figure reproduced from Ref. [20] showing amplitude of driven Rabi oscillations $\langle\phi\rangle$ vs time for a superconducting qubit coupled to a resonator being probed with n = 0,1,2,5,10 and 20 photons respectively. As the photon number increases so does the dephasing of the transmon. (b) Figure reproduced from Ref. [21] showing ancilla weak measurement in optical systems, where the polarization of the photon being measured is weakly coupled to that of an ancilla photon. (c) Figure reproduced from Ref. [23] showing a violation of the LGI for a superconducting qubit system using ancilla qubit weak measurement. The above graph shows the behavior of the post selected "weak values" while the lower graph shows the LGI correlator vs rotation angle for the intermediate measurement bases.

2.2 Combining measurement and Entanglement

While the weak measurements discussed in the previous section are unlikely to perturb the state in an unknown way, the issue of the clumsy measurement loophole was never fully addressed. Without knowing the behavior of a "hidden variable" in the system, it is impossible to known the magnitude of the effect of measurement. In an attempt to further avoid clumsy

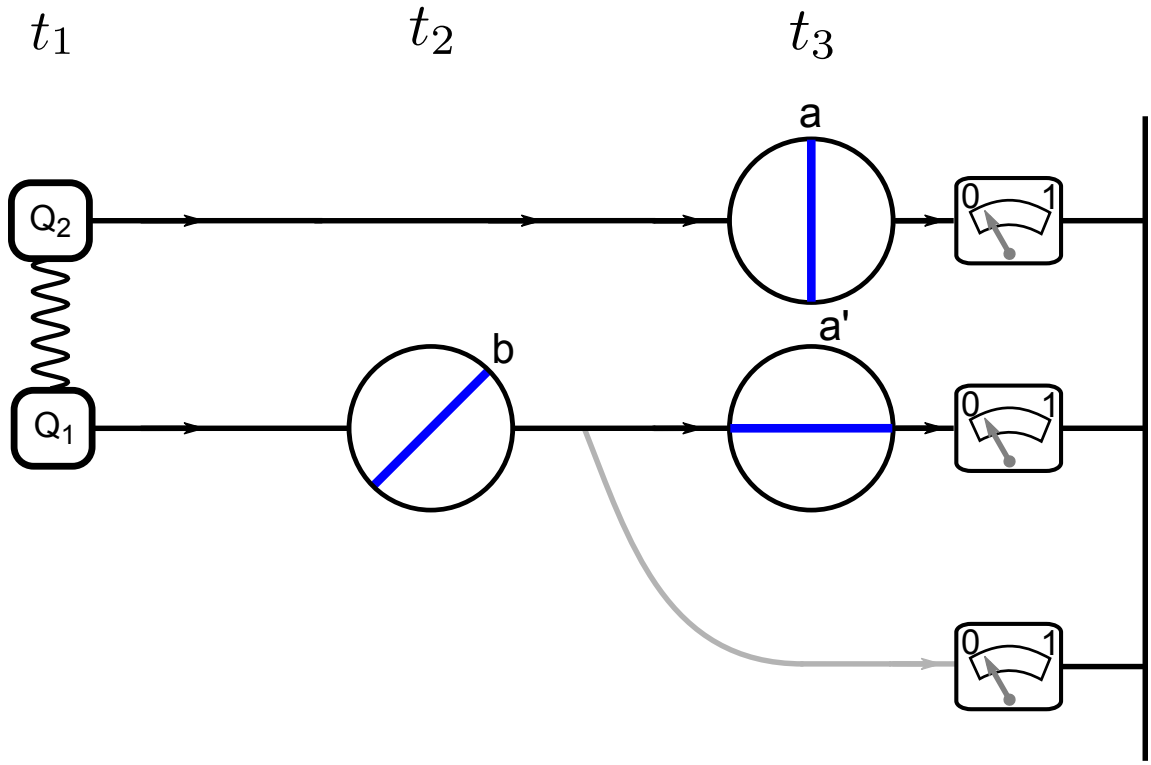

Figure 2.3: Leggett-Garg inequality in which the initial state prepared consists of two qubits in a bell state. A weak intermediate measurement is conducted on only one qubit of the bell pair. The weak measurement result of the one qubit is then correlated to the projective readout of both Bell qubits based. This allows the weak measurement process to be isolated from the qubit being projectively read out via the entanglement of the bell state.

measurements, it was suggested that the the single qubit of the LGI could be replaced with a Bell pair [22]. This protocol, show in Fig. 2.3, isolates the affect of the weak measurement to just one qubit in the Bell Pair. As the effects of measurement should be translated by the entanglement of the Bell pair, the necessary statistics can be still be correlated to violate an LGI [22]. By including a spatial separation between the two Bell qubits, the assumption that the weak measurement is non-invasive is reduced to an assumption that it is only locally invasive. This means that classical perturbation from the weak measurement is perfectly fine as long as it does not extend beyond the qubit being measured. This is similar to the locality assumption

of a standard Bell inequality.

A natural extension of this concept is to conduct weak measurements on both qubits of the Bell pair. This procedure, shown in Fig. 2.4, symmetriezes the measurement statistics on both branches of the Bell pair and brings the number of possible measurement angles to four. With four total measurement angles all the statistics necessary for violating the Bell inequality can be collected with a single experimental configuration. This is the basis of the Bell-Leggett-Garg inequality (BLGI) [25].

The BLGI is interesting because of its unique method of quantifying entanglement. This method makes it more robust against certain loopholes, but it also gives us an elegant way to examine the behavior of an entangled state under weak measurement. Normally an entangled state is broken when either qubit is measured. The measurement projects the entangled state into two individual qubit states and the only record of the initial entanglement is the correlation between the measurement results of both qubits. In a weak measurement the state is not completely projected, meaning that the entanglement is only partially collapsed. While a violation of the BLGI has been demonstrated in optical systems [26], it was only at a single measurement strength and the detector efficiency was too low to avoid the associated detector loopholes. By varying the measurement strength however, we can map out this continuous exchange of information and back-action. The continuous nature of the transition from projective to weak measurement also gives us more confidence that a violation of the inequality at the weakest measurement strengths. This would mean it is possible to extract the average state information of the Bell state without destroying it. Thus the BLGI inequality gives us a lens through which

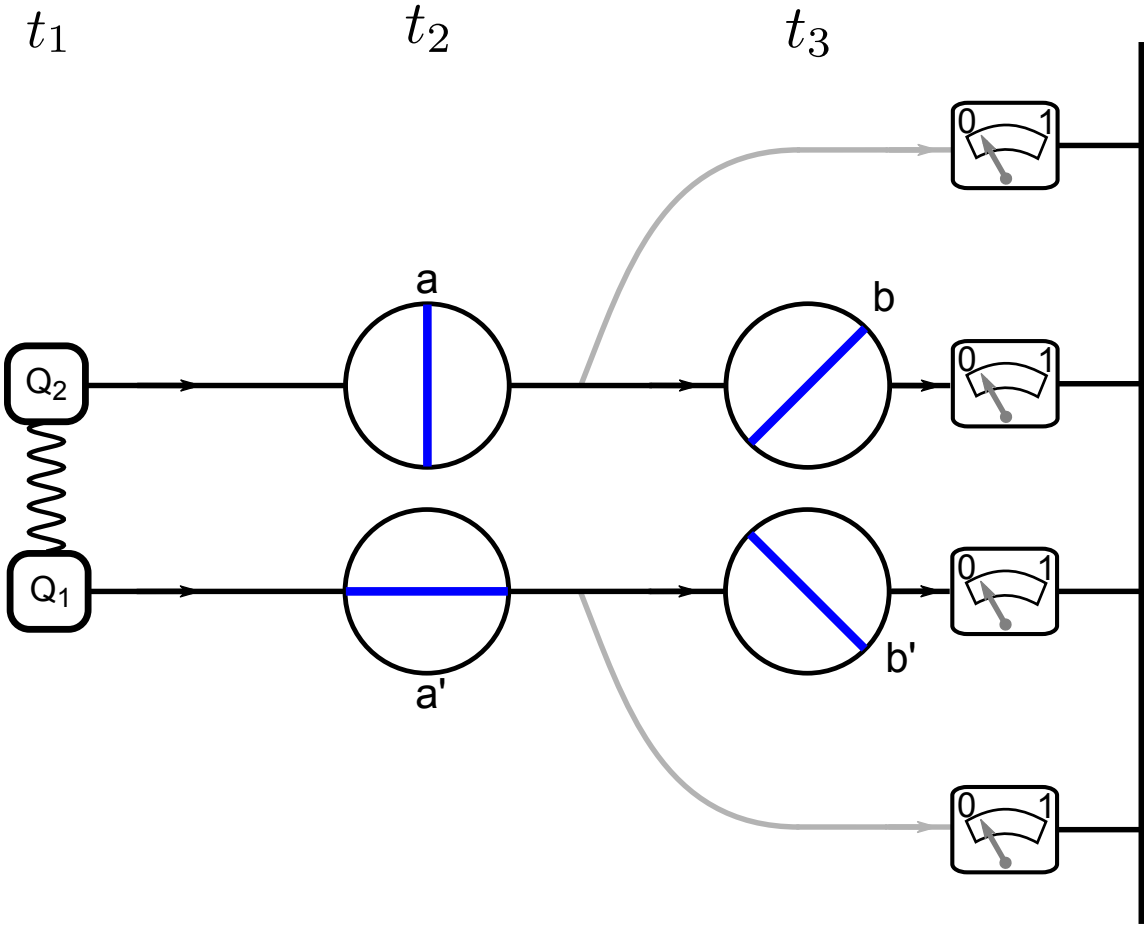

Figure 2.4: Schematic for the Bell-Leggett-Garg inequality. This extends the weak measurement protocol of the LGI to both qubits of a maximally entangled Bell state. By correlating both weak measurements and projective readout all the statistics of a CHSH experiment can be collected with a single experimental configuration. This allows the BLGI to avoid several loopholes such as the clumsy measurement and disjoint sampling loophole.

to examine the effect of measurement on entanglement collapse in continuous and controlled manner.

2.3 BLGI assumptions

The fundamental assumptions of the hybrid Bell-Leggett-Garg inequality are those of *local realism*, which are familiar from the Bell inequalities:

(i) If an object has several distinguishable physical states λ, then at any given time it occupies only one of them.

(ii) A measurement performed on one object of a spatially-separated pair cannot disturb the second object.

(iii) Measured results are determined causally by prior events.

Note that only assumption (ii) differs from the notion of *macrorealism* used in Leggett-Garg inequalities: it is weakened here to permit *local* invasiveness for sequential measurements in time made on the same object, while still forbidding spatially *remote* measurements from influencing each other. Note that the assumed physical state λ may be related to the quantum state, or may be a collection of more refined (but unspecified) hidden variables.

To these core assumptions we must append one more to permit noisy (i.e., realistic) detectors:

(iv) Unbiased noisy detectors produce results that are correlated with the true object state λ on average.

This assumption can be understood as follows. The object state λ ideally determines each measurable property $A(\lambda)$, but a physical detector (and environment) that interacts with the system

will also have a distinct physical state ξ that may fluctuate noisily between realizations (e.g., from the coupling procedure). In such a case the detector will report a correspondingly fluctuating signal $\alpha(\xi)$ according to some response probability $P_A(\xi|\lambda)$ for obtaining the detector state ξ given each definite system state λ. For any sensible detector, these response probabilities will be fixed by the systematic and repeatable coupling procedure (such as our ancilla measurement circuit). To calibrate such a detector, we must then assume that averaging over many realizations of the detector noise will faithfully reflect information about each *prepared* system state λ (even if that state ultimately changes for subsequent measurements due to the coupling):

$$\sum_{\xi} \alpha(\xi)\, P_A(\xi|\lambda) = A(\lambda). \tag{2.1}$$

Importantly, this equality formally states only what is usually assumed for an unbiased laboratory detector: that one can recover a meaningful system value $A(\lambda)$ by averaging away any detector noise.

Now consider the Bell-Leggett-Garg correlation. A correlated pair of objects with the joint state λ is sampled from an ensemble with the distribution $P(\lambda)$. (In our experiment, we prepare two qubits in a Bell state.) At a later time each object ($k = 1, 2$) is coupled to a detector (an ancilla qubit) that outputs a noisy signal α_k calibrated to measure the bounded property $A_k(\lambda) \in [-1, 1]$ on average (the Z operator for each Bell qubit). The noisy signal α_k generally has an expanded range of values that can lie outside the range $[-1, 1]$ (in our case this is due to re-scaling for measurement strength); however, for each λ the realizations of the output signal

will average to the correct bounded value by assumption (iv). (We verify this assumption with the ancilla calibration measurements using definite preparations of 0 or 1 on the Bell qubits.) Finally, each object is measured with a second detector that outputs a signal b_k for a similarly bounded property $B_k(\zeta) \in [-1, 1]$ (we read out the qubits directly to obtain $b_k = \pm 1$). From these four measured numbers, we then compute the CHSH-like correlator as a single number for each preparation

$$C = -\alpha_1\alpha_2 - \alpha_1 b_2 + b_1\alpha_2 - b_1 b_2. \tag{2.2}$$

The expanded ranges of the noisy signals α_k generally produce a similarly expanded range for the correlator C for each preparation. Nevertheless, averaging C over many realizations of the detector noise ξ_{A_k} and ξ_{B_k} and system states λ will produce

$$\begin{aligned}\langle C\rangle &= \textstyle\sum_\lambda \sum_{\substack{\xi_{A_1},\xi_{B_1}\\ \xi_{A_2},\xi_{B_2}}} C\, P(\xi_{A_1},\xi_{B_1}|\lambda)P(\xi_{A_2},\xi_{B_2}|\lambda)P(\lambda),\\ &= \textstyle\sum_\lambda \big[- A_1(\lambda)A_2(\lambda) - A_1(\lambda)B_2'(\lambda) + B_1'(\lambda)A_2(\lambda) - B_1'(\lambda)B_2'(\lambda)\big]\, P(\lambda),\end{aligned} \tag{2.3}$$

with $A_k(\lambda) = \sum_{\xi_{A_k},\xi_{B_k}} \alpha_k(\xi_{A_k})\, P(\xi_{A_k},\xi_{B_k}|\lambda)$ and $B_k'(\lambda) = \sum_{\xi_{A_k},\xi_{B_k}} b_k(\xi_{B_k})\, P(\xi_{A_k},\xi_{B_k}|\lambda)$, since postulate (ii) causes the joint distribution of the detector states to factor: $P(\xi_{A_1},\xi_{B_1},\xi_{A_2},\xi_{B_2}|\lambda) = P(\xi_{A_1},\xi_{B_1}|\lambda)P(\xi_{A_2},\xi_{B_2}|\lambda)$ in the same way as for a Bell inequality. From the postulates (i), (iii), and (iv), the averages $A_k(\lambda)$ and $B_k'(\lambda)$ are then bounded to the range $[-1, 1]$. Therefore, for each λ the sum of the bounded averages in Eq. (2.3) must itself be bounded by $[-2, 2]$.

Averaging this bounded result over $P(\lambda)$ produces the expected BLGI

$$-2 \leq \langle C \rangle \leq 2. \tag{2.4}$$

Importantly, the probability $P(\xi_{A_k}, \xi_{B_k}|\lambda) = P(\xi_{A_k}|\lambda)P(\xi_{B_k}|\lambda, \xi_{A_k})$ for each qubit k admits the dependence of the B'_k measurement on an *invasive* A_k measurement that can alter the physical state λ. Despite any randomization of the results $b_k(\xi_{B_k})$ caused by such local invasiveness, however, the perturbed averages $B'_k(\lambda)$ must still lie in the range $[-1, 1]$ since each $b_k = \pm 1$ by construction. This allowance for *locally* invasive measurements in the BLGI is what avoids the clumsiness loophole [11] of the usual LGI. The fact that the entire correlator C is computed for every realization in the same experimental configuration is what avoids any variant of the disjoint sampling loophole [10] for the usual Bell and LGIs (such as from systemic bugs in the preparation software).

There are, however, two notable ways that our derivation of the BLGI in Eq. (2.4) could fail. First, the assumptions (i–iii) of local realism could fail, as in a standard Bell inequality. This is certainly possible in our case since the Bell qubits are neighbors on the same superconducting chip. However, arranging for a locally realist model that accounts for the needed disturbance effects for the neighboring Bell qubits, the neighboring Bell-ancilla qubits, each remote pair of Bell-ancilla qubits, and the remote ancilla-ancilla qubits simultaneously is substantially more difficult (and therefore much less likely) than arranging for such disturbance in the usual Bell test on just two neighboring qubits. Moreover, our experiment verifies the detailed functional dependence of the quantum predictions as the weak measurement angle ϕ is varied, which

further constrains any purported locally realist explanation. Thus our tested BLGI significantly tightens the locality loophole [7] compared to the usual Bell test performed on the same chip.

Second, the noisy detector assumption (iv) could fail due to hidden preparation noise ξ_P not included in the state λ that systematically affects the detector output in both arms in a correlated way. In this case, the detector response would become noise-dependent $P_A(\xi|\lambda) \rightarrow P_A(\xi|\lambda, \xi_P)$ such that the calibration of Eq. (2.1) will be satisfied only after additionally averaging over ξ_P. Such correlated noise would prevent the detector distributions from factoring for each λ in Eq. (2.3), which formally spoils the inequality. However, in our experiment such a systematic bias due to correlated noise has been extensively checked during the characterization of the chip and the measurement calibration by deliberately preparing a variety of uncorrelated distributions $P(\lambda)$ (i.e., different qubit states) and looking for spurious cross-correlations of the various qubit readout signals that would be expected in the presence of such hidden preparation noise. Hence, the failure of assumption (iv) additionally requires an unlikely preparation-conspiracy where every calibration check that has been done is somehow immune to the hidden detector-noise correlations.

2.4 Conclusion

The BLGI provides a interesting test not only of the assumptions of local-macro-realism, but also of the behavior of entangled states under measurement. The draw back is that this experiment requires a high fidelity system with excellent control to achieve. Experimental errors and imperfections can lower the maximum measurable correlation amplitude perhaps even below

the level necessary for a violation. To move forward we must understand the effect of possible errors on the magnitude of BLGI correlations and what experimental systems are best suited to this experiment. Due to recent advances in both gate and measurement fidelity, superconducting qubit systems have emerged as an ideal system for testing weak measurements and the BLGI.

Chapter 3

Superconducting qubits: engineered quantum elements

An experimental system capable of violating the BLGI must meet several important requirements. The system must be able to encode quantum information onto the ground and excited state of a two-level system (qubit), it must exhibit the high fidelity control necessary to generate entangled states and conduct weak measurements, and it must provide a way to independently read out the state of each qubit with high precision. Fortunately, these are the same criteria necessary for creating a high fidelity quantum processor, and the field of quantum information has produced several promising physical implementations of such a processor. One of the most promising of these implementations has been superconducting quantum processors, in which the logical basis of 0 and 1 is provided by the ground and first excited state of a nonlinear resonant circuit. As macroscopic circuits, many of the characteristics of superconducting qubits

can be independently engineered and optimized according to classical circuit theory. Through this optimization, superconducting qubits have recently achieved record level gate fidelity [27] in a modestly scaleable system. Even more importantly, superconducting qubits have demonstrated high efficiency and high fidelity state readout in very short times [28]. This high fidelity control and efficient measurement makes superconducting qubits an ideal system for inequality experiments and the investigation of fundamental physics.

3.1 Engineering a quantum element

3.1.1 Superconducting circuits as quantum harmonic oscillators

To understand the behavior of circuit resonators, it is helpful to consider the simple harmonic oscillator in which a particle of mass m is subject to a restoring force $-kx$, with force constant k. Here the conjugate variables of momentum p and position x are related by the familiar formulas $p = mv = m\dot{x}$ and $-kx = ma = m\dot{v} = \dot{p}$. This force results in a parabolic potential energy and the Hamiltonian

$$H = \frac{p^2}{2m} + \frac{1}{2}m\omega_m^2 x^2, \tag{3.1}$$

where the mechanical resonance frequency $\omega_m = \sqrt{k/m}$.

We can construct a circuit analogue of this system with a parallel LC resonant circuit, shown in Fig. 3.1 (a). In this circuit we have the conjugate variables of charge $Q = CV_C$ and flux $\Phi = LI$. Using Kirchhoff's laws and integrating the voltage around the circuit we see that the current I through both elements is equivalent, but that $V_L + V_C = 0$. In this

case $V_L = L\dot{I} = \dot{\Phi}$ and since $V_c = -V_L$, we can relate the charge to the flux with the expression $Q = -CV_L = -CL\dot{I} = -C\dot{\Phi}$. We can then also relate the flux to the charge with the relation $\Phi = LI = L\dot{Q}$. From circuit theory we know that the energy stored in the capacitor and the inductor is given by $Q^2/2C$ and $\Phi^2/2L$ respectively. By making the substitution $\omega_r = \sqrt{1/LC}$, we can see the resulting Hamiltonian

$$H = \frac{Q^2}{2C} + \frac{1}{2}C\omega_r^2\Phi^2 \tag{3.2}$$

obeys the same physics as the simple harmonic oscillator. In this analogy the mass of the particle is given by the capacitance of the circuit, and the force constant k is equal to the inverse of the inductance.

Normally, macroscopic quantum behavior would be inhibited in a resonant circuit due to the presence of internal dissipation and uncontrolled thermally generated excitations. Both of these problems can be overcome however, by constructing a resonator out of superconducting material and operating at sufficiently low temperature. As an example, consider an aluminum resonator with a resonant frequency $\omega_r/2\pi = 6\,\text{GHz}$ operated at the base temperature of a dilution refrigerator, typically 20 mK. The operating temperature is well below the 1.2 K superconducting transition temperature T_c of aluminum, meaning the normal electron charge carriers have condensed into the Cooper pair states of a superconductor. Coherent oscillation of the Cooper pairs is possible because the large energy gap $\Delta \gg \hbar\omega_r$ prevents scattering of individual electrons (quasi-particles). Similarly, the probability of a thermal excitation is suppressed at low temperatures proportional to the Boltzmann distribution given by $\exp(-\hbar\omega_r/kT)$. At at frequency of $\omega_r/2\pi = 6\,\text{GHz}$ and a temperature $T = 20\,\text{mK}$ this probability is roughly

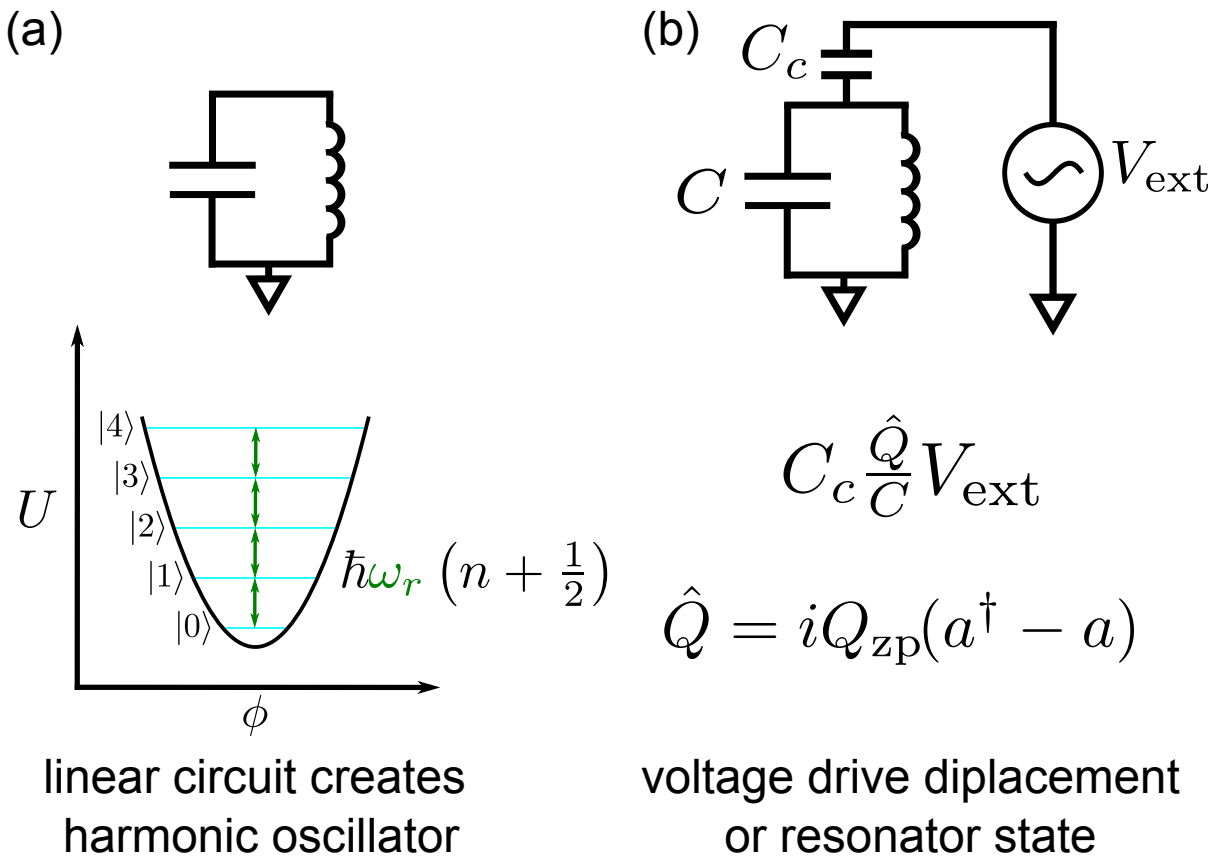

Figure 3.1: Diagram of a quantum harmonic oscillator circuit (a) The linear LC resonator acts as a quantum harmonic oscillator with evenly spaced energy levels. determined by the resonant frequency $\omega_r = \sqrt{1/LC}$ (b) A voltage bias, applied through a coupling capacitor, changes the energy of the system through the interaction term $C_c(\hat{Q}/C)V_{\text{ext}}(t)$ in the Hamiltonian.

3×10^{-7}. Thus, operating such a resonator at GHz frequencies and mK temperatures provides a system which should display coherent quantum oscillations while idling in the ground state.

By removing the constraints of dissipation and thermal excitation, there should be nothing preventing a superconducting resonant circuit from exhibiting coherent quantum behavior. To understand this behavior however, we can no longer rely on the classical parameters of charge and flux. Quantum mechanically the conjugate variables Q and Φ become non commuting operators $\hat{Q}$ and $\hat{\Phi}$ and obey the canonical commutation relation $[\hat{\Phi}, \hat{Q}] = i\hbar$. Continuing our

earlier analogy to the simple harmonic oscillator we can derive equivalent equations for the quantum harmonic oscillator model of a macroscopic electrical resonator

$$\hat{\Phi} = \Phi_{\text{zp}}(a + a^\dagger) \tag{3.3}$$

$$\Phi_{\text{zp}} = \sqrt{\frac{\hbar}{2C\omega_r}} \tag{3.4}$$

$$\hat{Q} = iQ_{\text{zp}}(a^\dagger - a) \tag{3.5}$$

$$Q_{\text{zp}} = = \sqrt{\frac{C\omega_r\hbar}{2}} \tag{3.6}$$

$$\tag{3.7}$$

Here we have written the charge and flux in the form of the familiar creation and annihilation operators but neglected the hat operator notation for consistency with traditional descriptions of the quantum harmonic oscillator. Additionally we have grouped the prefactors for the charge and flux operators into the zero point fluctuation parameters Q_{zp} and Φ_{zp}, such that $Q_{\text{zp}}^2/2C = \Phi_{\text{zp}}^2/2L = \hbar\omega/4$. Physically we can now interpret the creation and annihilation operators $a^\dagger$ and a as either creating or annihilating single photon excitations of the resonant circuit. The Hamiltonian written with these operators

$$\hat{H} = \hbar\omega_r \left(a^\dagger a + \frac{1}{2}\right), \tag{3.8}$$

simply describes the energy of the circuit as the ground state plus the number of photon excitations given by the number operator $a^\dagger a$.

As stated earlier, at the base temperature of a dilution refrigerator our resonator should idle in the ground state. We might then be able to use the ground and first excited state of the harmonic oscillator as the 0 and 1 basis of our quantum processor. First however, we must understand what happens to the system when we attempt to add energy through a classical

drive. We can imagine this classical drive as a time varying voltage $V_{\text{ext}}(t)$ applied through a coupling capacitor C_c shown in Fig. 3.1 (b). If this coupling capacitor is small relative to the capacitance of the circuit $C_c \ll C$, it will leave the Hamiltonian unchanged except for the presence of an interaction term given by

$$\begin{aligned} \hat{H}_{\text{int}} &= C_c \frac{\hat{Q}}{C} V_{\text{ext}}(t) && (3.9) \\ &= i \frac{C_c}{C} Q_{\text{zp}} V_{\text{ext}}(t)(a^\dagger - a) && (3.10) \end{aligned}$$

To understand how the system evolves under this perturbation, we can use the time evolution operator in the interaction picture. In this picture

$$\begin{aligned} a &\rightarrow a e^{-i\omega_r t} && (3.11) \\ a^\dagger &\rightarrow a^\dagger e^{i\omega_r t}, && (3.12) \end{aligned}$$

giving us the time evolution operator

$$U = \exp\left(-\frac{i}{\hbar} i Q_{\text{zp}} C_c \frac{C_c}{C} \int_0^t V_{\text{ext}}(t')(a^\dagger e^{i\omega_r t'} - a e^{-i\omega_r t'}) dt' \right). \tag{3.13}$$

In a realistic experiment, the voltage drive $V_{\text{ext}}(t')$ consists of time dependent driving voltage $V_{\text{ext}}(t') = V_0 \cos(\omega t' + \phi)$, where ω is close to the resonant frequency of the circuit. We can then decompose the cosine into the complex oscillator terms

$$V_{\text{ext}}(t') = \frac{V_0}{2}\left(e^{-i(\omega t' + \phi)} + e^{i(\omega t' + \phi)} \right). \tag{3.14}$$

If we multiply through by each oscillator term, neglect the rapidly oscillating terms $\pm(\omega_r + \omega)$, and group all of the remaining terms together based on operator, we get the variable α described

by

$$\alpha = \frac{1}{\hbar} Q_{\text{zp}} \frac{C_c}{C} \frac{V_0}{2} e^{-i\phi} \int_0^t e^{-i(\omega-\omega_r)t'} dt' \tag{3.15}$$

This makes the time evolution operator equivalent to harmonic oscillator displacement operator [29]

$$U = D = e^{\alpha a^\dagger - \alpha^* a}, \tag{3.16}$$

This displacement operator, when applied to the ground state, will drive it into a coherent state $D|0\rangle = |\alpha\rangle$, which depends on the amplitude of α.

As the displacement amplitude α is a classical drive term, we can understand it using classical resonant circuit analysis. First we can make the substitution $\Delta\omega = (\omega - \omega_r)$ and integrate over time t' to get

$$\alpha = \frac{1}{\hbar} Q_{\text{zp}} \frac{C_c}{C} \frac{V_0}{2} e^{-i\phi} \frac{1 - e^{-i\Delta\omega t}}{i\Delta\omega}, \tag{3.17}$$

where the last term reduces to just t in the limit that $\Delta\omega \to 0$. From this equation we can see that the nature of the displacement depends on the relative frequency of the resonator and the drive, shown in Fig. 3.2 plotted on the real Q and imaginary I plane. For a non-resonant drive tone, the phase of the drive oscillates relative to the phase of the resonator state as $\Delta\omega t + \phi$. This relative phase drift causes the drive tone to displace the resonator state in a circle around the IQ plane and limits the maximum amplitude of the coherent state.

When the drive is exactly on resonance with the circuit, α grows linearly in time. Since the drive adds a scaled voltage offset $(C_c/C)(V_0/2)$ twice per cycle, we can combine various

terms in α which describe the resonant voltage fluctuation

$$\dot{\Phi} = \frac{C_c}{C}\frac{V_0}{2}\omega_r t. \tag{3.18}$$

We can then rewrite α as

$$\alpha = \frac{1}{\hbar}Q_{\text{zp}}\frac{C_c}{C}\frac{V_0}{2}te^{-i\phi} \tag{3.19}$$

$$\alpha = \frac{1}{\hbar\omega_r}Q_{\text{zp}}\left(\frac{C_c}{C}\frac{V_0}{2}\omega_r t\right)e^{-i\phi} \tag{3.20}$$

$$\alpha = \frac{1}{\hbar\omega_r}Q_{\text{zp}}\dot{\Phi}e^{-i\phi}. \tag{3.21}$$

It is then strait forward to show that $(Q_{\text{zp}}\dot{\Phi}/\hbar\omega_r)^2 = E_{\text{res}}/\hbar\omega_r$, so that $|\alpha|^2$ is the energy in the resonator divided by the energy per photon.

To better understand the behavior of our driven resonator, we can compare our classical result to the quantum description of this coherent state $|\alpha\rangle$ described by

$$|\alpha\rangle = e^{-\frac{1}{2}|\alpha|^2}\sum_{n=1}^{\infty}\frac{\alpha^n}{\sqrt{n!}}|n\rangle, \tag{3.22}$$

as discussed in Ref. [29]. The coherent state consists of a superposition of the number states $|n\rangle$ with a Poisson distribution of probability amplitudes described by

$$P(n) = |\langle n|\alpha\rangle|^2 = \frac{|\alpha|^{2n}e^{-|\alpha|^2}}{n!}, \tag{3.23}$$

and centered around $|\alpha|^2$ [29]. From our classical analysis, we know that $|\alpha|^2$ should be proportional to the number of photons in the resonator. If we apply the the number operate $a^\dagger a$ to the state $|\alpha\rangle$ we indeed calculate that $\langle\alpha|a^\dagger a|\alpha\rangle = \langle n\rangle = |\alpha|^2$.

We can use this quantum description to investigate the possibility of driving a single photon excitation into the resonator. To do this we would logically expect to drive with a voltage

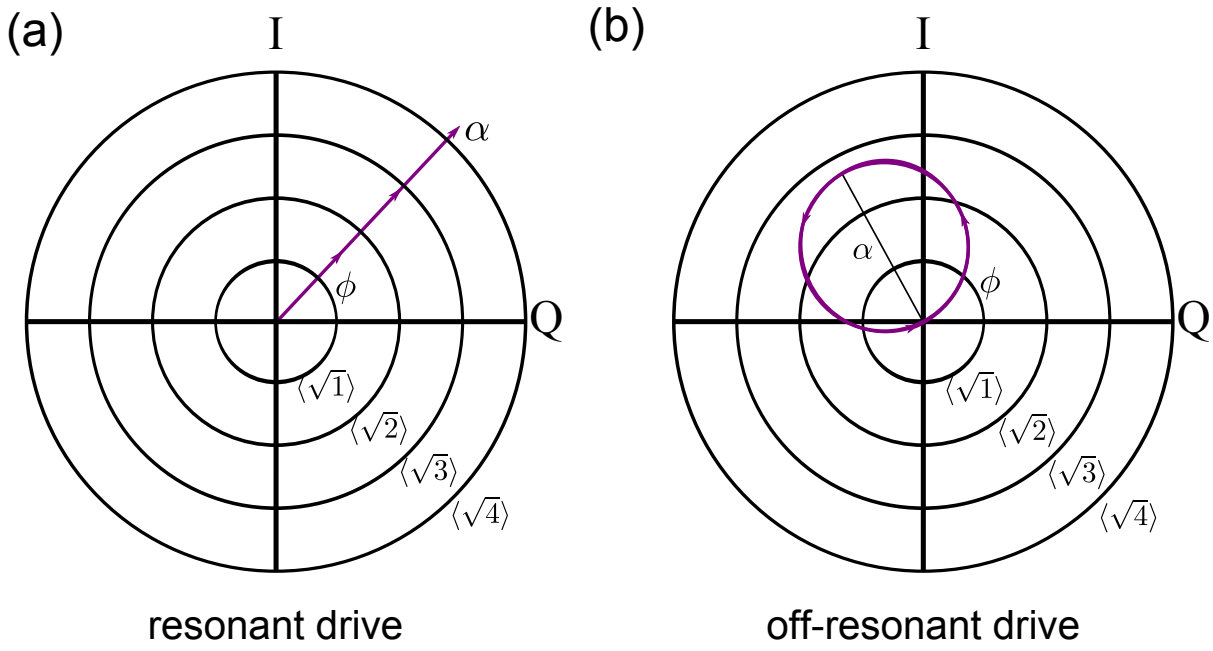

Figure 3.2: Average photon population of a linear resonator under a time dependent voltage drive, plotted on real Q and imaginary I axes. (a) If the drive frequency is on resonance with the resonator then the photon population will grow proportional to the drive time t with drive phase ϕ. (b) An off resonant drive will have an oscillating phase relative to the photons in the resonator. This relative phase determines if the applied voltage drives or damps the circuit and lowers the maximum possible α by a factor of $1/\Delta\omega$. For large detunings the state of the resonator will simply oscillate quickly around a state of $\langle 0\rangle$ average photons.

amplitude such that $|\alpha|^2 = 1$. If however, we then calculate the probability of being in the $|1\rangle$ state, we find that it is only $1/e$ along with smaller probabilities of being in higher photon number states. Obviously without being able to drive single photon excitations it is not possible to use the lowest two energy levels as our logical qubit basis. In fact, the behavior of the coherent state is semi-classical [29] and, except for features like quantum noise fluctuations, the state response to an external linear drive can be entirely described by classical circuit theory.

The problem with using the quantum harmonic oscillator as a qubit is that the energy levels are all equally spaced. The interaction term resonantly drives transitions not just from $|0\rangle$ to $|1\rangle$, but to every higher level in the system. As we saw in the previous section, driving the

resonator off resonance will induce relative phase oscillations, which average the displacement to zero for large detunings. Thus it should be possible to create the desired two-level state in a superconducting circuit by constructing an anharmoic oscillator, in which the various energy levels are not equally separated. In this way we can choose which state transition to drive by altering the frequency of our drive tone.

3.1.2 Nonlinear resonators create anharmonic oscillators.

To understand how to engineer this anharmonicity, it is helpful to first consider a classical circuit Hamiltonian with a nonlinear element supplied by the current and phase relations of the Josephson junction

$$V = \frac{\Phi_0}{2\pi}\dot{\delta} \tag{3.24}$$

$$I = I_c \sin(\delta). \tag{3.25}$$

Here I_c is the critical current of the junction, δ is the phase across the junction, and Φ_0 is the flux quanta. To relate this behavior to our previous analysis, it is helpful to make a substitution for δ and rewrite it in terms of the flux variable Φ as

$$\delta = \frac{2\pi}{\Phi_0}\Phi. \tag{3.26}$$

Written in this way, the voltage across a Josephson junction is given by Faraday's law $V = \dot{\Phi}$, just like the linear inductor. The Josephson current equation then becomes

$$I = I_c \sin\left(\frac{2\pi\Phi}{\Phi_0}\right). \tag{3.27}$$

For small Φ we can approximate the junction current as

$$I = \frac{2\pi I_c}{\Phi_0}\Phi, \tag{3.28}$$

and define the useful Josephson inductance constant $L_{J0} = \Phi_0/(2\pi I_c)$ based on the definition of flux $\Phi = LI$. The non-linearity of the device is evident from the differential Josephson inductance

$$\begin{aligned} L_J &\equiv \frac{\dot{\Phi}}{\dot{I}} && (3.29)\\ &= \frac{L_{J0}}{\cos\left(\frac{2\pi\Phi}{\Phi_0}\right)}. && (3.30) \end{aligned}$$

This effective Josephson inductance varies depending on the flux amplitude, making the response nonlinear in Φ. By replacing the linear inductor of a parallel LC circuit with a Josephson junction of equivalent junction inductance L_J, we create the non-linear oscillator shown in Fig 3.3 (a).

To write the Hamiltonian for this circuit we first calculate the potential energy due to the nonlinear element, by integrating the product of junction voltage and current with respect to time.

$$\begin{aligned} E &= \int IV dt && (3.31)\\ E &= \int I_c \sin\left(\frac{2\pi\Phi}{\Phi_0}\right)\dot{\Phi} dt && (3.32)\\ E &= -\frac{\Phi_0 I_c}{2\pi}\cos\left(\frac{2\pi\Phi}{\Phi_0}\right) && (3.33) \end{aligned}$$

Adding this potential energy term to the kinetic energy term, we get the nonlinear circuit Hamiltonian

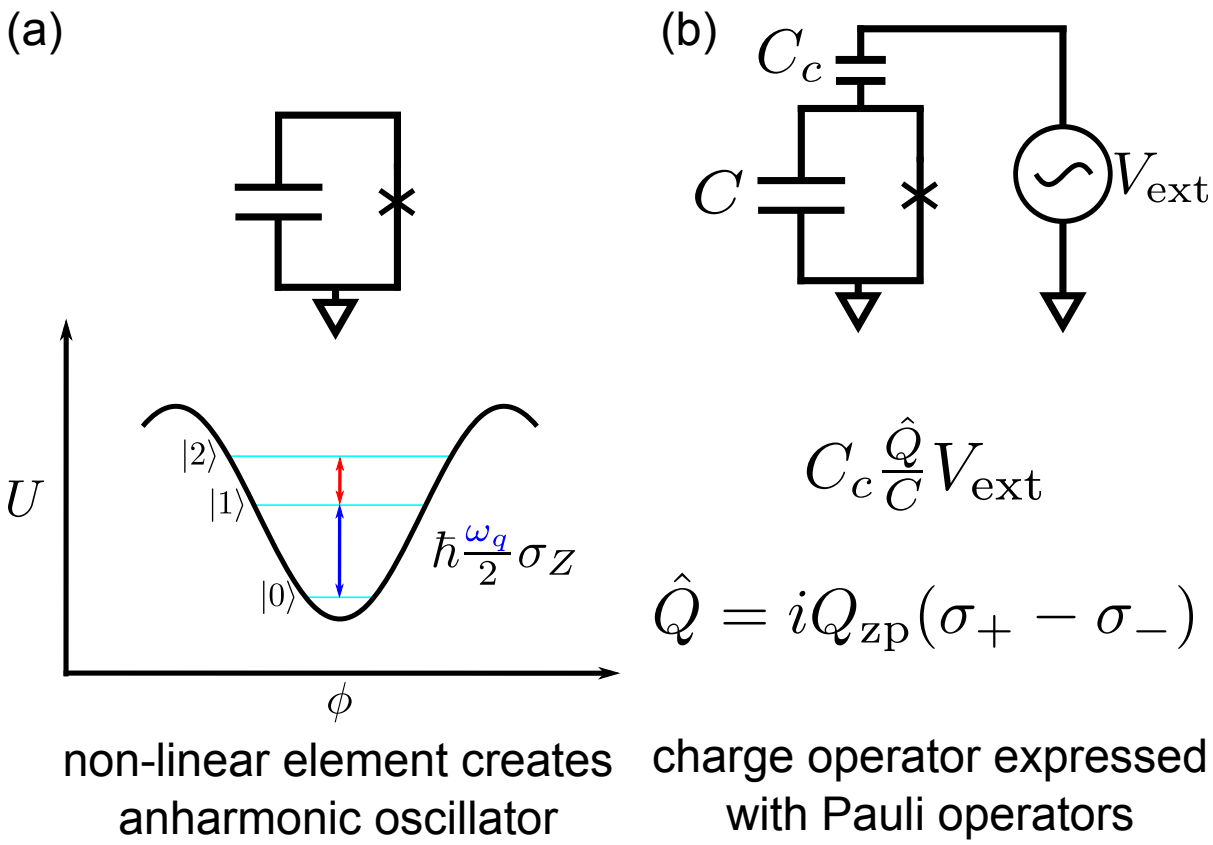

Figure 3.3: Diagram of a quantum anharmonic oscillator (qubit). (a) The non-linearity of the Josephson junction creates an anharmonicity in the oscillator, changing the energy level spacing between different energy levels. This energy difference isolates the ground and first excited state for logical qubit operations. (b) A voltage bias, applied through a coupling capacitor, changes the energy of the system through the same interaction term as the quantum harmonic oscillator. For the anharmonic oscillator the creation and annihilation operators can be replaced by the Pauli operators σ_+ and σ_-.

$$H = \frac{Q^2}{2C} - \frac{\Phi_0 I_c}{2\pi}\cos\left(\frac{2\pi\Phi}{\Phi_0}\right) \tag{3.34}$$

$$= \frac{Q^2}{2C} - E_J\cos\left(\frac{2\pi\Phi}{\Phi_0}\right), \tag{3.35}$$

where we have grouped the various terms making up the cosine amplitude into the junction energy $E_J = \Phi_0 I_c/2\pi$. To understand how this Hamiltonian relates to the simple harmonic

oscillator, we can expand the cosine function in terms of the variable Φ. Expanding to fourth order in Φ we get

$$H = \frac{Q^2}{2C} - E_J\left[1 - \left(\frac{2\pi}{\Phi_0}\right)^2 \frac{\Phi^2}{2} + \left(\frac{2\pi}{\Phi_0}\right)^4 \frac{\Phi^4}{24} - ...\right]. \tag{3.36}$$

The first term in the potential is just an energy offset $-E_J$ which will have no effect on the dynamics of the system can can largely be ignored. If we include the second term we see that

$$\begin{aligned} H &= \frac{Q^2}{2C} + E_J\left(\frac{2\pi}{\Phi_0}\right)^2 \frac{\Phi^2}{2} && (3.37)\\ &= \frac{Q^2}{2C} + \frac{1}{L_{J0}}\frac{\Phi^2}{2} && (3.38)\\ &= \frac{Q^2}{2C} + \frac{1}{2}C\omega_r^2\Phi^2 && (3.39) \end{aligned}$$

where $\omega_r = \sqrt{1/CL_{J0}}$. Thus if Φ is small relative to the flux quantum Φ_0, the Hamiltonian approximates that of a linear resonator. This approximation will be helpful in understanding the quantum behavior of the circuit.

If the quantum state of our non-linear circuit is well localized in a single well of the cosine potential, we can understand the behavior of the system by using the quartic term of the Hamiltonian as a perturbation of the quantum harmonic oscillator at small Φ. To ensure that this is the case, we will operate our device in the "transmon" regime [30] characterized by $E_J/E_c \gg 1$ where $E_c = e^2/2C$. This has the added benefit of making it robust against charge noise in the system [30]. Taking the quantum harmonic oscillator as the unperturbed system Hamiltonian, we get the familiar photon number states $|n\rangle$ and energy levels $\hbar\omega_r(n + 1/2)$. We can then apply first order perturbation theory to these states to calculate the energy level perturbation given by

$$E'_n = -\frac{E_J}{24}\left(\frac{2\pi}{\Phi_0}\right)^4 \langle n|\hat{\Phi}^4|n\rangle \tag{3.40}$$

$$E'_n = -\frac{E_J}{24}\left(\frac{2\pi}{\Phi_0}\right)^4 \Phi_{\text{zp}}^4 \langle n|(a+a^\dagger)^4|n\rangle \tag{3.41}$$

to find the resulting qubit Hamiltonian. The perturbed energy levels from this term are calculated in Ref. [30], and described by

$$E_n = -E_J + \hbar\omega_r\left(n+\frac{1}{2}\right) - \frac{E_c}{12}\left(6n^2+6n+3\right). \tag{3.42}$$

Here each energy level consists of the offset term $-E_J$, the unperturbed photon energy level $\hbar\omega_r n$ and a correction from the quartic perturbation given by multiples of the term E_c. Calculating the transition energies from this equation we get

$$\hbar\omega_{10} = E_1 - E_0 = \hbar\omega_r - E_c \tag{3.43}$$

$$\hbar\omega_{21} = E_2 - E_1 = \hbar\omega_r - 2E_c \tag{3.44}$$

Thus the term E_c represents an anharmonicity in the energy levels, reducing each transition frequency more and more as the photon number increases. This difference in the energy level separation is important because it allows us to address different energy level transitions by driving at different frequencies. For a typical transmon this anharmonicity is defined as $\eta = \omega_{10} - \omega_{21}$ and is of the order $\eta/2\pi \approx 200\,\text{MHz}$.

3.2 Qubit operation

3.2.1 Logical gates

With the qubit anharmonicty provided by the quartic perturbation term of the nonlinear Hamiltonian, we can ideally describe the lowest two levels of the nonlinear resonator as a two-level state. When describing the behavior of a two-level state, it is helpful to use the Bloch sphere representation, shown in Fig. 3.4, in which the $|0\rangle$ and $|1\rangle$ states correspond to the poles of the sphere. We can also express state measurements and qubit rotations in terms of the familiar Pauli operators. With this notation we can express the Hamiltonian simply as

$$\hat{H} = \hbar\frac{\omega_q}{2}\sigma_Z, \tag{3.45}$$

where σ_Z is the pauli Z operator and $\omega_q = \omega_{10}$. Here we have omitted the hat notation for the Pauli operators for simplicity. We can also replace the creation and annihilation operators in $\hat{Q}$ with the terms σ_+ and σ_-. Thus the charge operator becomes

$$\hat{Q} = Q_{\text{zp}} i(\sigma_+ - \sigma_-). \tag{3.46}$$
$$\tag{3.47}$$

As analogues of the creation and annihilation operators, σ_+ and σ_- have a similar time dependence given by

$$\sigma_+ \rightarrow \sigma_+ e^{i\omega_q t} \tag{3.48}$$
$$\sigma_- \rightarrow \sigma_- e^{-i\omega_q t}. \tag{3.49}$$

Just as an excitation in the harmonic oscillator evolved in phase with the term $\exp(-i\omega_r t)$, the qubit state evolves in phase with the term $\exp(-i\omega_q t)$ around the Z axis of the Bloch sphere. This can be seen in the time dependence of the rotation operators σ_X and σ_Y. In the Schrodinger picture, a rotation about a given axis will have a different effect depending on the phase of the qubit state. In the interaction picture, this is reflected in the time evolution of the σ_Y operator described below

$$\begin{aligned}
\sigma_Y &= i(\sigma_+ - \sigma_-) && (3.50)\\
&= i\left(\sigma_+ e^{i\omega_q t} - \sigma_- e^{-i\omega_q t}\right) && (3.51)\\
&= i\left(\cos(\omega_q t)(\sigma_+ - \sigma_-) + i\sin(\omega_q t)(\sigma_+ + \sigma_-)\right) && (3.52)\\
&= \cos(\omega_q t)\sigma_Y - \sin(\omega_q t)\sigma_X. && (3.53)
\end{aligned}$$

Thus, in the interaction picture a rotation operator will evolve between σ_X and σ_Y with angular frequency ω_q.

Just like with the harmonic oscillator we can add energy to the system by applying a voltage drive through a coupling capacitor. We can then calculate the same time evolution operator in the interaction picture

$$U = \exp\left(-\frac{i}{\hbar} Q_{\text{zp}} \frac{C_c}{C} \int_0^t V_{\text{ext}}(t') i(\sigma_+ e^{i\omega_q t'} - \sigma_- e^{-i\omega_q t'}) dt'\right), \tag{3.54}$$

for which the only difference is that we have replaced the creation and annihilation operators with Pauli operators. If we also apply the same time dependence to our drive voltage

$$\begin{aligned}
V_{\text{ext}}(t) &= V_0 \cos(\omega t' + \phi) && (3.55)\\
&= \frac{V_0}{2}\left(e^{-i(\omega t' + \phi)} + e^{i(\omega t' + \phi)}\right) && (3.56)
\end{aligned}$$

We can conduct a similar simplification of the time dependence of the interaction. If we multi-

ply through the oscillator terms, disregard the terms with $\pm(\omega+\omega_q)$, and make the substitution $\Delta\omega = \omega - \omega_q$ we get

$$\begin{aligned} V_{\text{ext}}(t')\hat{Q}(t') &= Q_{\text{zp}}\frac{V_0}{2}i\left(e^{-i(\omega t'+\phi)} + e^{i(\omega t'+\phi)}\right)\left(\sigma_+ e^{i\omega_q t'} - \sigma_- e^{-i\omega_q t'}\right) && (3.57)\\ &= Q_{\text{zp}}\frac{V_0}{2}i\left(\sigma_+ e^{-i(\Delta\omega t'+\phi)} - \sigma_- e^{i(\Delta\omega t'+\phi)}\right) && (3.58)\\ &= Q_{\text{zp}}\frac{V_0}{2}i\left(\cos(\Delta\omega t'+\phi)(\sigma_+ - \sigma_-) - i\sin(\Delta\omega t'+\phi)(\sigma_+ + \sigma_-)\right) && (3.59)\\ &= Q_{\text{zp}}\frac{V_0}{2}(\cos(\Delta\omega t'+\phi)\sigma_Y + \sin(\Delta\omega t'+\phi)\sigma_X). && (3.60)\end{aligned}$$

Our time evolution operator then becomes

$$U = \exp\left(-\frac{i}{\hbar}Q_{\text{zp}}\frac{C_c}{C}\int_0^t \frac{V_0}{2}(\cos(\Delta\omega t'+\phi)\sigma_Y + \sin(\Delta\omega t'+\phi)\sigma_X)dt'\right) \quad (3.61)$$

Where we have re-expressed the σ_+ and σ_- operators into a mixture of σ_X and σ_Y operators.

To appreciate what this difference means physically, let us examine the simple case of driving on resonance with zero phase ($\Delta\omega = 0$ and $\phi = 0$). In this case the time evolution equation becomes

$$\begin{aligned} U &= e^{-i\alpha\sigma_Y} && (3.62)\\ \alpha &= \frac{1}{\hbar}Q_{\text{zp}}\frac{C_c}{C}\int_0^t \frac{V_0}{2}dt'. && (3.63)\end{aligned}$$

Interestingly, this is exactly the same expression for α we calculated for the displacement operator in the harmonic oscillator case. We can understand the effect of this displacement operator with σ_Y by expanding the exponential function in a Taylor series, and grouping the even and odd terms together to get

$$U = e^{-i\alpha\sigma_Y} \tag{3.64}$$

$$U = \sum_{n=0}^{\infty} \frac{(-i\alpha\sigma_Y)^{2n}}{(2n)!} + \sum_{n=0}^{\infty} \frac{(-i\alpha\sigma_Y)^{2n+1}}{(2n+1)!} \tag{3.65}$$

$$U = \cos(\alpha)I - i\sin(\alpha)\sigma_Y, \tag{3.66}$$

where I is the identity. Thus for the simple case of resonant drive with zero phase, the time evolution operator causes the system to undergo a rotation around the Y axis of the Bloch sphere with angle 2α; the factor of 2 in front of α comes from the fact that an angle of $\alpha = \pi$ completes a 2π rotation from $|0\rangle$ to $-|0\rangle$. For a drive phase of $\phi = \pi/2$ we could calculate a similar expression for σ_x and rotate around the X axis of the Bloch sphere. The qubit state rotation for general α and ϕ is shown graphically in Fig 3.4 (a). Thus the same pulse that drove a displacement of the harmonic oscillator in the IQ *plane* can be used to drive a continuous rotation of the qubit state along the surface of the Bloch *sphere*.

While our resonant drive analysis is accurate for a perfect two level state, for the superconducting qubit we must ensure we are not also populating higher energy level states. This is particularly important in deciding how to turn our qubit drive on an off. Fourier analysis of different drive pulses shows that a simple square wave would lead to a non negligible resonant driving of the higher level states, through frequency broadening of the drive tone [31]. For this naive pulse we can treat the higher levels as two-level states undergoing an off-resonant drive. The effect of this off-resonant drive, shown in Fig. 3.4 (b), can be thought of as a combination of two rotation vectors. The state is rotating around the Y axis with a frequency proportional

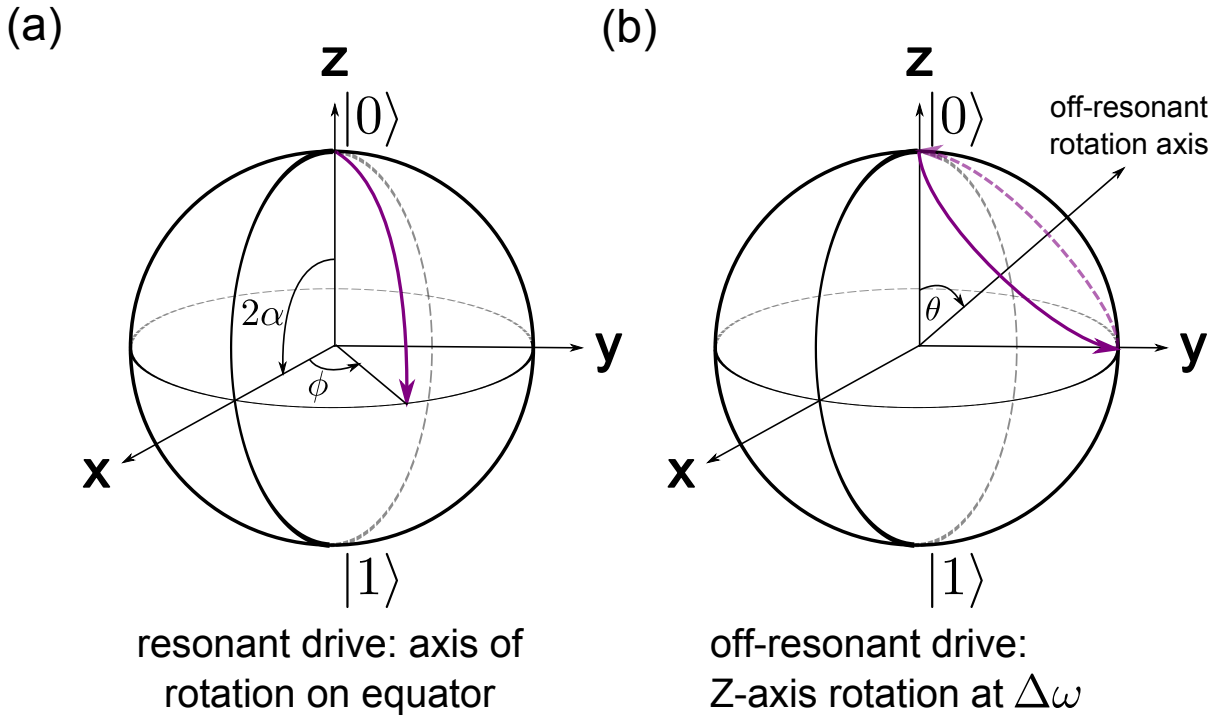

Figure 3.4: Evolution of a qubit state on the Bloch sphere under a time dependent voltage drive. (a) If the drive frequency is on resonance with the qubit it will execute a σ_X or σ_Y rotation of angle α around an axis on the equator with relative phase ϕ. (b) If the drive is not resonant with the qubit frequency it will change the angle of the rotation axis by introducing a rotation around the Z axis with frequency $\Delta\omega$. This tilted rotation axis limits the maximum excited state population in the qubit, and for large detunings causes the the state of the qubit to oscillate quickly around $|0\rangle$.

to the constants of the interaction term

$$\alpha_0 = \frac{Q_{\text{zp}}}{\hbar}\frac{C_c}{C}\frac{V_0}{2}, \tag{3.67}$$

and around the Z axis with a frequency equal to $\Delta\omega$. Based on the description of a generic two-level state from Ref. [29] we can conclude that the angle θ of this rotation axis is a result of the ratio of the drive term and the detuning

$$\tan(\theta) = \frac{\alpha_0}{\Delta\omega} \tag{3.68}$$

allowing for a maximum excited state probability of

$$P_{\text{max}} = \frac{4\alpha_0^2}{4\alpha_0^2 + (\Delta\omega)^2} \tag{3.69}$$

For a typical transmon the detuning is set by the nonlinearity $\eta/2\pi \approx 200\,\text{MHz}$, and the typical X or Y rotation time is of order $t_{\text{gate}} = 25\,\text{ns}$, which for a constant drive would make $\alpha_0/2\pi \approx 10\,\text{MHz}$. Using Eq. 3.69 we calculate that with a simple square wave pulse we could induce an error with a probability of order 1 percent.

Fortunately, this error can be drastically reduced through more careful application of pulse shaping to the qubit drive [31, 32, 33]. In this scheme, the constant voltage term V_0 is multiplied by a slowly varying envelope function $e(t)$. If chosen carefully, such a shaped drive pulse will execute a complete rotation from the $|0\rangle$ to the $|1\rangle$ state with a rotation angle of

$$\frac{1}{\hbar} Q_{\text{zp}} \frac{C_c}{C} \frac{V_0}{2} \int_0^t e(t')dt' \approx \frac{\pi}{2}. \tag{3.70}$$

At the same time this shaped pulse ensures rotations of the $|1\rangle$ to the $|2\rangle$ state are negligible

$$\frac{1}{\hbar} Q_{\text{zp}} \frac{C_c}{C} \frac{V_0}{2} \int_0^t e(t') \cos(\eta t')dt' \approx 0, \tag{3.71}$$

$$\frac{1}{\hbar} Q_{\text{zp}} \frac{C_c}{C} \frac{V_0}{2} \int_0^t e(t') \sin(\eta t')dt' \approx 0. \tag{3.72}$$

By combining cosine shaped pulses and the DRAG protocol [33], superconducting qubit systems have reduced the $|2\rangle$ state error per gate below 1×10^{-4} [33], and as low as 1×10^{-5} is more recent (unpublished) work.

While superconducting qubits can execute high fidelity single qubit rotations, this is not enough to conduct a BLGI experiment. To do this we also require a high fidelity two-qubit entangling gate. In superconducting qubit systems this can be accomplished with the adiabatic

C-phase gate [34]. This gate however, requires an ability to tune the qubit frequencies dynamically. In addition to a good two-qubit gate, frequency tunability would also allow us to avoid frequency crowding in multi-qubit systems.

We can incorporate this tunability into the transmon circuit by replacing the single Josephson junction with a DC SQUID, consisting of two junctions on opposite branches of a superconducting loop. If both junctions in the loop have the same critical current then the SQUID has the same current phase relationship as a single junction but with a tunable critical current described by the equation

$$I_{max} = 2I_c|\cos\left(\frac{\pi\Phi_{\text{ext}}}{\Phi_0}\right)| \tag{3.73}$$

Where I_c is the critical current of each junction in the loop and Φ_{ext} is an externally applied flux. Since the qubit frequency is proportional to the square root of the critical current, we can tune the qubit frequency down from a maximum value at $\Phi_{\text{ext}} = 0$, towards zero frequency when $\Phi_{\text{ext}} = \Phi_0/2$. The two-qubit C-phase gate along with single qubit X and Y rotations, are all the gates necessary for a BLGI experiment. Additionally, all these gates have been demonstrated with greater than 99 percent fidelity in randomized bench marking of a 5 qubit chip [27].

3.2.2 State readout

The last element necessary to conduct a BLGI experiment is an effective method of qubit state readout. In superconducting qubits this is typically accomplished through the dispersive interaction [24] between a qubit and a linear resonator. This interaction can be engineered

through capacitave coupling of the qubit and resonator, shown in Fig 3.5, and is described by the Jaynes-Cummings Hamiltonian [35]

$$\hat{H} = \hbar\omega_r a^\dagger a + \frac{\hbar\omega_q}{2}\sigma_Z + \hbar g(\sigma^+ a + \sigma^- a^\dagger). \tag{3.74}$$

This Hamiltonian consists of the resonator energy term, the qubit energy term, and an interaction term with coupling energy $\hbar g$, which models the interaction between a two-level state and the electric field in a resonant cavity. In this expression, the ground state energy of both the qubit and resonator has been scaled out, such that the energy depends only on photon occupation in either circuit. The coupling term g is derived from the coupling capacitor C_g, the circuit capacitance of the qubit C_q and resonator C_r, and the resonant frequencies of both circuits. In the typical limit where $C_q, C_r \gg C_g$ the term can be written simply as

$$g \approx \frac{C_g}{2\sqrt{C_q C_r}}\sqrt{\omega_q \omega_r}. \tag{3.75}$$

As this term is much smaller than either the qubit or resonator frequency, we can treat the interaction term as a perturbation on the Hamiltonian. After calculating the effect of this term to second order in perturbation theory, we get energy corrections which depend on both the qubit state and the resonator photon number n. Grouping these terms together based on their associated state, we can write a new Hamiltonian which describes the state dependent energy shifts in the system

$$\hat{H}' \approx \hbar\omega_r a^\dagger a + \frac{\hbar\omega_q}{2}\sigma_Z + \hbar\chi a^\dagger a \sigma_Z \tag{3.76}$$

where $\chi = g^2/\Delta$ and $\Delta = \omega_r - \omega_q$. In practice however, we must include the $|2\rangle$ state of the qubit in such a calculation, which leads to a correction factor based on the qubit anharmonicity

η. After including these corrections χ is described by

$$\chi = \frac{g^2}{\Delta}\frac{\eta}{\eta + \Delta}. \tag{3.77}$$

The full calculation of χ is discussed in Ref. [30]. The importance of this energy correction to the Hamiltonian is that it can be thought of as a state dependent frequency correction to either circuit. We can see this by grouping the correction term together with the resonator energy term, which gives us

$$H' = \hbar(\omega_r + \chi\sigma_Z)a^\dagger a + \frac{\hbar\omega_q}{2}\sigma_Z. \tag{3.78}$$

This is equivalent to a shift in the frequency of the resonator by 2χ which depends on the state of the qubit. As we saw in the previous section, voltage driving this linear resonator with a capacitively coupled drive line populates it with a semi-classical coherent state. Let us also postulate that the dispersive frequency shift is engineered such that $2\chi \approx \kappa$, where κ is the bandwidth of the resonator. In this case, a probe tone applied between the two possible resonant frequencies, shown in Fig. 3.5, will pick up a phase shift from the resonator which depends directly on the state of the qubit. This phase shift, encoded on the large coherent drive of the resonator, can then be measured with a classical detector to infer the state of the qubit.

Given the symmetry of the dispersive coupling, there is also a measurement dependent back action on the qubit. Just as the resonator frequency depends on the qubit state, the qubit frequency depends on the number of photons in the resonator. This can be seen by grouping the terms in the Hamiltonian

$$H' = \hbar\omega_r a^\dagger a + \hbar\left(\frac{\omega_q + 2\chi a^\dagger a}{2}\right)\sigma_z. \tag{3.79}$$

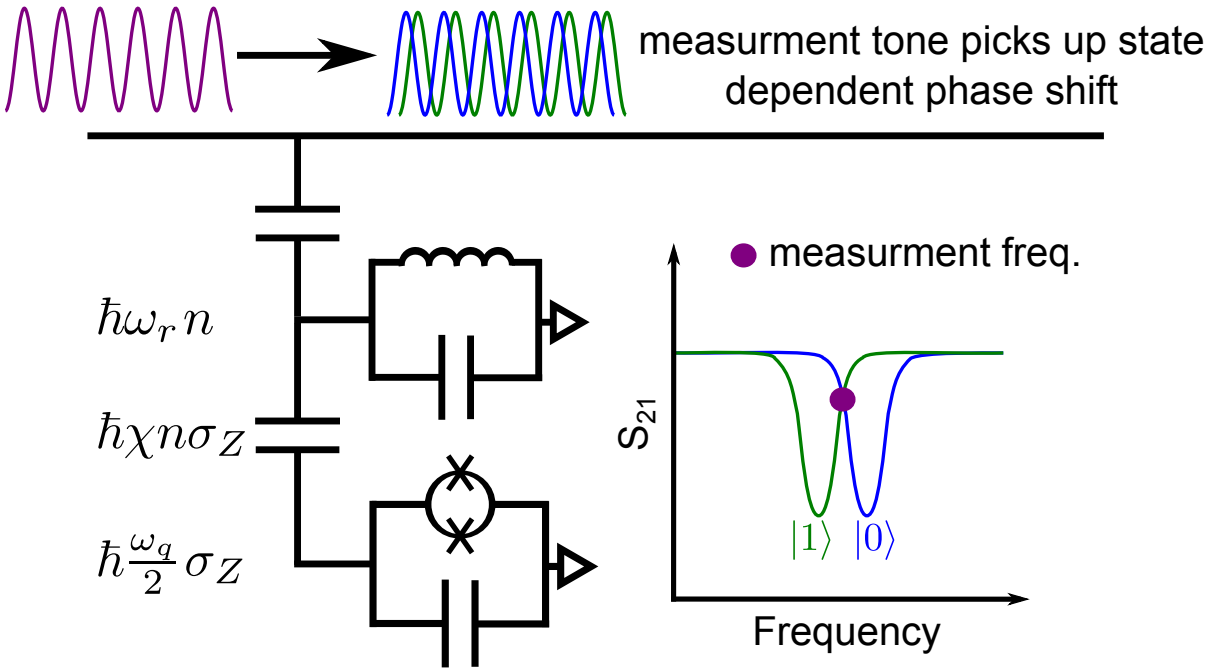

Figure 3.5: Diagram of dispersive readout of a superconducting qubit. The qubit is capacitively coupled to a linear LC resonator which is capacitively coupled to a transmission line. The joint Hamiltonian has independent terms for the qubit, the resonator, and a coupling term which describes how energy in either circuit shifts the frequency of the other. By picking a measurement frequency in between the two possible resonator frequencies the probe tone picks up a qubit state dependent phase shift, which can be measured by a room temperature detector.

When driving at the intra-resonator frequency used in dispersive readout, each photon in the resonator shifts the qubit frequency by 2χ in what is known as the AC Stark shift [36]. An important difference between the two circuits, is that the resonator is typically populated with many tens of photons, leading to much larger frequency shifts in the qubit. As the number of photons in the resonator increases, this back action can produce state transitions in the qubit [28]. Such state transitions are not well understood and can leave excess $|1\rangle$ state population in the qubit, requiring a longer cool down period between iterations of an experiment. This creates constraints on the power used in dispersive readout which will be discussed in the next chapter.

3.3 Conclusion

Superconducting qubit systems, because they provide all the elements necessary for a general quantum processor, are an excellent system for conducting our BLGI experiment. High fidelity single-qubit gates have been demonstrated with the straight forward application of microwave control tones. DC control tones provide high fidelity two qubit gates, and allow for tunable frequency spacing in complex coupled qubit systems. Lastly the dispersive interaction between a qubit and a linear resonator allows one to easily turn measurement on and off for individual qubits. Measuring this dispersive readout signal at room temperature however, is a distinct and difficult challenge. The the AC stark shift limits the power of the measurement tone we can apply. Typical measurement power is far below the measurement threshold of room temperature electronics, and requires significant amplification. In the next chapter, we discuss some of the

constraints on dispersive readout and the role of the microwave amplifier chain in high fidelity qubit measurement.

Chapter 4

Dispersive readout and the microwave amplifier chain

For inequality experiments like the BLGI, a violation requires non-classical correlations in an ensemble of measurements. Experimental errors which might affect these measurement statistics are troubling because they can lower the maximum possible violation, or if corrected for, introduce potential loopholes. In the previous chapter we discussed how state readout in superconducting qubit systems is accomplished through the dispersive interaction of the qubit and a linear resonator. In this chapter, we will discuss some of the experimental details of dispersive readout and how they relate to the BLGI. In particular we will discuss the difference between measurement efficiency and measurement visibility, as well as the role of supplemental technologies like microwave amplifiers which are crucial for high fidelity measurement.

4.1 Quantum state detection: efficiency vs visibility

4.1.1 Disepersive readout is naturally efficiency

When describing the effectiveness of qubit state detection there are two important but subtly different concepts. The first of these concepts is measurement efficiency, which depends on the likelihood of detecting a null result when conducting a measurement. In optical inequality experiments involving detection of single photons, there are often loses in the system which absorb incoming photons. In some cases only a relatively small fraction of the emitted photons are ever detected. As such, correlation measurements between two photons are scaled by the probability of detecting any photon at all. This is the basis of the fair sampling [9] and disjoint sampling [10] loophole discussed in chapter 1. On the other hand, the dispersive interaction of the qubit and resonator couples the qubit state to every photon entering the resonator. Even if some of the photons are absorbed the state can still be detected by simply measuring longer or increasing the signal power. Thus superconducting qubits hold an advantage over many quantum systems in that the method of dispersive readout has extremely high intrinsic detection efficiency.

4.1.2 Visibility is key

The second factor to consider in qubit state readout is the visibility of the measurement. Visibility refers to the difference between the maximum probability of measuring the $|0\rangle$ state and the maximum probability of measuring the $|1\rangle$ state. High visibility measurement is important

because the amplitude of the BLGI correlator $\langle C \rangle$, is particularly sensitive to single qubit measurement visibility. Even with no additional sources of error, the single qubit visibility must exceed 90 % for a robust violation [37]. While the measurement probabilities can be re-scaled for unit visibility, this introduces another potential BLGI loophole and should be avoided. To ensure a robust violation and to account for other sources of error, we should strive for a single qubit measurement visibility of 97 % or greater. With this goal in mind, there are certain constraints on the measurement due to the fundamental qubit physics.

The first of these constraints comes from spurious $|1\rangle$ state population in the qubit. As we saw in the previous chapter, for typical excitation frequencies and operation temperatures the qubit should idle in the ground state. While most algorithms assume this to be the case, there is often a small probability that the qubit begins in the excited state, which alters its behavior throughout the algorithm [38]. If nothing is done to address this, the excited state probability reduces visibility symmetrically for both states. One of the most effective ways to deal with this spurious $|1\rangle$ state population is to use heralding [39], in which a measurement is conducted before and after the algorithm. By discarding every iteration in which the qubit is initialized in the $|1\rangle$ state, we can prevent this spurious excited state population from affecting the BLGI measurement. For this method to be effective, we must ensure the measurement itself does not change the state of the qubit. As we discussed in the previous chapter, back action from dispersive readout can cause these state transitions if the probe signal is used with too much power [28]. For the purposes of this chapter, let us assume a safe limit of about 50 resonator photons during steady state measurement.

The second physical constrain on dispersive measurement comes from the coherence time T_1 of the qubit. For any finite T_1, there is a probability that the qubit state can decay from the excited state to the ground state during the measurement. This represents a loss of visibility which only affects the $|1\rangle$ state but can become significant if the measurement takes too much time. Assuming our visibility threshold of over 97 %, we can calculate a rough time limit given an average qubit coherence time $T_1 \approx 30\,\mu s$. Assuming this time, the measurement of a qubit state should not exceed $\sim 1\,\mu s$. This is a reasonable threshold given the typical bandwidth of readout resonators is of order $\kappa \approx 1/1\,\mu s$ [40]. This bandwidth sets the "ring up" time of the resonator, which is roughly the time required for the photons entering and leaving the resonator to reach equilibrium [41], and for sufficient state information to be accumulated.

The final constraint on visibility in our system is the fidelity of the underlying measurement itself, defined as the probability that a given measurement correctly identifies the qubit state. For example, if the fidelity of the measurement is 90 % then a detector will identify a qubit in the $|1\rangle$ state as being a $|0\rangle$ state 10 % of the time. In dispersive readout, this error probability is symmetric for both states so that the decrease in visibility is twice the error rate of the measurement. Given the constraints imposed by the qubit physics on signal power and measurement time, much of the difficulty in achieving high measurement fidelity is in improving the sensitivity with which this signal is measured. To describe this quantitatively, we must understand the relationship between errors, signals, and noise.

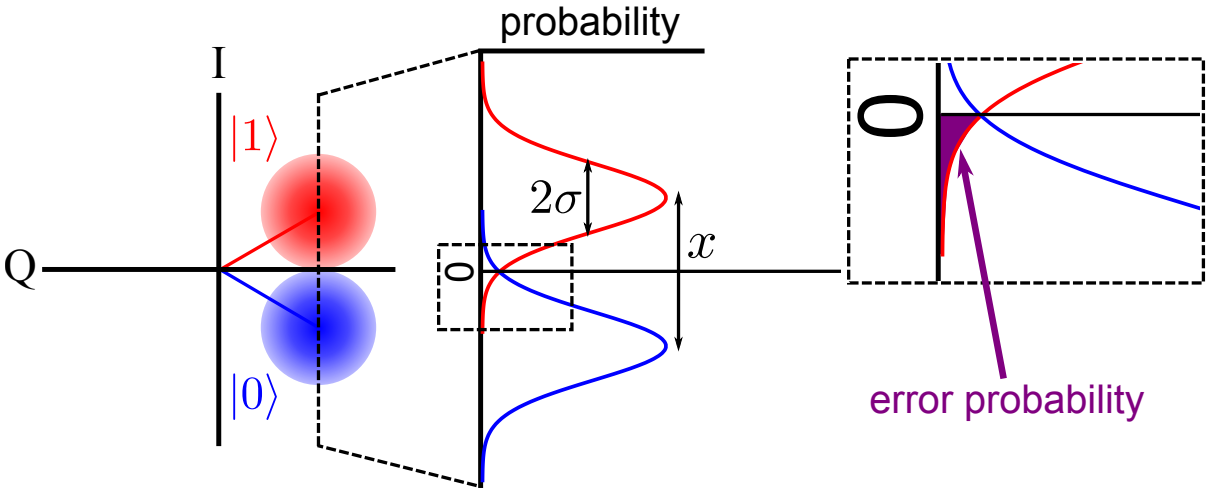

Figure 4.1: Diagram of state dependent resonator signals plotted on the IQ-*plane* and the error rate which results from overlap of the Gaussian distributions. The center of the blobs depend on the amplitude and phase of the measurement probe tone. The magnitude of the Gaussian distributed noise directly depends on the signal to noise ratio of the measurement. The error rate depends on the overlap of between the Gaussian distributions and the measurement threshold chosen.

4.2 Separation fidelity and signal to noise ratio

In dispersive readout, a microwave probe tone enters the resonator and acquires a phase shift depending on the state of the qubit. If we then mix this theoretical signal, with amplitude V and phase ϕ, to zero frequency it represents a single point on the IQ plane. A measurement of this point is then effectively a measurement of the qubit state. In a real experimental detector, this simple picture is complicated by a background of white noise coming from voltage fluctuations in the system [42]. An actual measurement of the output signal produces a spread of possible IQ values with a Gaussian distribution, whose center is described by V and ϕ. If the distance between the center of the $|0\rangle$ state distribution and the center of the $|1\rangle$ state distribution is equal to x, then we can define a threshold axis which is a distance $x/2$ from each center. Any point on one side of the axis is considered a $|0\rangle$ state measurement, and any point on the other

Table 4.1: Evaluation of separation error ϵ *vs.* SNR

parameter	1	2	3	4	5	6	7
SNR	0.5	1	2.5	5	10	20	40
ϵ	0.309	0.240	0.132	0.057	0.013	7.82e-4	3.87e-6

side is considered a $|1\rangle$ state measurement. An illustration of a set of IQ blobs is shown in Fig 4.1, evenly distributed on either side of the Q axis of the IQ plane. In this case the line $I = 0$ is a natural threshold for our measurement. For this example, the spread in each data set means that there is a slight overlap in the two distributions. The measurement fidelity thus be described as a separation fidelity which depends on the size of this overlap.

The separation fidelity in this example can be calculated by integrating over the Gaussian distribution of signals on the "wrong" side of the threshold. While the actual distribution is two dimensional, we can more easily understand the scaling by considering the error in I along the line connecting the center of both blobs. In this one dimensional calculation, the probability of accidentally measuring a $|1\rangle$ state signal when the qubit is in the $|0\rangle$ state is described by a guassian distribution of width σ

$$\epsilon = \frac{1}{\sqrt{2\pi\sigma^2}} \int_0^\infty e^{\frac{-(I+x/2)^2}{2\sigma^2}} dI. \tag{4.1}$$

Here the threshold is at I=0, the state blobs are centered at $I = \pm x/2$. By a substitution of variables and some minor algebra we can rewrite the integral as the special function erfc.

$$\epsilon = \frac{1}{2}\text{erfc}\left[\frac{x}{2\sqrt{2}\sigma}\right]. \tag{4.2}$$

From this we can see that the separation fidelity depends directly on the ration of x and σ.

In this measurement the distance between each blob and the center of the IQ plane is equivalent to the voltage amplitude V of the signal. The power from such a signal is equivalent to $V^2/2Z$ where Z is the impedance of the room temperature detector. Similarly the power of the noise signal is equivalent to the variance divided by the impedance of the room temperature detector σ^2/Z. In this case the signal to noise ratio or SNR in units of power is described by $V^2/2\sigma^2$. The distance between the state blobs x is generally related to the voltage amplitude a trigonometric factor depending on the relative phase shift of both blobs. To simplify the analysis here, we will simply assume that $V \approx x$ and SNR $\approx x^2/2\sigma^2$. Using this we can make the substitution

$$\frac{x}{2\sqrt{2}\sigma} \approx \frac{\sqrt{\text{SNR}}}{2}, \tag{4.3}$$

such that

$$\epsilon \approx \frac{1}{2}\text{erfc}\left[\frac{\sqrt{\text{SNR}}}{2}\right]. \tag{4.4}$$

Thus, given a reasonable geometric correction factor from a properly engineered phase shift, the separation fidelity is a simple function of the signal to noise ratio of the microwave probe tone. The value of ϵ *vs.* SNR is shown for various values in the table 4.1.

4.3 Signals and noise

4.3.1 Comparing in units of power

To understand the signal to noise ratio of our measurement system, we must be able to compare the contributions of all the various signals and noise sources. Up to this point, we have generally described coherent microwave signals as either sinusoidal voltage drives, or in the case of a linear resonator, coherent states with average photon number n. In large microwave systems however, it is often more advantageous to consider the signal in units of power. As we saw in the last section we can describe the power of a voltage drive as $P = V^2/2Z$. Here Z is the impedance of the environment, which for most commercial hardware is $Z = 50\,\Omega$. For a resonant circuit we can convert between drive power and photon number using the formula $P = n\hbar\omega B$ where B is the bandwidth of the resonator. This gives us as easy way to convert between two different types of signals in our system, the voltage amplitude of a classical drive pulse and the photon population of a quantum harmonic oscillator. Additionally, power is usually converted into the logarithmic dBm scale described by

$$P_{\text{dBm}} = 10\log_{10}\left(1000 P_{\text{watts}}\right), \tag{4.5}$$

for which 0 dBm is 1 mW of power. This allows easy comparison of signals across many orders of magnitude, which is important in superconducting qubit experiments where many levels of attenuation or amplification are necessary to properly isolate the qubit.

Noise in the system is typically described by the spectral density function $S(\omega)$, which has units of power per Hertz bandwidth or energy. At microwave frequencies in our system

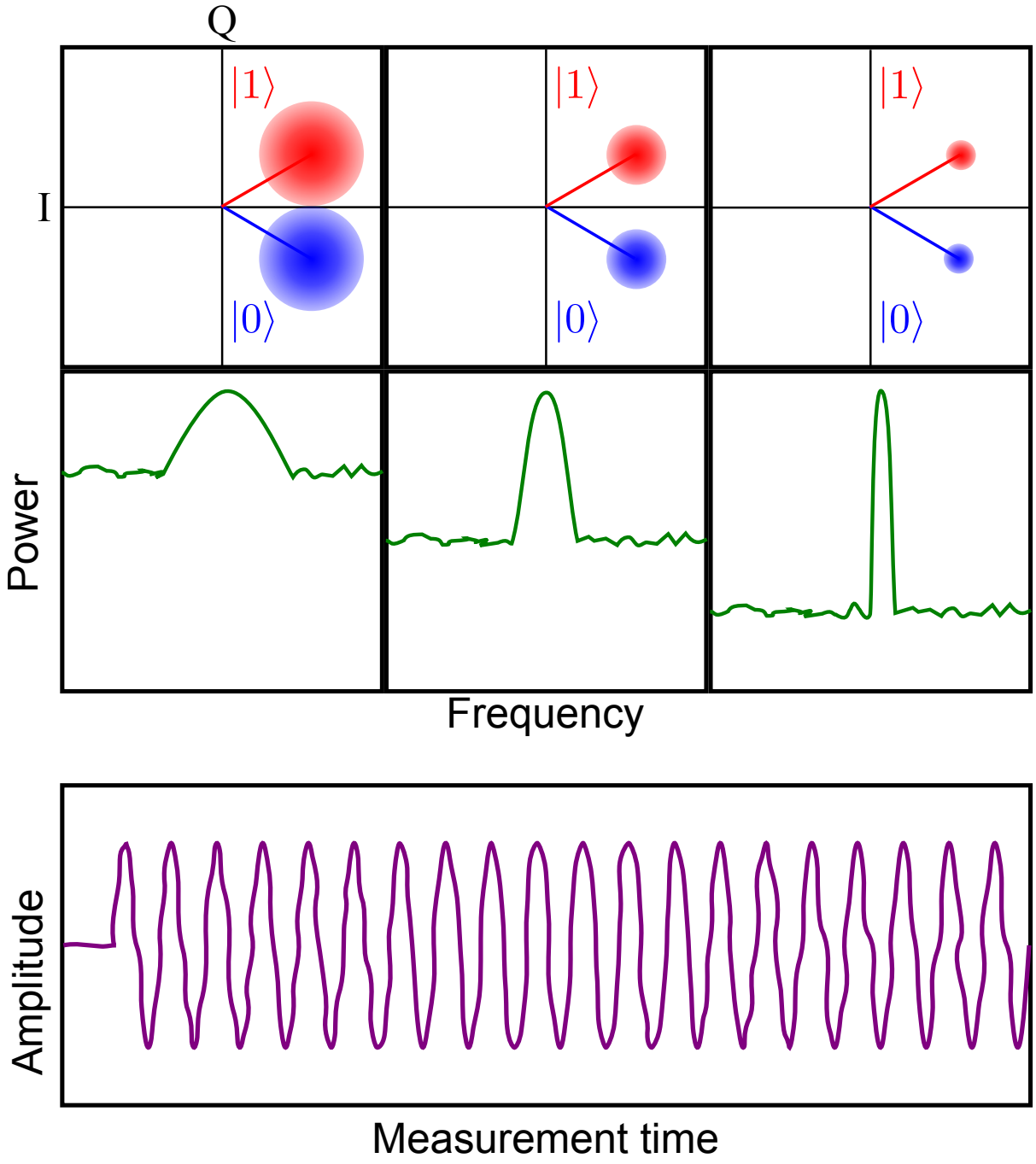

Figure 4.2: Dependence of noise power on measurement time for different kinds of signal processing. Given a coherent signal with background white noise spectral density $S(\omega)$, the noise power is simply $S(\omega)$ times the resolution bandwidth B which is given by $B = 1/t_{\text{meas}}$. If a signal is being measured on the *IQ-plane* then decreasing the noise power has the effect of shrinking the spread of the Gaussian measurement distributions around their average value. For a measurement in the frequency domain, a longer measurement time allows us to decrease the noise background while also increasing our resolution of the signal frequency.

the noise is white noise resulting from the thermal (kT) or quantum ($\hbar\omega/2$) fluctuations of electrons in the $50\,\Omega$ environment. The spectral density of this noise is given by the general equation

$$S(\omega) = \frac{\hbar\omega}{2}\coth\left(\frac{\hbar\omega}{2kT}\right). \tag{4.6}$$

From this formula we can see that the magnitude of the background noise in a system depends on both the temperature and the frequency being measured. For typical qubit experiments $\hbar\omega \gg kT$ so $S(\omega) \approx \hbar\omega/2$. For white noise, we can convert the spectral density into a noise power by multiplying $S(\omega)$ by a measurement bandwidth B which has units of $1/t$ [42]. If this bandwidth is set by a physical object like a filter, then fluctuations at frequencies too low or too high are rejected by the filter. Similarly, the resolution bandwidth of a detector can be set by changing the integrating time of the signal. In this case the resolution bandwidth $B_{\text{meas}} = 1/t_{\text{meas}}$ comes from Fourier transforming the time domain signal. As the measurement time increases noise fluctuations at higher and lower frequencies average to zero, because a mathematical filter of shrinking bandwidth is applied to the signal. The effect of increasing measurement time is shown in Fig. 4.2, for various kinds of signal analysis. In both cases, increasing the measurement time is to decreases the magnitude of the background noise power and the variance in the signal.

4.3.2 Amplifiers and detectors.

In addition to the environment noise, there is noise added to the signal by active elements like amplifiers and detectors. While each active device adds noise to the signal in a nontrivial and

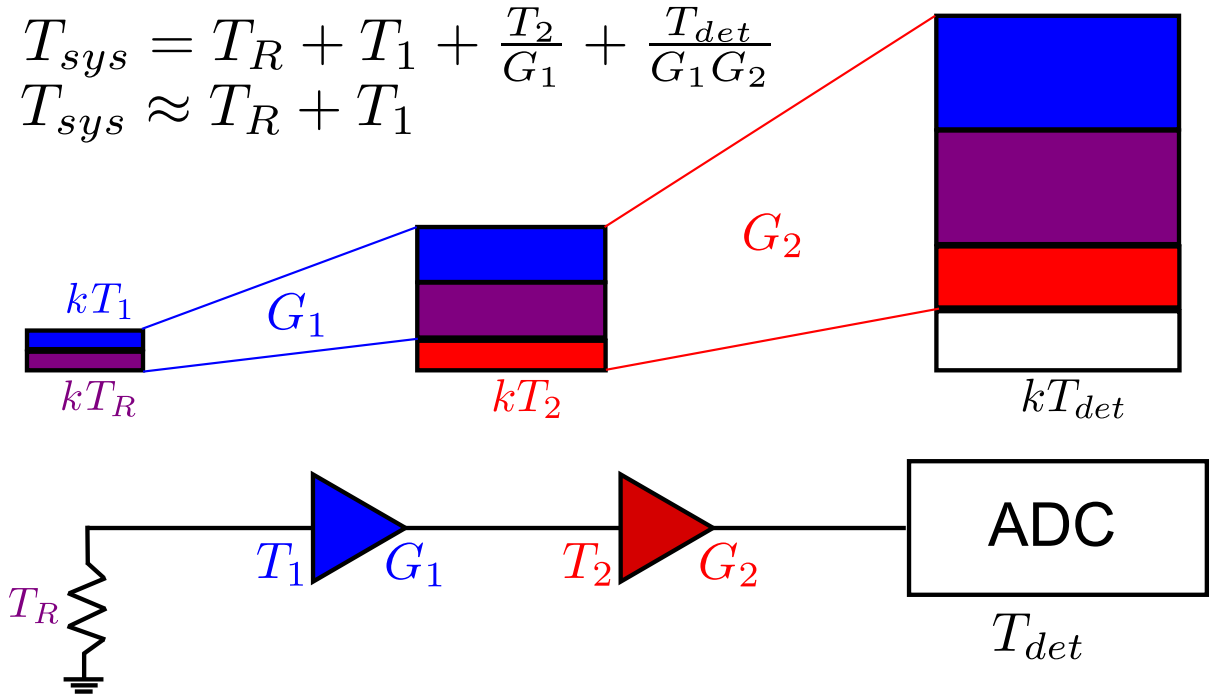

Figure 4.3: Noise scaling in a typical microwave measurement chain. The System noise temperature includes the noise added at each stage, scaled by the gain between the original signal and that point in the chain. Ideally the gain of each amplifier is much larger than the input noise the the following amplifier. In this case the system noise temperature is set by the environment and the input referred noise of the first amplifier.

distinct way, as long as the noise is smooth in frequency it can be reduced to a system noise temperature for each device. This has the benefit of making the noise from each element easy to compare to all other elements. In the case of an amplifier with gain G_{amp} and bandwidth B_{amp}, one can describe the output noise power in terms of the noise temperature with the expression $G_{\text{amp}}(kT_{\text{amp}}B_{\text{amp}})$. The term T_{amp} now describes what is known as an input referred noise temperature. If a signal enters the amplifier with power P_{sig}, the output of the amplifier is $G_{\text{amp}}(P_{\text{sig}} + kT_{\text{amp}}B_{\text{amp}})$. Similarly, for a detector with variable bandwidth B_{meas} and input referred noise T_{det} measuring a coherent signal P_{sig}, the signal to noise measure would be described $P_{\text{sig}}/(kT_{\text{det}}B_{\text{meas}})$.

For dispersive qubit measurements, the signal is typically measured at room temperature with an analogue to digital converter (ADC). The average input referred noise of an ADC is on the order of 10^5 K, which is far too high to measure the raw signal coming out of the superconducting chip. To overcome this we can add amplifiers that operates with a lower input referred noise, and a high enough gain to amplify the signal far above the noise temperature of the next stage. The schematic in Fig. 4.3 demonstrates this concept with a resistor, two amplifiers, and a detector. For each stage, there is a signal power and an input referred noise for that amplifier/detector.

For typical cryogenic microwave measurements the cold amplifier consists of a high electron mobility transistor (HEMT) amplifier [43] with an input referred noise temperature of 2-5 K and 40 dB of gain. In addition to this, our room temperature amplifier has an input referred noise temperature of about 200 K and 60 dB of gain. In this case our signal is the noise

from the cryogenic resistor which we shall label simply kT where T is the physical temperature in the system. If the input noise of our detector is 10^5 K, and the gain of the room temperature amplifiers is 60 dB, then the effective noise from the detector at the amplifier input is $10^5 K/10^6 = 0.1K$. Thus the contribution from the detector is negligible when compared to the input noise of the amplifier. Similarly, the noise due to the room temperature amplifier at the input of the HEMT is $200/10^4 = 0.02$ K, which is negligible compared to the noise of the HEMT. Our total noise power at room temperature is then just $P_{\text{meas}} \approx G_{\text{HEMT}} G_{\text{RT}} K(T + T_{\text{HEMT}}) B_{\text{meas}}$. Thus noise temperature gives us a simple way to relate noise and signal power at many different stages of measurement. From this we can see that for a properly designed amplifier chain, the system noise temperature T_{sys} is set by the first amplifier in the chain and the noise of the environment.

4.4 Signal to noise ratio in dispersive readout.

With our understanding of the signal and noise in microwave measurement, we can calculate the separation fidelity possible in an actual dispersive measurement. First recall the equation for separation fidelity Eq. 4.4 where SNR is the power ratio of our coherent probe tone and the system noise. First we must apply the constraints we discussed on signal power and measurement time coming from the fundamental qubit physics. As we discussed in the previous section on visibility, the back-action during dispersive readout sets a limit on the number of photons in the resonator which is determined experimentally to be around 200 photons [28]. For the purpose of this analysis we shall assume a limit of about 50 photons. For a typical resonator

bandwidth and frequency of 1.5 MHz and 6.5 GHz respectively, this corresponds to a signal power of order -125 dBm. Similarly, T_1 decay requires that we complete the measurement in less that $1\,\mu s$. This then sets our measurement bandwidth at $B_{\text{meas}} = 1/t_{\text{meas}} = 1$ MHz. Given these constraints on signal power and measurement bandwidth, the last parameter needed to determine the separation fidelity is the system noise temperature.

Since we can expect a slight loss of visibility due to T_1 decay, let us determine the system noise temperature which will allow us to achieve ~ 99.9 percent separation fidelity. Plugging in numbers to Eq. 4.4 we reach the desired separation at $SNR \approx 20$. This number can then be directly calculated using the formula

$$\text{SNR} = \frac{P_{\text{sig}}}{k_B T_{\text{sys}} B_{\text{meas}}} \tag{4.7}$$

$$T_{\text{sys}} = \frac{P_{\text{sig}}}{k_B \text{SNR} B_{\text{meas}}}, \tag{4.8}$$

which is our case is $T_{\text{sys}} \approx 1.2\,K$. As stated before, the environment noise in qubit experiments is set by the quantum fluctuations. For 6.5 GHz the ground state fluctuations correspond to a noise temperature of about $\hbar\omega/2k \approx 150$ mK. If we subtract this value from the system noise, we see that the input noise of the first amplifier should be about 1 K. While the HEMT has sufficient gain to overcome higher stage amplifiers, the best noise temperature quoted by HEMT manufacturers is just over 2 K. Additionally The input noise of an amplifier can vary from system to system. To properly claculate our signal to noise ratio, we must conduct a measurement of the HEMT noise.

To measure the system noise in our setup, shown in Fig. 4.4, we use a Y-factor measurement

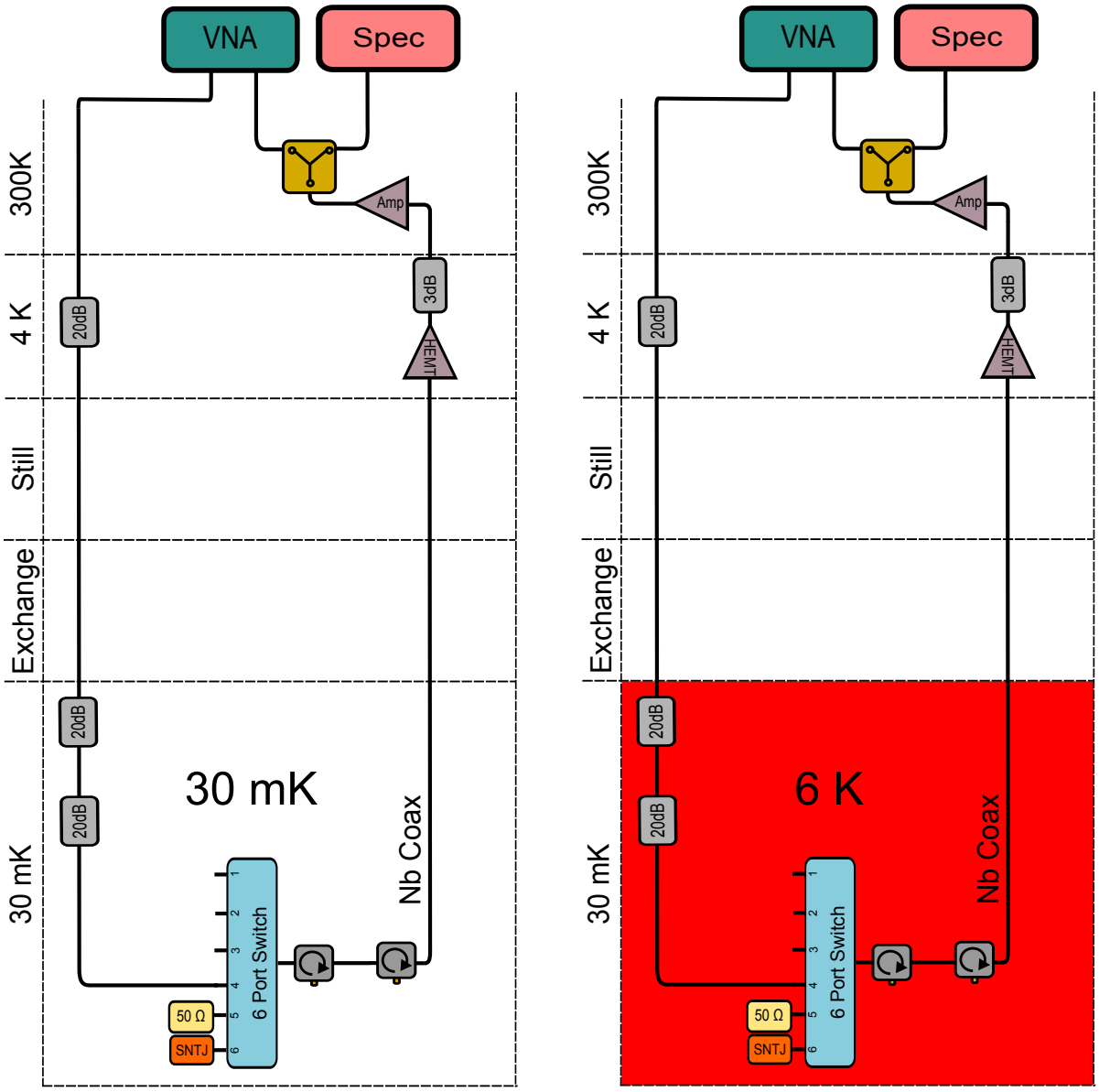

Figure 4.4: Schematic for experimental setup used to characterize noise. The left figure shows the experimental setup with and microwave switches and circulators at base temperature. The 6-port switch is used to switch between a signal line used to characterize gain, and a 50 Ω terminator which is heated to calibrate the HEMT noise. The right schematic shows the portion of the fridge heated (red) to perform a Y-factor measurement. The two circulators provide directional transmission, allowing signals to pass to the HEMT with negligible loss while preventing HEMT noise from propagating qubit sample. As circulators are the dominant source of loss, they must be included when calibrating the HEMT noise temperature.

[41] with a heated 50 Ω resistor on the cold plate of our dilution refrigerator. The Y-factor is calculated by measuring the output noise power of a 50 Ω resistor at two different temperatures. For a system gain G_{sys} and HEMT noise temperature T_{HEMT} the power measured by our room temperature detector is described by

$$P_{\text{hot}} = G_{\text{sys}} k_B B_{\text{meas}} (T_{\text{hot}} + T_{\text{HEMT}}) \tag{4.9}$$
$$P_{\text{cold}} = G_{\text{sys}} k_B B_{\text{meas}} (T_{\text{cold}} + T_{\text{HEMT}}) \tag{4.10}$$

Assuming we can accurately measure P_{hot}, P_{cold}, T_{hot}, and T_{cold}, we can reduce this to an equation with only one unknown given by

$$T_{\text{HEMT}} = \frac{T_{\text{hot}} - \frac{P_{\text{hot}}}{P_{\text{cold}}} T_{\text{cold}}}{\frac{P_{\text{hot}}}{P_{\text{cold}}} - 1}. \tag{4.11}$$

In this setup the 50 Ω resistor is connected to the HEMT by copper microwave flex cables at 30 mK, 2 circulators, and a Nb coaxial cable connected between 30 mK and the HEMT at 4 K. Due to the difficulty of heating just the 50 Ω resistor we use a method in which the entire cold plate of the refrigerator in heated to a much larger temperature (6 K) and allowed to stabilize before a measurement is performed. The HEMT amplifier is on a different plate and its temperature is held steady over the course of this experiment. This methodology, while allowing for accurate temperature measurement of the resistor, can mis-characterize the effect of loss between the resistor and the HEMT. Any dissipative loss on the 30 mK plate would add noise to the signal as it was also at the higher 6 K temperature. In this case, we assume the dominant source of loss comes from the microwave circulators, as the superconducting and copper cables should have negligible loss at these temperatures. The circulator insertion loss was measured at room temperature to be between 0.5 and 0.3 dB. Using this method the

HEMT noise was measured to be between 2.1-2.2 K, which is in good agreement with the quoted commercial values. This is roughly a factor of two larger than the 1 K needed and would lower the separation fidelity to roughly 99 %.

While 99 % separation fidelity is not particularly bad, there are additional losses between the qubit and the HEMT which are not accounted for in a Y-factor measurement. The qubits require extensive filtering to shield them from decoherence mechanisms like high frequency radiation [44]. Additionally, elements in the chip packaging like wire bonds can cause standing waves which further reduce signal power. In a realistic experiment, there can be as much as 6 dB of signal loss between the readout resonator and the input of the amplifier [28]. Just as signal gain decreases the noise added by later stages, signal loss will make this noise appear larger. Including this loss in our analysis the system noise due to the HEMT would be of order 8.4-8.8 K. This system noise gives us a separation fidelity below 90 %, or a visibility of only 80 %, making a violation of the BLGI impossible.

4.5 The quantum limit

As we saw in the previous section, we require a system noise temperature of around 1-2 K which includes the 6 dB of loss from the qubit filters and connectors. From this we can calculate that our first amplifier must have a total input referred noise of about 300-500 mK at frequency $\omega/2\pi = 6.5$ GHz. For a phase insensitive amplifier, in which the phase of the incoming signal has no effect on the gain of the amplifier, this represents the lowest possible noise we can achieve as determined by the quantum limit [45]. To see why this is the case, we can write

down the general equations for a phase insensitive amplifier that couples input photons (a,$a^\dagger$) to output photons (b,$b^\dagger$). These amplifier equations consist of

$$b = Ma + La^\dagger + \mathcal{F} \tag{4.12}$$
$$b^\dagger = M^* a^\dagger + L^* a + \mathcal{F}^\dagger \tag{4.13}$$

where the term M represents a phase preserving gain, the term L represents a phase conjugating gain, and the term $\mathcal{F}$ corresponds to any possible internal amplifier mode which might add noise. As both a and b are photons, we know that $[a, a^\dagger] = [b, b^\dagger] = 1$. If we rewrite the amplifier equations in terms of these commutation relations, we get

$$[b, b^\dagger] = |M|^2[a, a^\dagger] + |L|^2[a^\dagger, a] + [\mathcal{F}, \mathcal{F}^\dagger] \tag{4.14}$$
$$1 = |M|^2 - |L|^2 + [\mathcal{F}, \mathcal{F}^\dagger]. \tag{4.15}$$

From this we can see that unless the total gain of the amplifier is $|G|^2 = |M|^2 - |L|^2$ is one, the noise fluctuations described by $[\mathcal{F}, \mathcal{F}^\dagger]$ must be non-zero.

From the uncertainty principle we know that the noise fluctuation term obeys the bound

$$(\Delta\mathcal{F})^2 \geq \frac{1}{2}|[\mathcal{F}, \mathcal{F}^\dagger]| \tag{4.16}$$

With this we can calculate the minimum added noise from a phase insensitive amplifier as

$$(\Delta\mathcal{F})^2 \geq \frac{1}{2}|1 - |M|^2 + |L|^2| \tag{4.17}$$
$$(\Delta\mathcal{F})^2 \geq \frac{1}{2}|1 - |G|^2|. \tag{4.18}$$

Thus the minimum value of the noise added from the term $\mathcal{F}$ is a half photon multiplied by the gain of the amplifier. If we then include the half photon of noise coming from quantum

fluctuations in the system, we get a quantum limit on the system noise of $T_{\text{sys}} = \hbar\omega$. For a phase insensitive amplifier measuring signals at a frequency $\omega/2\pi = 6.5\,\text{GHz}$ the quantum limit of noise is $T_{\text{sys}} = \hbar\omega/k \approx 300\,\text{mK}$. If we include the loss due to qubit filters, this puts us right at the $1.2\,\text{K}$ system noise temperature we require. A more detailed discussion of the quantum limit, including phase sensitive amplification can be found in Ref. [45].

4.6 Conclusion

From this analysis we can draw several conclusions about the effectiveness of dispersive readout in superconducting qubit systems. Dispersive readout has an efficiency approaching unity, because the a qubit state is always detected. To improved the fidelity we can increase the signal to noise ratio by using more signal power or measuring for longer. There are however, constraints on the signal power and measurement time which come from the fundamental physics of the qubit. If we include these constraints into our analysis it becomes clear that we require an amplifier which operates at or near the quantum limit of added noise. Additionally, this amplifier must have enough gain to overcome the noise added by the HEMT amplifier which follows it. In the next chapter we will discuss the Josephson parametric amplifier and its role as a quantum limited amplifier for superconducting qubit readout.

Chapter 5

Design and characterization of a lumped element Josephson parametric amplifier

As discussed in the previous chapter, the nature of dispersive readout puts certain limitations on the total system noise of the microwave readout chain. In particular for high visibility measurements we require a system noise level that is at or near the qauntum limit. At the microwave frequencies used in dispersive readout, few amplifiers have been able to reach this noise limit. Of these, the most common are a parametric amplifiers based on the non-linearity of the Josephson junction. The following is a description of the design and characterization of a superconducting Josephson parametric amplifier used for high visibility single qubit readout.

5.1 introduction

Low-power dispersive measurement of superconducting microwave resonators has become an important tool for applications ranging from the search for dark matter[46], quantum-limited measurements of mechanical resonators[47], and readout of superconducting qubits, where single-shot sensitivity is desirable[24, 48]. These measurements are typically performed using commercial cryogenic high-electron-mobility transistor (HEMT) amplifiers[43], which have several GHz of instantaneous bandwidth but add many photons of noise to the measurement signal. Recently a number of pre-amplifiers have been developed that achieve high gain with near-quantum-limited performance, including DC SQUID amplifiers[49], the superconducting low-inductance undulating galvanometer (SLUG) amplifier[50], TiN traveling wave parametric amplifiers[51], and Josephson junction-based parametric amplifiers[52, 53, 54, 55, 56, 57].

In this chapter we present a lumped-element Josephson parametric amplifier (LJPA), with a single-ended design and a high-bandwidth on-chip bias line, based on the approach in Ref [55]. The simple single-ended design, fabricated using a multi-layer fabrication process, eliminates the need for a hybrid coupler used in differential designs. The amplifier can be pumped either through its input port or through the bias line, using a number of different operating modes, making the device easy to adapt to a variety of applications. We find this design yields wide bandwidth, relatively high saturation power, and excellent noise performance.

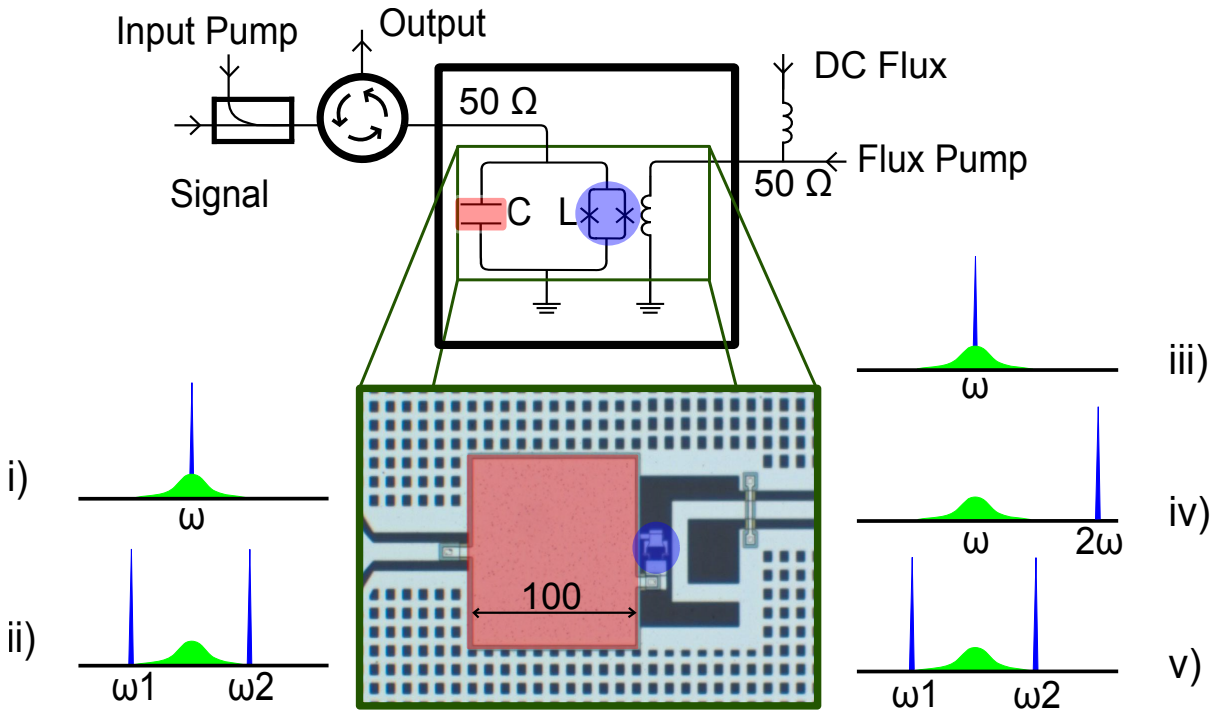

Figure 5.1: (Color online) Design of the paramp, where the signal is amplified through reflection off the non-linear resonant circuit. A circulator is used to separate incoming signals from amplified outgoing signals. Top details the layout of the Josephson LC resonant circuit with input port (left) and bias line (right). Bottom shows a micrograph of the device; false color indicates the parallel plate capacitor (red square) and the SQUID (blue circle), adjacent to the bias line. A DC current, applied via the bias line, changes the coupled flux and tunes the resonant frequency of the amplifier. The device can be pumped through either the input port via the directional coupler or through the flux-pump port. The pump (blue, dark) and response (green, light) graphs display the five possible pump modes coupled to their respective terminals: (i) ω-input, (ii) sideband-input, (iii) ω-flux, (iv) 2ω-flux, and (v) sideband-flux pumping.

5.2 circuit design

Junction based superconducting paramps, regardless of design, depend on frequency mixing via the nonlinear Josephson inductance. A sufficiently large pump tone can drive the circuit into a non-linear regime where energy couples from the pump to other tones within the device bandwidth. Parametric amplification occurs when the pump (ω_p), at the correct frequency and amplitude, transfers energy to a signal (ω_s) and idler (ω_i) tone. Depending on the design, a paramp can operate as either a three-wave mixing amplifier, where ($\omega_p = \omega_s + \omega_i$) with typically $\omega_p \approx 2\omega_s$, or four-wave mixing amplifier, where ($2\omega_p = \omega_s + \omega_i$) with typically $\omega_p \approx \omega_s$. In the degenerate output case ($\omega_s = \omega_i$) the signal and idler responses interfere to amplify only one quadrature, making phase sensitive operation possible with no added noise[45]. In the more general non-degenerate output case ($\omega_s \neq \omega_i$), the phase of the amplified signal is preserved but an additional half photon of quantum noise is mixed into the signal response from the detuned idler frequency. In either form of amplification the circuit remains superconducting and dissipates minimal energy internally. Thus the half photon (degenerate) or whole photon (non-degenerate) of noise from quantum fluctuations is the dominant source of system noise[45].

Existing paramps, using both three-[57] and four-wave mixing[53, 54, 55], operate in reflection mode: an incoming signal reflects off the amplifier, producing the outgoing amplified signal and idler tones. A microwave circulator separates the incoming from the outgoing signals, and provides a 50 Ω matched environment to eliminate standing waves at the input.

The pump mode also dictates the hardware used in the signal path of the amplifier. For

four-wave mixing ($\omega_p \approx \omega_s$), the large amplitude pump tone is combined with the signal using a directional coupler. In this case additional isolating hardware (typically a circulator) is needed to prevent the reflected pump tone from perturbing the signal source (e.g. a qubit) in the measurement line. This hardware can cause loss of signal and decreased system quantum efficiency. In principle this can be avoided by using two equally detuned pump tones[58] (sideband pumping in Fig. 5.1 (ii, v)), but both tones must be precisely balanced to optimize paramp performance, making tuning the amplifier bias more complicated. Three-wave mixing ($\omega_p \approx 2\omega_s$), where a single pump tone (Fig. 5.1 (iv)) is applied to the flux port, naturally avoids these constraints. Use of a single tone simplifies operation of the paramp, while pumping at twice the signal frequency eliminates the need for a directional coupler and naturally separates the pump and measurement signals.

In our single-ended device, as shown in the schematic and optical micrograph in Fig. 5.1, the paramp resonant circuit consists of a SQUID loop with flux tunable inductance shunted by a parallel plate capacitor, with a resonant frequency in the 4-8 GHz range. The resonator is directly connected to the signal and ground of the 50 Ω input. We tune the resonant frequency of the circuit by applying flux to the SQUID loop through an on-chip bias line, which is designed as a 50 Ω coplanar waveguide (CPW).

This design leverages existing multilayer fabrication techniques first developed for use in the Josephson phase qubit[59]. Low-loss amorphous silicon dielectric and low-impedance vias allow for 3-D routing of signal wires. We use these features to make a compact parallel plate capacitor and crossovers that eliminate CPW slot line modes. These devices have a capacitance

$C = 4.2$ pF, a stray inductance $L_s = 24$ pH, and an unbiased junction inductance $L_j = 68$ pH yielding a resonant frequency $(2\pi\sqrt{C(L_s + L_j)})^{-1} = 8.1$ GHz with a coupled quality factor (Q) of 10. The resonant frequency can be tuned from 4 to 8 GHz, shown in Fig. 5.2(a), with a DC flux-bias current applied through the bias line with a mutual inductance $M = 1.4$ pH. These devices are mass produced using wafer-scale fabrication, which yields hundreds of devices in parallel; we observe nominally identical performance between paramps from different chips.

This paramp, depending on which pump port is used and on the DC flux bias, can be operated as either a three-wave or four-wave mixing amplifier. It can be operated as a four-wave mixing amplifier by the application of either a single or two detuned pump tones at the input port, which we refer to as ω-input pumping (5.1 (i)) and sideband-input pumping (5.1 (ii)) respectively. In addition, the paramp can be operated by driving RF flux through the SQUID loop with the high-bandwidth flux bias line. This allows us to operate the device as either a four-wave amplifier with ω-flux pumping (5.1 (iii)) or a three-wave amplifier with 2ω-flux pumping (5.1 (iv)). It is also possible to operate the device with sideband-flux pumping (5.1 (v)), however more effort is required to tune the power of the pump tones on the flux-bias line. Figure 5.1 enumerates the five pump modes and indicates how each pump enters the circuit and the qualitative relationship between pump and amplified signal. The ability to use all five modes allows the amplifier to be tailored to the requirements of a specific experiment.

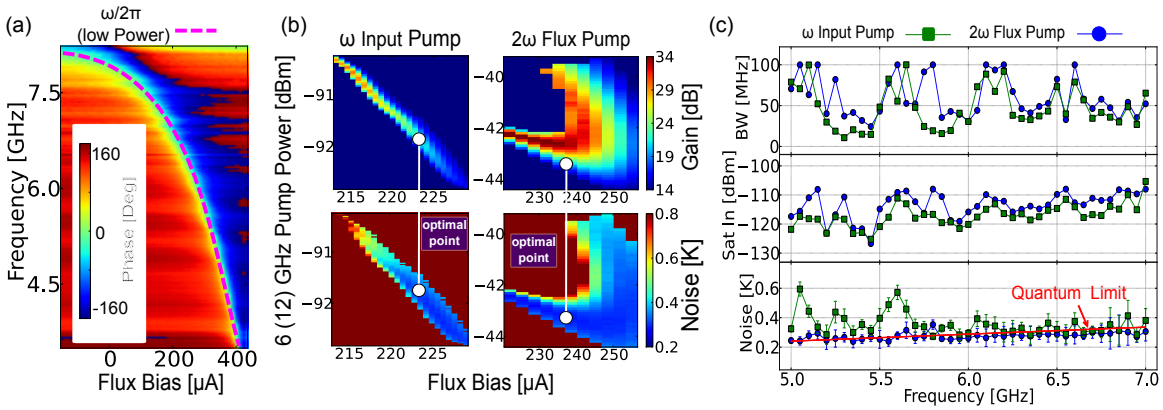

Figure 5.2: (Color online) (a) Reflected phase of a low-power microwave signal vs. signal frequency ($\omega/2\pi$) over the range of a half flux quantum of DC flux bias. The dashed line (zero phase) corresponds to the linear (low power) resonant frequency and demonstrates a tunable range from 4 to 8 GHz. (b) Power gain and system noise temperature (both referenced to input of directional coupler in Fig. 5.1) vs. DC flux bias and pump power, for both ω-input and 2ω-flux pump modes. With 2ω-flux pumping the device operates over a larger DC flux range and exhibits an additional branch where the amplifier operates with higher bandwidth at the cost of added noise. For both modes, the optimal point (white circle) was chosen to maximize bandwidth and saturation power while maintaining large enough gain (22 dB) to ensure quantum-limited noise performance. (c) Bandwidth, input saturation power and system noise temperature vs. frequency, for both pump modes. Data was taken after tuning up the amplifier to its optimal point (as shown in (b)) every 50 MHz from 5 to 7 GHz. We see structure in the frequency dependence of the bandwidth and saturation power, which provides evidence for impedance variations in the microwave environment. While the noise temperature of the amplifier in the phase-preserving mode, obtained using both pump modes, scales with the frequency-dependent quantum noise (red line) given by $\hbar\omega/k_B$, 2ω-flux pumping exhibits far less deviation from the quantum limit than ω-input pumping.

5.3 Comparison of 2ω and ω Pumping Modes

LJPA-style paramps, using ω-input pumping, have achieved gains greater than 25 dB and a gain-bandwidth product in the hundreds of MHz[55]. This gain-bandwidth product has to date proven to be an order of magnitude higher than paramps based on other resonant circuits[60, 61]. In our device we are able to replicate or exceed this performance with 2ω-flux pumping. With our device we can identify the effect of pump mode on performance, using the same device under identical conditions. Among the five possible modes, we thoroughly investigated 2ω-flux and ω-input pumping, because these modes are the easiest to use and yield the best performance.

We compared the ω-input and 2ω-flux pump modes by measuring amplifier performance vs. frequency, pump power and detuning, shown in Fig. 5.2 (b-c). For a given LJPA-style amplifier, performance depends on pump power and the detuning between the pump frequency and the low-power resonant frequency[62]. We changed the detuning by varying the DC flux bias of the amplifier while keeping the pump frequency constant. Figure 5.2(a) demonstrates the relationship between DC flux bias and the resonant frequency of the paramp, where we can tune from 4 to 8 GHz by applying between -300 and 400 μA of bias current, corresponding to a half-quantum of coupled flux. We characterized device performance using gain, bandwidth, saturation power, and system noise temperature. At each frequency, power, and detuning, we measured the transmission and noise power vs. frequency with the pump off, then we re-measured the same quantities, as well as transmission power vs. signal power, with the pump on. The gain was calculated as the increase in transmission power near the pump frequency,

the bandwidth as the full width at half maximum (FWHM) of the gain as a function of frequency, and the saturation power as the 1 dB compression point in gain vs. signal power. These quantities were only measured for gains larger than 14 dB, below which the paramp does not overcome the noise added by the HEMT. Here bandwidth refers to the full available bandwidth (for a given power and detuning) for constant wave (CW) signals. When measuring pulsed (wide-band) signals, only half of the FWHM bandwidth can be used without generating distortion from mixing between signal and idler tones. Lastly, we calculated the noise temperature of the amplifier in the phase-preserving mode using the method of signal-to-noise ratio improvement[55] over a standard HEMT amplifier, at frequencies slightly detuned from the amplifier center frequency. Using a Y-factor measurement[41] with a heated 50 Ω resistor installed on the mix plate of our dilution refrigerator (base temperature of 30 mK), the system noise temperature with only the HEMT was found to range from 1.8 to 2.6 K.

In general, we find that the same gain, bandwidth, and saturation can be achieved at multiple points in the pump power and detuning range, as shown explicitly for the gain in Fig. 5.2(b). We find 2ω-flux pumping displays lower noise over a larger range of applied flux than does ω-input pumping. Additionally, 2ω-flux pumping features a branch at larger pump powers, where the amplifier operates with wider bandwidth, albeit at the cost of added noise. When ω-input pumping, the optimal noise performance is at the lowest power and detuning (bottom-right most point in Fig. 5.2) for a given gain. For 2ω-flux pumping the entire lower branch exhibits quantum-limited performance. We ensured operation on the low noise branch, by tuning to gains larger than 30 dB, which do not exist on the other branch. Then for consistency, we

chose the lowest power and detuning on the low noise branch which achieves the desired gain.

Previous studies have shown that LJPA performance is strongly dependent on the impedance of the environment in which the paramp circuit is embedded[63]. As this impedance varies with frequency, we characterized this effect by measuring amplifier performance as a function of frequency. Using the data from Fig. 5.2(b) we implemented a software algorithm that tunes the amplifier to an optimal point in the parameter space, chosen as the smallest pump power and detuning that achieves 22 dB of gain with near quantum-limited noise. In this way we could ensure consistency between frequency measurements, eliminate experimenter bias, and automate the procedure. The gain, bandwidth, saturation power and noise were measured using this technique from 5 to 7 GHz, shown in Fig. 5.2 (c).

The data in Fig. 5.2(c) display oscillations in the paramp bandwidth ranging from 30 MHz to 100 MHz, with an average of about 50 MHz. The saturation power, which scales with pump power, also exhibits similar oscillations of several dB, with the average increasing steadily from -125 dBm at 5 GHz to -110 dBm at 7 GHz. The average saturation power scales with frequency because the pump power and frequency both scale with SQUID critical current. The oscillations are evidence of variations in the impedance of the microwave environment, because both bandwidth and pump power are strongly dependent on the coupling Q of the circuit[63]. We observe a larger than average input saturation power in this device resulting from lower than average Q as well as stray geometric inductance. Stray inductance weakens the nonlinear response of the circuit requiring more pump power to operate[64]. For both pump modes, the noise temperature of the amplifier scales with the frequency-dependent quantum noise, but

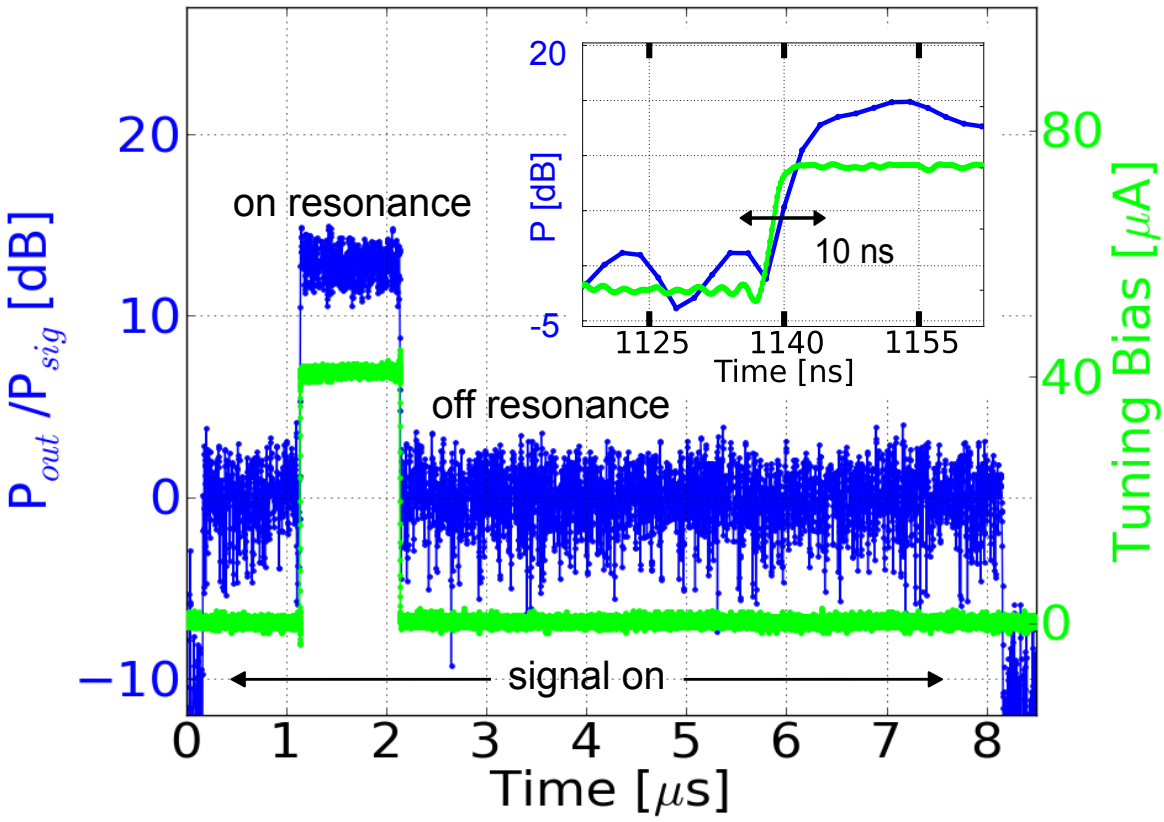

Figure 5.3: (Color online) Demonstration of dynamic frequency tuning of the amplifier. The output power normalized to the signal power (plotted in blue, dark) corresponds to the paramp gain, measured by mixing to DC and filtering. Starting at 0.2 μs a small amplitude 5.98 GHz tone is applied to the paramp for 8 μs. Using a 1 Giga-sample per second (Gsps) arbitrary waveform generator (AWG), the bias (plotted in green, light) is pulsed to 40 μA for 1 μs bringing the paramp on resonance and amplifying the 5.98 GHz tone. Insert shows the leading edge of power gain jump on a 60 ns time scale.

2ω-flux pumping deviates far less from the quantum limit than ω-input pumping, especially at lower frequencies.

5.4 Fast Resonance Tuning

In addition to allowing for multiple pump modes, the high bandwidth of the bias line can be used to rapidly tune the resonant frequency of the amplifier by varying the DC flux bias. This can enable one paramp to sequentially monitor multiple signals widely spaced in frequency, e.g. for multiplexed resonator or qubit readout[65, 66, 67, 40, 23]. The paramp should respond to a change in its resonant frequency over a time scale limited only by the paramp's quality factor. We verified this in 2ω-flux pump mode by tuning the paramp to yield a gain of 14 dB at 5.98 GHz for a $2\omega/2\pi = 12$ GHz pump tone, corresponding to a paramp center frequency of about 6 GHz. We then decreased the bias current by 40 μA, corresponding to a paramp frequency of about 6.4 GHz, and effectively reducing its gain at 6 GHz to unity. To test the paramp time-domain response we then applied a 1 μs duration, 40 μA pulse of current generated by a 1 Giga-sample per second (Gsps) arbitrary wave form generator (AWG), and monitored the time-dependent gain of a 5.98 GHz signal tone, as shown in Fig. 5.3.

The normalized paramp output power is shown in blue (dark) along with the AWG pulsed bias current in green (light). The time-domain signal was digitally mixed to DC and the idler tone and extra noise filtered. With the paramp off-resonant, the signal tone is only amplified by the HEMT and following amplifiers. During the current pulse, we see the gain increase suddenly by about 14 dB, in tandem with the DC current. The inset shows a fine time-scale

plot of the rising pulse edge. These data show that the resonant frequency can be changed by several hundred MHz in less than 10 ns.

5.5 Conclusion

In summary, we have demonstrated a single-ended LJPA with gain exceeding 22 dB, gain-bandwidth product greater than 500 MHz, a saturation power greater than -120 dBm, and near quantum limited performance over an operating frequency from 5 to 7 GHz. This versatile device also allows for the comparison of three- and four-wave mixing using ω-input and 2ω-flux pumping modes. While the performance of the amplifier is similar for both pump modes, 2ω-flux pumping offers better noise performance. Since 2ω-flux pumping also requires fewer components in the signal path, it is the preferred mode of operation. Lastly, we have demonstrated the inclusion of an on-chip bias line allows us to rapidly vary the resonant frequency of the amplifier. This could be used to read-out widely-spaced (in frequency) signals using successive measurements separated by only $\sim$10 ns.

While this device demonstrates low noise and high gain, it is still insufficient to conduct a BLGI experiment. While this device would allow us to conduct a high visibility measurement of a single qubit, it lacks the bandwidth and saturation power to measure more than one or two qubits at a given time. While we could attempt to use the time multiplexing feature documented above, we would again be constrained by T_1 decay during the overall measurement time. The challenge then is to achieve the same performance in noise and gain while drastically increasing bandwidth and saturation power. In the next chapter we will discuss one method of achieving

this goal through the use of impedance matching to the external environment.

Chapter 6

Impedance transformed parametric amplifier

To to successfully carry out a BLGI experiment, we require up to four simultaneous qubit state measurements all with high visibility. In the previous chapter we demonstrated a Josephson parametric amplifier with quantum limited noise performance and high enough gain to overcome the HEMT noise. The bandwidth and saturation power of this was not, however, capable of conducting the four simultaneous qubit state measurements. To increase these parameters in a superconducting JPA we require an unconventional approach to coupling, and a re-examining the the $50\,\omega$ environment. The following is a description of the resulting device known as the impedance-transformed parametric amplifier.

6.1 introduction

Parametric amplification is a result of frequency mixing via a nonlinear element coupled to an external environment. Amplifiers based on this principle have achieved near quantum limited performance[45], essential for high fidelity measurement of both optical [68] and microwave [46, 24] signals. In the microwave domain the Josephson parametric amplifier [52, 61, 54, 55, 56, 69] (JPA) has enabled new studies of quantum jumps [70] and measurement of quantum trajectories [71]. While well suited to single qubit dynamics, progress in scaling to larger quantum algorithms and fault-tolerant quantum computing [72, 27, 65] is limited by JPA bandwidth and dynamic range. JPA performance is constrained by weak coupling between the nonlinear resonator and the environment, chosen to simplify amplifier dynamics.

In this chapter, we experimentally demonstrate a JPA operated in a previously unreported regime of strong coupling to the environment. Physical insight into this coupling interaction follows naturally from the "pumpistor" model of a flux driven superconducting quantum interference device (SQUID), previously used to describe only degenerate (phase-sensitive) amplification [73]. By adapting the non-degenerate (phase-preserving) "pumpistor" theory [74] we create a model which accounts for dramatic improvements in both quantum limited bandwidth and dynamic range observed in this device. Additionally, by varying the environment we demonstrate significant control over amplifier dynamics and provide a further verification of the full "pumpistor" theory.

6.2 Impedance-transforming the JPA

The JPA relies on the Josephson inductance to create a nonlinear resonator which is typically weakly coupled to a $50\,\Omega$ embedding environment. When driven by a pump tone of sufficient power, energy is coupled from the pump (ω_p) into other signals within the resonator bandwidth. A signal applied near the resonant frequency (ω_o) results in an amplified signal (ω_s) and idler (ω_i) tone. In this work, the amplifier is operated as a non-degenerate (phase-preserving) three-wave mixing amplifier, where $\omega_p = \omega_s + \omega_i$ and $\omega_p \approx 2\omega_o$. The amplifier operates in a reflection mode where a microwave circulator separates the incoming signal from the outgoing amplified signal and idler tones, which are further amplified by a cryogenic following amplifier, typically a high-electron mobility transistor (HEMT) amplifier [43].

The impedance-transformed parametric amplifier (IMPA) shown in Fig. 6.1 builds on a typical lumped-element style JPA consisting of a SQUID loop with 100 pH of combined geometric and non-linear (Josephson) inductance L_j shunted by a 4 pF parallel plate capacitor C, for a characteristic impedance of $1/\omega_o C \approx 5\,\Omega$. Typically, this resonator is coupled to a $50\,\Omega$ transmission line, either directly or with a coupling capacitor. Practical measurements with the JPA are limited by narrow bandwidth (10-20 MHz typ.) and the low signal power (-120 dBm typ.) at which the amplifier saturates. These figures of merit are many orders of magnitude lower than the HEMT following amplifier. Bandwidth in the JPA scales as $1/Q$ and saturation power scales as I_c^2/Q [63] where I_c is the critical current of the SQUID and $Q = Z_o\omega_o C = Z_o/\omega_o L$ is the low power coupled Q of the JPA. For a fixed environment impedance Z_o and frequency ω_o, the coupled Q and critical current cannot be varied independently because $L_j \propto 1/I_c$, intro-

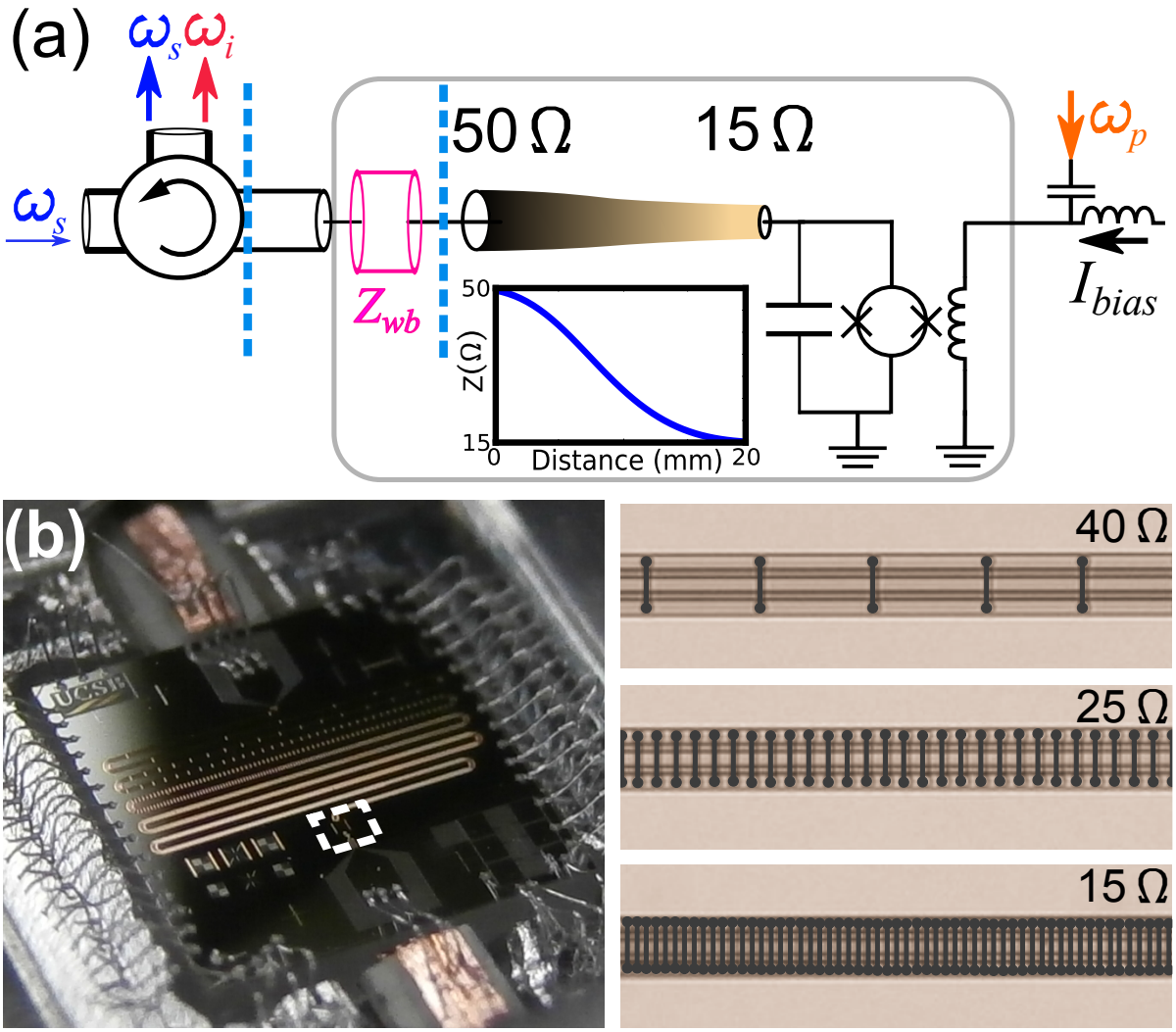

Figure 6.1: (Color Online) Schematic and photograph of the IMPA. **(a)** Circuit diagram of the IMPA (gray, light box) and accessory microwave hardware. The device consists of a nonlinear LC resonant circuit coupled to the 50 Ω environment by a tapered transmission line, smoothly varying from 50 Ω to 15 Ω, with profile shown in the inset. The bias port (right) injects current I_{bias} to change the resonant frequency ω_o of the circuit by varying the inductance of the SQUID loop. Dominant sources of reflections (dashed blue lines) in the chain are the circulator, used to separate incoming and amplified outgoing signals, and the wire-bond (pink, light) shown as Z_{wb}. **(b)** Photograph of device. The chip is a 3 mmX3 mm square. The gradient of the crossover density is visible as the 20 mm long CPW becomes increasingly bronze (light) in color. The LC resonant circuit is contained within the dashed box. On the right are photo-micrographs of different regions of the hybrid CPW/microstrip transmission line. As the density of 2 μm wide crossovers (false color in black) increases, the impedance of the transmission line drops.

ducing trade-offs between saturation power and bandwidth. This trade off can be circumvented using multiple SQUIDS in series [75], but this makes fabrication less reliable and complicates device operation.

In the IMPA, we instead transform the environmental impedance Z_o, increasing coupling, lowering Q and thus simultaneously increasing the bandwidth and saturation power. We use a tapered impedance transformer (Fig. 6.1) to lower the effective external impedance seen by the JPA from $50\,\Omega$ to about $15\,\Omega$. In this way, we can directly probe the effects of lowering the coupled Q while at the same time increasing both saturation power and available bandwidth.

A hybrid geometry was adopted for the taper, since the $15\,\Omega$ to $50\,\Omega$ impedance range is not intrinsically suited to either a purely co-planar waveguide (CPW) or microstrip transmission line. The tapered line consists of a fixed geometry CPW shunted with parallel plate capacitor cross-overs. The sections with a cross-over approximate a microstrip transmission line, with much lower local characteristic impedance. The small size of the crossovers ($2\,\mu$m) relative to the wavelength of a 6 GHz photon, allows us to vary the impedance smoothly with the density of crossovers, following a 20 mm long Klopfenstein taper [76, 41], a profile chosen to minimize the pass-band ripple of the network; see Fig. 6.1 [77].

6.3 IMPA performance

Using this new device we measure a significant increase in average saturation power, the power at which the gain compresses by 1 dB, with values as high as -103 dBm at 15 dB gain, as shown in Fig. 6.2. Decreasing the coupled Q has the added benefit of increasing bandwidth. We have

measured amplification bandwidths of nearly 700 MHz, shown in Fig. 6.2 for data centered about 6.7 GHz. Due to the multi-peaked gain features visible in the figure, we define the amplification bandwidth as the frequency range over which the device approaches the quantum noise limit. We calculate system noise using the method of signal to noise ratio improvement [55, 69] over the calibrated noise of the HEMT following amplifier. Further information on the HEMT noise measurement can be found in Appendix B.

The increase in average saturation power up to -108 dBm is consistent with theoretical expectations coming from both lower coupled Q (about 5 dB increase) and lower average gain (about 2-3 dB increase). This increase in input saturation power allows the amplifier to amplify both a higher power signal as well as quantum fluctuations from a larger bandwidth [77]. The factor of 10 improvement in the bandwidth however, cannot be explained by the reduced coupled Q. Moreover, the shape of the gain profile differs significantly from the typical Lorentzian described by most resonant JPA models [53, 63, 75] and thus requires a detailed understanding of how the JPA interacts with variations in the microwave environment.

6.4 The "pumpistor" model

For a JPA coupled to a perfect 50 Ω environment, the incident signal tone at ω_s reflects off the LC resonator, where pump photons are converted to amplified signal ω_s and idler ω_i tones. In the case of an imperfect match to the environment, the outgoing amplified signal and idler tones are back-reflected towards the JPA, creating standing waves and affecting device gain through constructive or destructive interference. These standing waves are properly thought

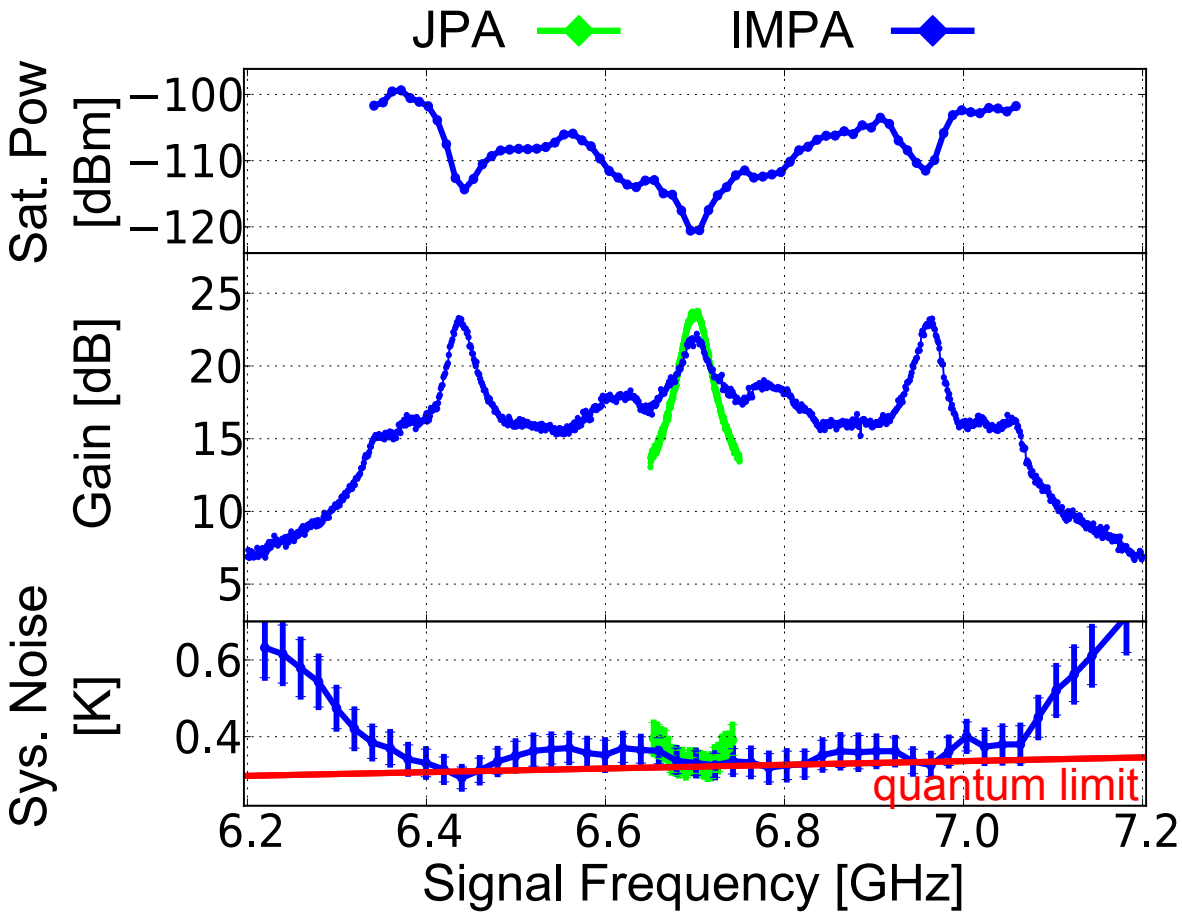

Figure 6.2: (Color Online) Input saturation power, gain, and noise performance of the IMPA. Here we show amplifier performance centered at 6.7 GHz for a single pump tone at 13.4 GHz. The IMPA (blue, dark) provides an average input saturation power (defined as 1 dB compression point) of -108 dBm with regions as high as -103 dBm. The device gives greater than 15 dB of gain and near quantum-limited performance over a bandwidth of nearly 700 MHz. This is compared to a typical JPA with a $Q = 10$ (green, light) for a similar gain, which only provides quantum-limited performance over a 60 MHz band. We define the quantum limit as one photon $\hbar\omega$ of total system noise at the input of the amplifier. Here deviations from the quantum noise limit correspond to gains that are unable to completely overwhelm the noise added by the HEMT following amplifier. Error bars on the noise correspond to potential systemic calibration errors on HEMT system noise.

of as variations in the frequency dependent admittance $Y_{\text{ext}}(\omega_s)$ (inverse impedance) of the environment seen by the JPA. The predominant sources of reflections in the microwave chain are due to the wire-bond and microwave circulator interfaces, shown as dashed lines in Fig. 6.1

(a). Typically, experiments are designed to minimize the distance between the JPA and these reflection planes, spacing out these standing waves in frequency. As a result, the effects of these standing waves are not so apparent in devices with $Q¿10$ as variations in the impedance are small over the response bandwidth of the JPA.

The full "pumpistor" theory [74], while previously validated for only the degenerate frequency (phase-sensitive) case [73], is well suited to a detailed analysis of the effect of these standing waves on non-degenerate gain in a JPA. Here, the non-linearity of a flux-pumped SQUID loop is treated as a power dependent modification of the SQUID inductance. For a signal at frequency ω_s the admittance of the loop becomes $Y(\omega_s) = 1/i\omega_s L_0 + 1/i\omega_s(L_1 + L_2)$, where the three elements of the inductance are

$$L_0 = L_j/\cos(\pi\Phi_Q/\Phi_0) \tag{6.1}$$

$$L_1 = -\frac{4L_j\cos(\pi\Phi_Q/\Phi_0)}{\pi^2\sin^2(\pi\Phi_Q/\Phi_0)}\left(\frac{\Phi_0}{\Phi_{ac}}\right)^2 \tag{6.2}$$

$$L_2 = i\frac{4\omega_i L_j^2 Y^\star_{\text{ext}}(\omega_i)}{\pi^2\sin^2(\pi\Phi_Q/\Phi_0)}\left(\frac{\Phi_0}{\Phi_{ac}}\right)^2. \tag{6.3}$$

Here the idler frequency $\omega_i = \omega_p - \omega_s$, $L_j = \Phi_0/(2\pi I_c)$ is the unbiased SQUID inductance, Φ_Q is the DC flux bias, and Φ_{ac} is the amplitude of the flux pump. The dependence of L_2 on the external admittance at the idler frequency $Y^\star_{\text{ext}}(\omega_i)$ comes about because the pump also drives oscillations at the idler frequency, and the magnitude of these oscillations depends on the output admittance. As the pump power increases from zero, $L_1 + L_2$ emerges as an element in parallel with the initial SQUID inductance L_0. The term L_1 modifies the inductance of the circuit, lowering the operating frequency as pump power increases. The term L_2 represents an

imaginary inductance that gives rise to a negative real impedance given by Re$[i\omega_s L_2]$.

As the JPA is a reflection amplifier, we can use our "pumpistor" model to calculate the reflection coefficient and thus the gain G using the admittance (impedance) mismatch between the external evironment Y_{ext} and the paramp admittance Y_{JPA}.

$$G(\omega_s) = \frac{Y_{\text{ext}}(\omega_s) - Y_{\text{JPA}}(\omega_s)}{Y_{\text{ext}}(\omega_s) + Y_{\text{JPA}}(\omega_s)}. \tag{6.4}$$

Using Eqs. (6.1)-(6.3) we derive a simplified approximation of the JPA admittance which includes the SQUID loop and shunt capacitance C

$$Y_{\text{JPA}}(\omega_s) = \frac{-2i(\omega_o - \omega_s)}{\omega_o \omega_s L_c} - \frac{\pi^2 \sin^2(\pi\Phi_Q/\Phi_0)(\Phi_{ac}/\Phi_0)^2}{4\alpha\omega_s\omega_i L_{\text{j}}^2 Y_{\text{ext}}^{\star}(\omega_i)}, \tag{6.5}$$

where $1/L_c = 1/L_0 + 1/L_1$ is the combined parallel inductance of the SQUID, $\omega_o = 1/\sqrt{CL_c} \approx \omega_p/2$, and $\alpha = 1 + Q^2 \approx 10$ is due to a series to parallel circuit conversion [77]. Equations (6.4) and (6.5) describe how a knowledge of the frequency dependent admittance of the environment at both the signal and idler frequencies is required to model amplifier behavior.

We show in Fig. 6.3(a) solutions to Eq. (6.4) and (6.5) with a 10% sinusoidal variation in Y_{ext}. With increasing power, the denominator in Eqs. (6.4) is brought closer to zero, resulting in increased gain. The Q = 20 case shows that the effect of Y_{ext} on the overall gain is dominated by the narrowed response of the JPA. For comparison, in the Q = 3 case (gold, light), the response of the JPA is broad enough to sample variations in the external environment. Moreover, the profile of the gain reflects the shape of Y_{ext} at that frequency. This results in the variations in bandwidth seen in the left versus right simulation. We note that the measured gain profiles show a high degree of symmetry for ω_s about $\omega_p/2$, regardless of the detailed behavior of Y_{ext}.

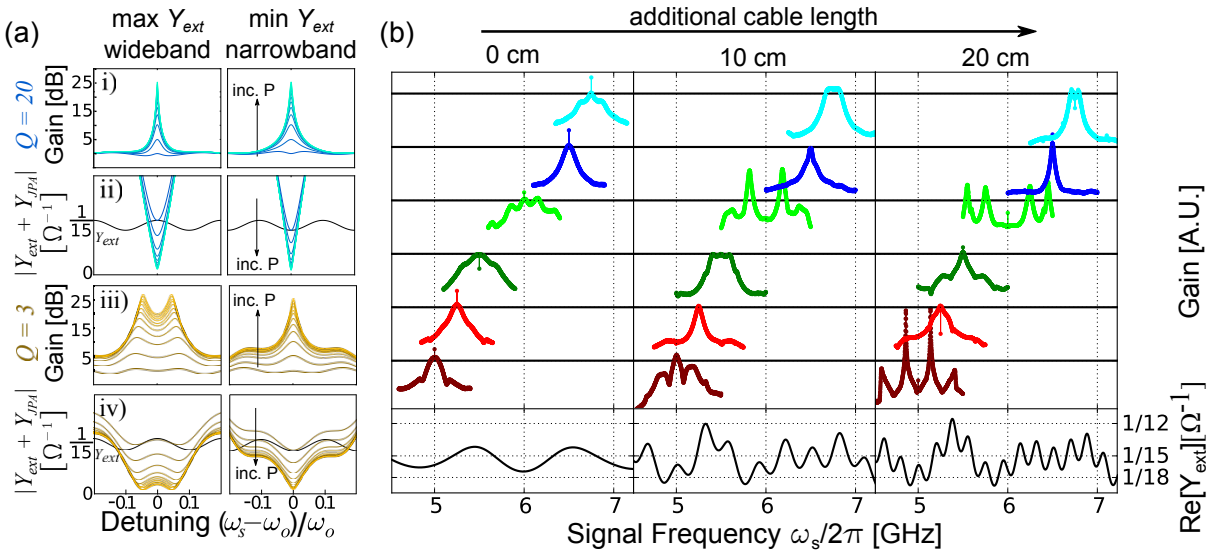

Figure 6.3: (Color Online) Effect of variation in external admittance on amplifier performance. **(a)** Simulated gain profiles (i,iii) showing the effect of external impedance on gain for both weak ($Q = 20$) and strong ($Q = 3$) coupling. Higher pump power is denoted by lighter colored traces and indicated by the arrow. The denominator of Eq. 6.4 (ii,iv) is plotted, with the gain shown in (i,iii). As pump power increases the denominator is displaced from Y_{ext} towards zero by an increasingly negative Y_{JPA}. In a weakly coupled device (i,ii) the gain profile is not affected by the shape of the external admittance. In the case of strong coupling (iii, iv) the response of the JPA is broader and the gain profile is greatly influenced by the external admittance. If $\omega_p/2 = \omega_o$ is centered at a maxima in external admittance the gain is broadened (left), if ω_o is centered on a minima it is narrowed (right). **(b)** Experimental variation of the standing waves in the external environment. Gain profiles of approximately 20 dB, and offset by 20 dB (denoted by bold horizontal lines) are shown as the amplifier frequency ω_o is tuned from 5 to 7 GHz. Standing waves are introduced by lengthening the cable between the IMPA and the circulator; the longer the cable, the more closely spaced in frequency are the standing waves. Amplitude variations in Y_{ext} come from a superposition of standing waves in the cable and on-chip taper. The gain profiles become increasingly featured as the variations in Y_{ext} (calculated using SPICE) increase with cable length.

This is to be expected, as the gain samples Y_{ext} at both the signal and idler frequencies, which are symmetrically placed about $\omega_p/2$. A broader sampling of frequency dependent gain profiles calculated using Eqs. (6.4) and (6.5) are shown in Ref. [77] with a similar degree of symmetry.

6.5 testing the model

To test the dependence of amplifier performance on environment admittance, we changed the pattern of standing waves on the output line by changing the length of cable separating the device from the circulator. We measured the gains as a function of ω_s for different resonant frequencies ω_o from 5 to 7 GHz with direct connection to the circulator, a 10 cm and 20 cm cable. The results of this experiment are shown in Fig. 6.3(b). In each case, a series of gain profiles with $\sim$ 20 dB peak gain are shown, spaced vertically. We also plot the frequency-dependent output impedance taken from simulations using the corresponding length of cable. This frequency-dependent admittance can be estimated using lumped circuit models to approximate the dominant contributions from the circulator and wirebond connections.

When the amplifier is connected directly to the circulator, the admittance variation is minimized and the IMPA more consistently approaches the expected Lorentzian gain profiles. When connected using the 10 cm cable a drastic change is exhibited in many of the peaks showing both broadening at some frequencies and narrowing at others. When the 20 cm cable is used the output impedance varies more rapidly and the device performance becomes increasingly erratic while often exhibiting multiple distinct resonant peaks. The experimental data shows good qualitative agreement to that predicted by the "pumpistor" reflection model.

While the gain profile is strongly dependent on frequency, when the amplifier is properly tuned for quantum-limited noise performance the complexity of the gain profile is insensitive to DC flux and pump power. Moreover we see very little chip to chip and run to run variation, with most of the performance variations arising from changes to the experimental setup. This

effect is evident in the nominally Lorentzian gain profiles observed with direct connection to the circulator. This reliability is further demonstrated by the IMPA's use in broadband, high-power, multi-qubit readout in existing experiments [28, 27]. These experiments both make use of the operation point shown in Fig. 6.2 with a roughly 15 cm copper cable connecting the IMPA to the circulator.

6.6 conclusion

In conclusion, we have demonstrated validation of the "pumpistor" theory and application of a new model for understanding parametric amplifier behavior. In the strongly coupled limit this model predicts unexpectedly large bandwidths, which have been observed in the IMPA with near quantum-limited noise performance. Using this model, further improvements should be possible by shaping the external embedding impedance, possibly with alternate matching networks [78]. Additionally, this strong coupling could enhance performance in alternate JPA designs, such as multi-SQUID LJPAs[75]. This large bandwidth, along with a significant increase in saturation power, gives us all the tools to conduct a full BLGI experiment. There is however an additional amplifier design which might provide even better performance than the IMPA at the cost of increased complexity. This traveling wave parametric amplifier will be discussed in the next chapter.

Chapter 7

Josephson junction based traveling wave parametric amplifier

The traveling wave parametric amplifier (TWPA) promises huge increases in bandwidth and saturation power at the cost of increased fab complexity. While the IMPA should be sufficient to conduct the BLGI, the much larger bandwidth and saturation power of the TWPA would provide additional freedom in choosing our readout parameters. What follows is a description of the design and operation of a Josephson junction based TWPA.

7.1 Introduction

The Josephson parametric amplifier [52, 61, 54, 55, 56, 69, 79] (JPA) is a critical tool for high fidelity state measurement in superconducting qubits [48, 71, 15] as it allows parametric amplification with near quantum-limited noise [45]. Despite its success, the JPA has typically been

used only for single frequency measurements due to lower bandwidth and saturation power. A promising approach to scaling superconducting qubit experiments is frequency multiplexing [65, 67, 80], which requires additional bandwidth and dynamic range for each measurement tone. Simultaneous amplification of up to five multiplexed tones has been achieved with a JPA [28, 27, 81] but was only possible with the Impedance-transformed parametric amplifier [82] (IMPA). This highly engineered JPA provides much larger bandwidth and saturation power but pushes the resonant design to its low Q limit.

To extend this frequency multiplexed approach for future experiments, we have adopted the distributed design of the traveling wave parametric amplifier (TWPA) [83]. Fiber-optic TWPAs have already demonstrated high gain, dynamic range, and bandwidth while reaching the quantum-limit of added noise [84, 68]. In this letter we present a microwave frequency TWPA with 4 GHz of bandwidth and an order of magnitude more saturation power than the best JPA. This device is compatible with scaling to much larger qubit systems through multiplexed measurement, and may find applications outside quantum information such as astrophysics detectors [65, 46]

7.2 TWPA as a non-linear transmission line

At microwave frequencies the TWPA can be thought of as a transmission line where the propagation velocity is controlled by varying the individual circuit parameters of inductance or capacitance per unit length [86, 87]. This is typically achieved by constructing a signal line with a current dependent (nonlinear) inductance. Like the JPA, a large enough pump tone will

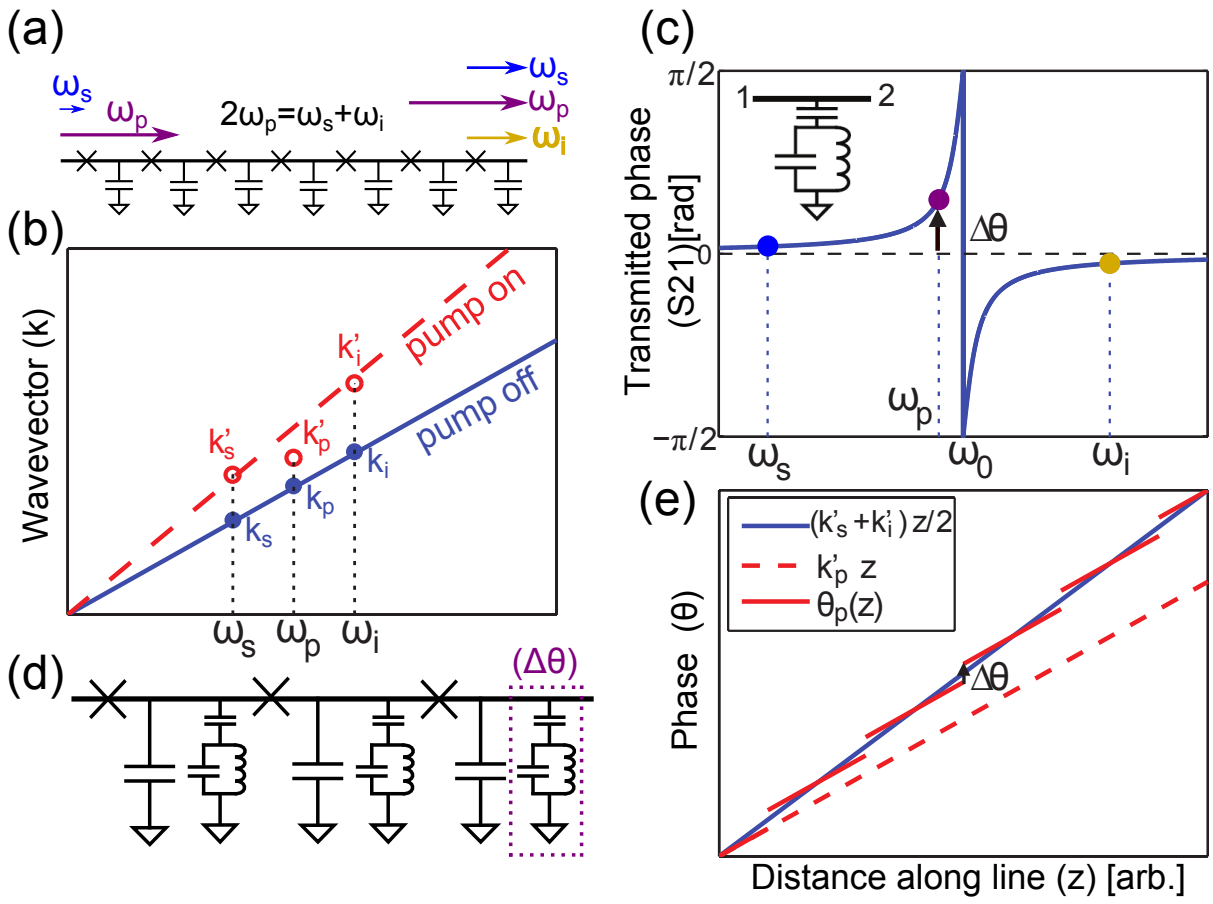

Figure 7.1: (Color Online) (a)Circuit diagram of the Josephson juction TWPA. (b) The dispersion relationship in a conventional Josephson junction traveling wave parametric amplifier (TWPA). For weak signals (linear regime), the dispersion is linear $\Delta k = k_s + k_i - 2k_p = 0$ where $k = \omega/v_p$. When a strong pump tone is applied, the traveling waves are slowed down due to an increase in the junction inductance and a decrease in the phase velocity. The pump tone is slowed down less than the signal and idler tones due to the difference between the self-phase modulation and cross-phase modulation [85] effects which causes a mismatch $\Delta k' > 0$. (c) Phase shift due to a shunt resonator to ground. The resonator produces a frequency dependent phase shift for just the pump tone. (d) Resonantly phase matched TWPA in which resonator phase shifters are inserted between nonlinear transmission line sections. (e) The phase of the pump tone is adjusted at discrete locations and piece-wise matched to the signal and idler tones which enhances the gain, as can be seen from a tight fit between the stepped solid red line and the straight blue line $\Delta k = 0$. Without these resonator phase shifters, the phase mismatch would grow (as can be seen from the departure of the dashed red line from the solid blue line) and the gain would be limited to the quadratic case of Eqn. (7.3).

modulate this inductance, coupling the pump (ω_p) to a signal (ω_s) and idler (ω_i) tone via frequency mixing such that $\omega_s + \omega_i = 2\omega_p$. Unlike the JPA however, the TWPA has no resonant structure so gain, bandwidth, and dynamic range are determined by the coupled mode equations of a nonlinear transmission line [88]. In addition to allowing more bandwidth and saturation power, the TWPA is directional so that amplification only occurs for signals propagating in the same direction as the pump.

The concept of a nonlinear superconducting transmission line has been demonstrated in NbTiN TWPA [51] where the kinetic inductance of the superconductor provides nonlinearity in a standard co-planar waveguide (CPW). These amplifiers have achieved gains greater than 20 dB over bandwidths greater than 8 GHz, and with saturation power many orders of magnitude larger than a standard JPA. To achieve this high dynamic range, a large pump tone ($\sim 100\,\mu W$) is required, which poses many engineering challenges for qubit readout. Attenuation in the line leads to heating which increases the base temperature of the experiment. Likely due to this local heating, the NbTiN amplifier has yet to reach the quantum limit of added noise. In addition, the qubits must be aggressively isolated from the large pump tone which requires additional hardware.

The ideal amplifier for qubit readout would provide gain and bandwidth similar to the NbTiN TWPA but with a higher non-linearity, requiring less pump power and achieving quantum-limited noise. A promising approach is to build a TWPA based on the non-linear inductance of the Josephson junction (JJ) [89, 90, 91, 92, 93]. This junction TWPA (JTWPA) circuit, shown in Fig. 7.1(a), combines JJs with shunt capacitors to construct a 50 Ω lumped element transmis-

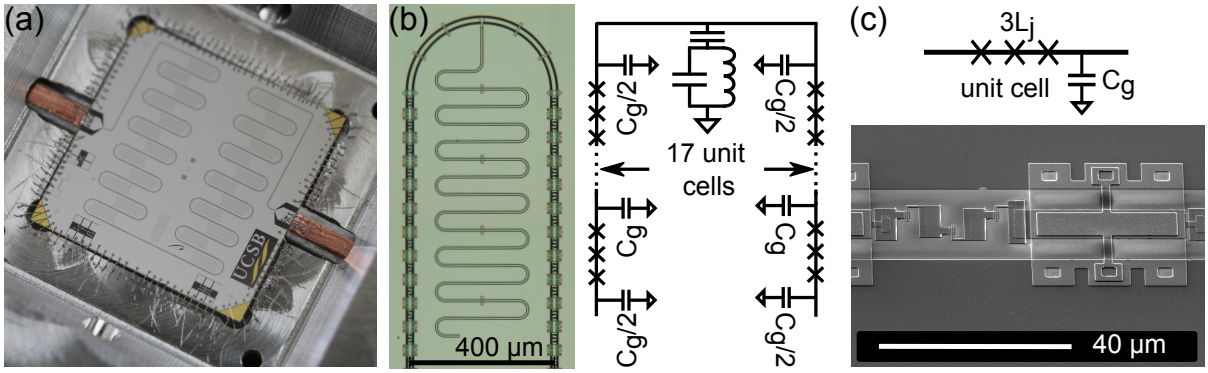

Figure 7.2: (Color Online) (a) Photograph of the TWPA showing the full packaged device with an aluminum box and copper circuit-board feed lines. The chip is square with 6 mm sides. (b) Optical micrograph and circuit diagram that show the discrete phase matching through the periodic insertion of $\lambda/4$ CPW resonators, spaced at an electrical length equivalent to $\lambda/2$ of the pump tone. (c) Scanning electron micrograph of the non-linear unit cell consisting of three double angle evaporation Josephson junctions(left) and a shunt parallel plate capacitor(right), with amorphous silicon dielectric.

sion line. The capacitors and JJs are small relative to the wavelength of a microwave signal, giving an effective capacitance and non-linear inductance per unit length. The JTWPA obeys the same physics as the NbTiN TWPA, but needs $\sim 10^5$ times less pump power.

7.3 phase matching and the coupled mode equations

TWPA gain is described by solving the coupled mode equations including mixing terms between the pump(k_p), signal(k_s), and idler(k_i) wave vectors [85]. Power gain is given by

$$G_s = \cosh^2(gz) + \left(\frac{\kappa}{2g}\right)^2 \sinh^2(gz) \tag{7.1}$$

and

$$g = \sqrt{\frac{k_s k_i}{k_p^2}(\gamma k_p)^2 - (\kappa/2)^2}. \tag{7.2}$$

Here z is the length along the transmission line, $\gamma = I_p^2/16I_c^2$ describes the ratio of drive current to junction critical current (nonlinearity), and $\kappa = 2\gamma k_p + k_s + k_i - 2k_p$ is the effective dispersion. The pre-factor $k_s k_i/k_p^2$ describes the bandwidth of the amplifier and maximizes gain when $k_s = k_i = k_p$. For small signal powers where $\gamma \approx 0$, κ would be described by the difference in wave vectors $\Delta k = k_s + k_i - 2k_p$. The term $2\gamma k_p$ describes the self phase modulation of the pump, shown in Fig. 7.1 (b), which increases with pump power. In a linear superconducting transmission line there is no dispersion, so $\Delta k \approx 0$ making $\kappa \approx 2\gamma k_p$. The maximum gain then occurs when $g \approx 0$ and is given by

$$G_s = 1 + (\gamma k_p z)^2 = 1 + \phi_{nl}^2, \tag{7.3}$$

where $\phi_{nl} = \gamma k_p z$ is the nonlinear phase shift of the pump, such that gain depends quadratically on length. If proper phase matching can be achieved, $\kappa = 0$, $g = \gamma k_p$, and the maximum gain, given by

$$G_s = \cosh^2(\gamma k_p z) \approx \frac{\exp(2\phi_{nl})}{4}, \tag{7.4}$$

is exponentially dependent on length. The phase matched design thus provides a much larger gain-bandwidth than a non phase matched TWPA for a given number of junctions and is a more efficient amplifier design.

To produce $\kappa = 0$ we can counter the power-dependent phase shift of the pump with an engineered frequency-tunable phase shift. In the NbTiN TWPAs this was accomplished by a periodic impedance variation which created a narrow band gap and phase shift in the transmission [94]. However, this approach provides only a small correction to the phase shift per unit length, which is incompatible with the high nonlinear phase shifts of the JTWPA.

Alternatively, a resonator capacitavly coupled to the transmission line, shown in Fig. 7.1(c), produces an arbitrarily large frequency dependent phase shift which counters the non-linear phase shift. By including such a resonator after every nonlinear section in the transmission line, shown in Fig. 7.1(d), the pump frequency could be tuned to cancel the phase mismatch; thus making $\kappa \approx 0$. This approach has been shown to significantly increase both gain and bandwidth for a given number of junctions [95, 93].

While continuous phase correction is the most obvious approach, a resonator following each junction can introduce additional complications. The large number of resonators would require a compact lumped-element design with parallel plate capacitors. The frequency of these resonators would be harder to control and the extra dielectric will introduce more loss. It should be possible however, to use fewer total resonators if we increase the phase shift from each individual resonator. With fewer total resonators we can use larger CPW designs with lower loss and greater frequency control. The concept of discrete phase correction is shown in Fig. 7.1 (e).

7.4 TWPA design

Our device, shown in Fig. 7.2(a), consists of a single 66 mm CPW with both non-linear (lumped element JJ array) and linear (superconducting Al) sections. The 1326 JJs are standard Al-Al_2O_3-Al junctions created using double angle evaporation [96]. The junction critical current was designed to be $5\ \mu$A with an effective inductance of 65 pH per junction that, combined with geometric inductance, gives 3.5 μH/m. Parallel plate capacitors made with low loss amorphous

silicon (a-Si:H) dielectric [97] provide 1.6 nF/m in the non-linear sections of the chip, setting the impedance while also shorting together the ground planes. This connectivity is important feature such a long transmission line could support lossy slot line modes. The periodic structure shown in Fig. 7.2(b) consists of a series of JJs followed by a linear section where the resonator is used to fix the pump phase before entering the next non-linear section. To improve the impedance matching of the non-linear sections, the first and last shunt capacitor is half the capacitance of the others. We chose a nonlinear unit cell of 3 junctions per capacitor, shown in Fig. 7.2(c), to lower the transmission line cutoff frequency while maintaining a high junction critical current. This was done to prevent leakage of pump power into higher harmonics, which may reduce gain, and to prevent the onset of a shock wave. [98].

In the case of 1000 junctions, continuous phase matching can be approximated with the phase shift of just 10 ideal phase shifters [85]. This result however does not consider the effect of the resonant amplitude dip on the pump, which can lead to large reflected pump energy. Using more resonators will lessen this effect, but increase design complexity. However, if the $\lambda/4$ resonators are spaced by $(2n)\lambda/4$, where λ is the wavelength corresponding to the resonator frequency, the periodic placement provides a large stop band at 3ω to prevent pump leakage. To take advantage of this enhancement on a chip with 1326 junctions, we chose 26 resonators with 17 non-linear unit cells between each resonator. The resonance coming from the periodic placement combines with the resonators to create a sharp amplitude dip at 6.1 GHz with optimal phase shift at about 5.8 GHz, where almost no pump energy is reflected.

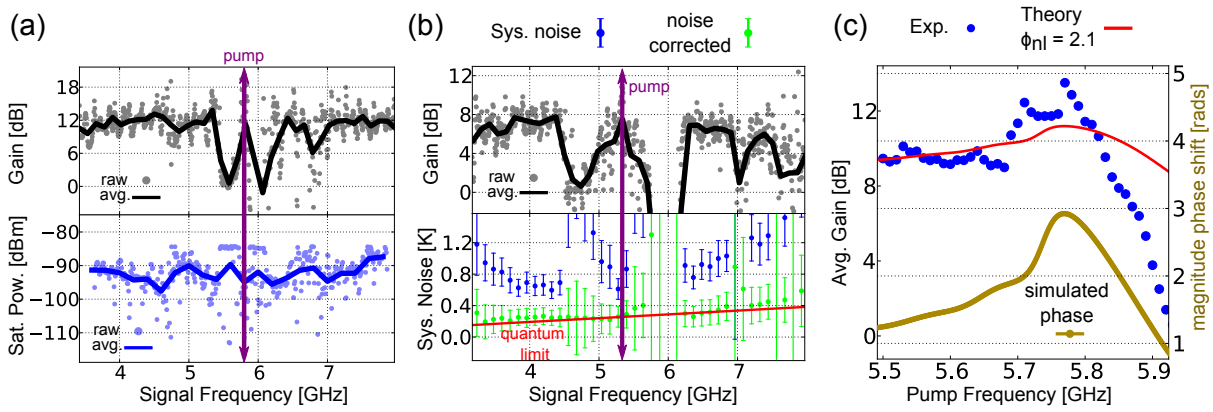

Figure 7.3: (Color Online)(a) Saturation power and gain vs frequency for optimal pump gain with two TWPAs chained together; the pump tone is 5.83 GHz. Raw data is plotted in lighter points with a darker averaged line overlaying the data. Average saturation power is -92 dBm and average gain is 12-14 dB. The dips on either side of the pump come from the resonator reflecting either the signal or the idler tone close to the pump. (b) Gain and system noise vs frequency for a different experiment optimized for low noise at a pump tone of 5.32 GHz. In this experiment the maximum gain achieved was 8 dB while the lowest noise was 600 mK corresponding to an input noise of 2 photons. The raw system noise is plotted in blue(dark), while system noise with the contribution from the HEMT subtracted is plotted in green(light). (c) Average gain and simulated phase shift vs frequency measured for a pair of devices which achieved 12-14 dB max gain. The blue (dark) data points are the averaged gain values, the yellow (light) curve is the simulated resonator phase shift, and the red (solid dark) line is a theoretical gain curve computed using the simulated phase shift. The change from linear to exponential is consistent with $\phi_{nl} \approx 2.1$ with a peak at 5.8 GHz.

7.5 TWPA performance

In the past JTWPAs have had difficulty reaching the quantum limit of added noise due to loss in the transmission line [91]. To characterize the loss and transmission line performance in our device, we measured the amplitude of S_{21} and S_{11} through both the TWPA and a copper cable of equivalent length. We used *in-situ* microwave switches to alternate between the cable and the TWPA in the same experimental setup [85]. We find that the difference in S_{21} is less than 0.5 dB over the entire 4-8 GHz measurement band. When measuring S_{11} of the TWPA we see an average reflected amplitude -10 dB relative to the cable S_{21}. This is consistent with the majority of the signal difference between the TWPA and the cable coming from reflections due to imperfect impedance matching [85].

The device presented in Fig. 7.2(a) provides a good test of amplifier performance, but is limited to 6-8 dB gain. To increase the gain and verify the phase matching will hold in a longer device we chain two of these chips together in series. The performance of this amplifier chain is shown in Fig. 7.3 and details the 1 dB compression point (saturation power), gain, and noise temperature. Each chip was in a separate box and the boxes were connected via SMA connectors. The gain was measured relative to the low power transmission amplitude.

As can be seen in Fig 7.3(a), the chained device displays an average gain of 12-14 dB over almost the entire 4-8 GHz frequency range. Interestingly the gain dips quite significantly on either side of the pump. This is due to the reflection of either the signal or idler tone when measuring close to the pump frequency. Variations in the gain on the order of 2-3 dB most likely come from imperfect impedance matching between sections and at the bond pads. These

variations in gain also affect the saturation power, here defined as the 1 dB compression point. The broad band input saturation power shown in Fig. 7.3(a) varies from -95 dBm to -85 dBm with an average of -92 dBm. This represents a significant improvement in both bandwidth and saturation power over the best resonant JPA [82]. The reverse gain measured was 0 dB as expected from the directionality of the coupled mode equations [85].

To measure noise temperature we used the method of signal to noise ratio improvement [55, 85] over a traditional high electron mobility (HEMT) semiconductor amplifier [43]. In this experiment the HEMT noise temperature was measured to be 2.5 ± 0.5 K over the measurement band. Unfortunately while measuring the TWPA noise temperature, the gain, shown in Fig. 7.3 (b), reached only 8 dB. In this case we, find that the noise does approach the quantum limit over the entire range but reaches a low of only 600 mK. This noise temperature corresponds to about 2 photons of input noise and is consistent with residual HEMT noise at low gain. If we subtract the expected HEMT contribution to the system noise we find the noise added by the TWPA is very close to quantum limit.

To verify the frequency dependence of the gain we measured maximum average gain vs frequency for the device shown in Fig. 7.3(a). The frequency dependence of the gain is shown in Fig. 7.3(c) along with a simulated phase shift coming from the resonators. The average gain increases by ~ 5 dB when it nears the resonator phase shift. This is consistent with a nonlinear phase shift $\phi_{nl} \approx 2.1$ with a predicted device gain plotted with a solid red line along with the data.

7.6 conclusion

We have experimentally demonstrated a Josephson junction traveling wave parametric amplifier with minimal resonator phase matching. This amplifier displays a significant increase in both bandwidth and saturation power while maintaining near quantum-limited noise performance. By using discrete resonators to correct the pump phase we can access the exponential gain dependence with a minimal increase in fab complexity. In this regime we should be able to increase the gain by simply increasing the length of the device. In addition it may be possible to improve the transmission amplitude even further through fine tuning of the impedance in each section.

While the initial performance is encouraging, the performance is not quite at the level necessary for a violation of the BLGI. White there is a large bandwidth, the variation of gain in frequency makes amplifier performance highly variable. Additionally the highest gain achieved is not quite sufficient to overcome the noise of the HEMT. In principle these issues can be solved by fixing fabrication issued leading to better uniformity in junction critical current. In the mean time the BLGI can still go forward using an IMPA as the quantum limited pref-amplifier.

Chapter 8

Preserved entanglement and violation of the BLGI

With the development of high bandwidth and high saturation power Josephson parametric amplifiers, we can conduct high visibility state readout simultaneously on four qubits. If we combine this with the high fidelity control demonstrated in superconducting qubits, we can in principle violate the BLGI. This first requires us to map the BLGI algorithm onto a superconducting qubit system. What follows is a description of the theoretical concepts and their physical implementation on a superconducting qubit chip.

8.1 Recap: weak measurement and the BLGI

Quantum computing promises greater processing power through the clever application of superposition and entanglement. Despite the importance of this uniquely quantum behavior, it oc-

curs elusively behind the non-unitary effects of measurement collapse. Weak measurements[12, 13, 14] have provided new insight into this collapse process by demonstrating the ability to extract average state information without fully collapsing the system. These gentler measurements have allowed single-configuration violations of the Leggett-Garg inequality [17, 18, 19, 20, 21, 22, 23, 6] and, more recently, the detailed tracking of single qubit trajectories [15, 16]. It is an outstanding challenge however, to achieve the same level of measurement control with an entangled state. Here we demonstrate for the first time a continuous and controlled exchange of extracted state information and two-qubit entanglement collapse, achieved using variable strength ancilla qubit measurements of a maximally entangled Bell state. We quantify this effect by correlating weak measurement results with subsequent projective readout to collect all the statistics of a Bell inequality experiment [2, 3, 4, 8] in a single quantum circuit. Additionally, we demonstrate the ability to measure the Bell state with minimal entanglement collapse, by violating this hybrid Bell-Leggett-Garg inequality [25] at the weakest measurement strengths. This experiment indicates that it is possible to learn about the dynamics of large entangled systems without significantly affecting their evolution, and when combined with remote entanglement [99], may lead to a loophole-free test of quantum mechanics.

The challenge of successfully implementing weak measurements is twofold: the first is to evaluate the amount of information extracted on average by the measurement; the second is to evaluate the measurement back-action on the system. For a single qubit state, the Leggett-Garg inequality [5] (LGI) provides an elegant way to do both with a single experiment. The LGI was originally designed to verify the "quantumness" of macroscopic objects through the effects of

projective measurement, which allows larger correlations between successive measurements (e.g., at times $t_1 < t_2 < t_3$) than are possible classically. More recent generalizations of the LGI prepare a known state at time t_1 and replace the intermediate measurement at time t_2 with a weak measurement [17, 18, 19, 20, 21, 22, 23, 6]. This minimizes the quantum state disturbance while still extracting sufficient information on average. Ideally this allows all the statistics necessary for a violation of the inequality to be measured with a *single* experimental configuration. Violating the inequality in this way guarantees that the state information has been extracted without significant back-action on the system [20].

Evaluating the effect of weak measurements on an entangled state is more difficult because the degree of entanglement is in generally challenging to quantify. The most robust method for quantifying entanglement remains a Bell test [2], which was first proposed by Bell and later refined by Clauser, Horne, Shimony, and Holt into an inequality (CHSH). The CHSH term sums the correlation measurements of two spatially separated qubits in four different measurement bases and bounds the maximum total value of classical correlations to be $|\text{CHSH}|_{\text{class}} \leq 2$.

8.2 BLGI with superconducting qubits

In superconducting qubits, we use qubit state rotations to map the desired measurement basis onto the ground ($|0\rangle$) and excited ($|1\rangle$) states of the system. For measurement rotations a (qubit 1) and b (qubit 2), the correlation amplitude between two measurements is given by

$$E(a,b) = P(00) - P(10) - P(01) + P(11), \tag{8.1}$$

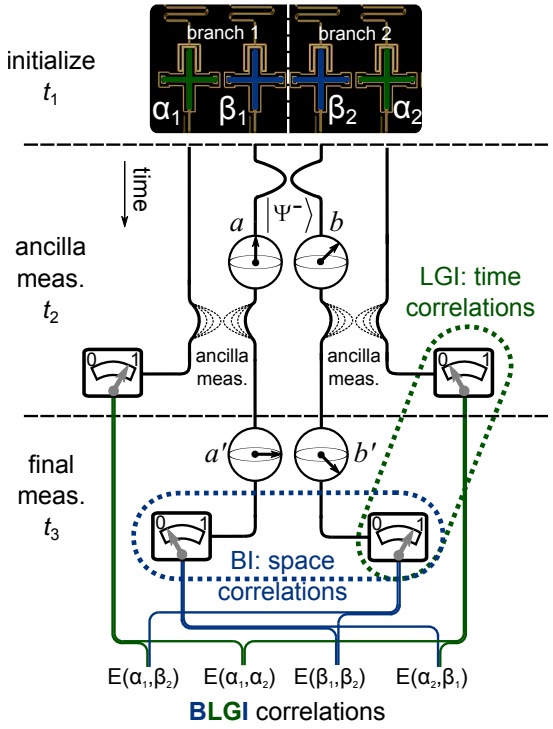

Figure 8.1: Schematic of the hybrid Bell-Leggett-Garg inequality and optical micrograph of the superconducting quantum device. The algorithm consists of two LGI weak measurement branches, bridged by the entanglement of the central Bell qubits. The Bell pair ($\beta_{1,2}$) is initially prepared in the anti-symmetric singlet Bell state $|\Psi^-\rangle$. Next, each Bell qubit is rotated to its first measurement basis (a or b) and entangled with its ancilla qubit ($\alpha_{1,2}$). Finally, the Bell qubits are rotated and projectively read out in bases corresponding to angles a' and b'. By correlating the final projective read out and the weak ancilla measurements we calculate all four terms of a CHSH correlator simultaneously.

where the term $P(00)$ is the probability both qubits are in the ground state. A traditional CHSH experiment combines the four correlator terms

$$\text{CHSH} = E(a,b) + E(a',b) + E(a,b') - E(a',b'). \tag{8.2}$$

Entangled quantum states can violate the classical bound, with a fully entangled Bell state ideally saturating the quantum upper bound of $|\text{CHSH}|_{\text{quant}} \leq 2\sqrt{2}$ at the specific rotation angles $a = 0$, $b = \pi/4$, $a' = \pi/2$, and $b' = 3\pi/4$.

To understand the effect of weak measurement on an entangled state we combine the spatial correlations of a Bell inequality with the temporal correlations of an LGI to construct a Bell-Leggett-Garg inequality (BLGI). The algorithm, as described by Dressel and Korotkov [25] and shown in Fig. 8.1, consists of a CHSH-style experiment in which each Bell qubit is measured twice in succession as for a simultaneous LGI [100, 20, 23]. After preparing the Bell qubits in the anti-symmetric singlet state

$$|\Psi^-\rangle = \frac{1}{\sqrt{2}}(|01\rangle - |10\rangle), \tag{8.3}$$

each Bell qubit ($\beta_{1,2}$) is rotated to its first measurement angle ($a = 0$, $b = \pi/4$) and then entangled with its ancilla qubit ($\alpha_{1,2}$) to implement a tunable-strength measurement. Next, each Bell qubit is rotated to its final measurement angle ($a' = \pi/2$, $b' = 3\pi/4$), and all four qubits are read out. With this procedure the data for each measurement angle is encoded on a distinct qubit ($a \to \alpha_1$, $b \to \alpha_2$, $a' \to \beta_1$, and $b' \to \beta_2$). The BLGI correlator then takes the form similar to Eq. (8.2)

$$\langle C \rangle = -E(\alpha_1,\alpha_2) - E(\alpha_1,\beta_2) + E(\beta_1,\alpha_2) - E(\beta_1,\beta_2). \tag{8.4}$$

where each term is calculated as in Eq. (8.1).

By encoding the measurement result for each rotation angle on an independent qubit, we can measure all the correlations of a CHSH style inequality in one simultaneous experimental configuration. The BLGI statistics can then be used to quantify the state information extracted by the weak measurement, as well as the entanglement collapse of the central Bell qubits. If the ancilla measurement is fully projective then $|E(\alpha_1, \alpha_2)| = 1/\sqrt{2}$, but the entanglement is destroyed so all other correlations vanish. As the ancilla measurement strength is decreased, we should extract the same qubit information on average while only partially collapsing the Bell state. If this is true, then as we turn down the measurement strength the value of $|E(\alpha_1, \alpha_2)| = 1/\sqrt{2}$ should remain unchanged while the magnitudes of the remaining three correlators increase. For sufficiently weak measurements, the magnitudes of all four correlators approach the unperturbed Bell state values of $1/\sqrt{2}$, and $\langle C \rangle$ approaches $2\sqrt{2}$. Thus a violation of the BLGI done in this way demonstrates the ability to measure both qubits in a Bell state with complete control over the magnitude of entanglement collapse. Additionally, as we can measure all four correlators at once, we can evaluate each weak ancilla measurement independently.

We performed this experiment on a linear chain of Xmon transmon qubits, shown at the top of Fig. 8.1, with ground to excited state transition frequencies in the 4-6 GHz range [81]. Each qubit is individually addressed with a microwave control line which can be used for single qubit X or Y gates as well as a DC line for implementing Z-gates and frequency control. These control lines are used in conjunction to execute high fidelity two-qubit gates [27] for entanglement and ancilla measurement. The state of each qubit is measured independently us-

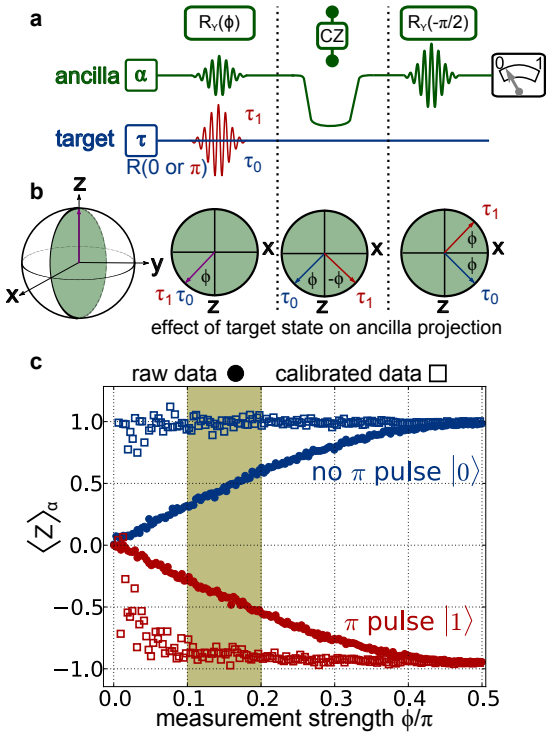

Figure 8.2: Weak measurement protocol. **a**, Full pulse sequence of the ancilla measurement algorithm used in the BLGI experiment. The measurement consists of a variable amplitude Y rotation by an angle ϕ which controls the strength of the measurement. This is followed by a CZ gate that entangles the ancilla qubit with the target qubit. Finally the ancilla is rotated by an angle $-\pi/2$, bringing it into the desired measurement basis. Two cases are compared, that of the target qubit in the ground (blue) or excited (red, π rotation) state. **b**, Bloch sphere representation of the ancilla qubit during the weak measurement protocol when the target qubit is in either the ground (blue) or excited (red) state. The Z averages of the ancilla and target qubit are correlated such that $\langle Z \rangle_\alpha = \sin(\phi)\langle Z \rangle_\tau$, where a full projective measurement corresponds to $\phi = \pi/2$ and no measurement corresponds to $\phi = 0$. **c**, Ancilla measurement of prepared target state before and after calibrating for measurement strength. We calibrate both curves by the scaling factor required to normalize the average 0 state curve. This is almost equivalent to dividing by $\sin(\phi)$ but bounds the calibrated mean by ± 1. In the calibrated case, the measured mean remains unchanged while the measured variance increases as ϕ decreases. The gold shaded region denotes angles at which weak measurement data can violate the BLGI while still being reliably calibrated

ing the dispersive shift of a dedicated readout resonator. Resonators are frequency multiplexed [67] and readout with a broadband parametric amplifier [82], which allows for fast high fidelity measurement. Further details of this device can be found in Refs. [81, 37].

8.3 Weak ancilla measurement

The ancilla measurement protocol used in this experiment and shown in Fig. 8.2, is a modified version of the protocol demonstrated in an LGI violation from Groen *et al.* [23]. Initially, an ancilla qubit is Y-rotated by an angle $0 \leq \phi \leq \pi/2$ from its ground state to set the measurement strength. A control phase gate is then performed, causing a Z rotation of $\pi/2$ in the ancilla qubit depending on the target qubit's state. Finally a $-Y$ rotation of $\pi/2$ is performed on the ancilla qubit to rotate into the correct measurement basis. The visibility of this measurement is then proportional to the distance of the ancilla state vector from the equator of the Bloch sphere, as shown in Fig. 8.2 (b). When $\phi = \pi/2$ this operation becomes a control-NOT gate and implements a projective measurement. As $\phi \to 0$ the ancilla states become degenerate and no information is extracted.

As the final position of the ancilla state is dependent on the measurement strength, the ancilla readout is imperfectly correlated with the target qubit. That is, the visibility of an ancilla Z average, $\langle Z \rangle_\alpha \simeq \sin(\phi)\langle Z \rangle_\tau$, is compressed from the target Z average by a factor of approximately $\sin(\phi)$. To reconstruct the target Z average from the ancilla Z average, we should thus rescale the signal by $1/\sin(\phi)$. For more robust calibration, we used data-based rescaling to set the measured ground state ($|0\rangle$) average to 1, which ensures that the calibrated

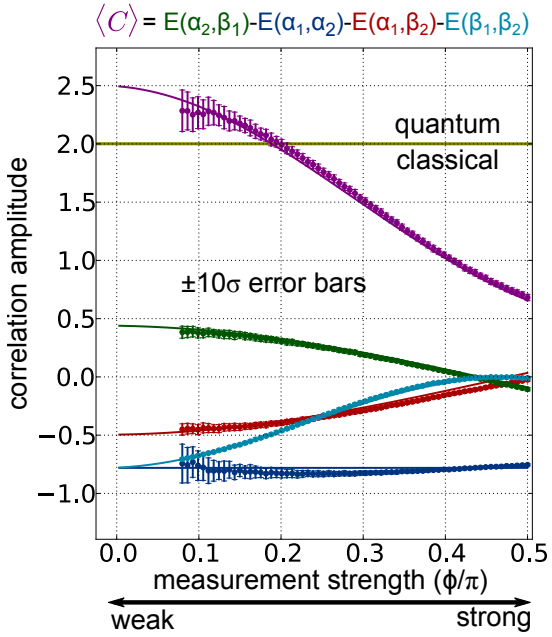

Figure 8.3: Graph showing both experimental data (points) and theoretical predictions (lines) for the correlator $\langle C \rangle$ and its four terms vs. measurement strength ϕ. The horizontal gold line denotes the classical bound on $\langle C \rangle$. The data set was taken by averaging together 200 traces in which each point was measured 3000 times for a total of 600,000 iterations per point. The error bars represent 10 standard deviations of the mean to demonstrate the scaling the ancilla measurement noise vs. ϕ. The magnitude of the correlations between each pair of qubits reveals the extent to which entanglement has been broken for each measurement strength.

ancilla average is properly bounded by ± 1, as shown in Fig. 8.2(c). Further details of this calibration can be found in appendix D.

8.4 Results

After this and other extensive system calibrations, we can begin our investigation in earnest. To quantify the entanglement collapse, we measure each two-qubit correlator in $\langle C \rangle$ vs. ancilla measurement strength ϕ. The data are plotted in Fig. 8.3 alongside theory curves generated by a quantum model that includes realistic environmental dephasing and readout fidelity [25]. Error

bars for the data represent ± 10 standard deviations of the mean to demonstrate the increase in noise with decreasing measurement strength. For projective angles $\phi \approx \pi/2$, the ancilla measurement results ($E(\alpha_1, \alpha_2)$) reflect the correlation expected from a fully collapsed Bell pair. As measurement strength is decreased, this ancilla correlation remains nearly constant while additional inter-qubit correlations ($E(\alpha_1, \beta_2)$, $E(\beta_1, \alpha_2)$, $E(\beta_1, \beta_2)$) emerge. For sufficiently weak measurements, $\langle C \rangle$ exceeds the classical bound of 2 and saturates towards the CHSH value of 2.5, which is expected from simulations for a fully entangled Bell state in realistic experimental conditions [37].

The measured BLGI correlations follow the theoretical model [37] very closely for all measurement strengths. This behavior, observed for the first time in experiment, reveals the continuous and controlled exchange between the collapse of an entangled Bell state and the information gained from tunable-strength measurements. Each ancilla qubit, when calibrated, retains the same correlations for all measurement strengths, whereas each Bell qubit has its correlations damped through partial projection by its ancilla qubit [25]. The effect of partial projection can be seen in the difference in functional behavior between the Bell-ancilla ($E(\alpha_1, \beta_2)$, $E(\beta_1, \alpha_2)$) and the Bell-Bell ($E(\beta_1, \beta_2)$) correlator terms. In the Bell-ancilla terms, the correlations are suppressed solely due to the randomization of the Bell qubit, but return as soon as measurement strength is decreased. In the Bell-Bell term, this effect is compounded as both qubits are being damped by partial ancilla projection, so the correlations return more slowly. This gives $E(\beta_1, \beta_2)$ its distinct shape compared to the other correlators. The BLGI terms can be seen in greater detail in appendix D.

8.5 conclusion

While other methods exist to characterize entanglement, the correlation measurements of a CHSH experiment remain one of the more robust tests of quantum behavior due to the considerations given to experimental loopholes. Fortunately, the unique construction of the BLGI allows us to avoid some of the more pervasive loopholes appearing in traditional Bell or LG inequalities. The simultaneous measurement of all four CHSH terms in a single circuit allows us to avoid any configuration-dependent bias, such as the disjoint sampling loophole [10]. The near unit detection efficiency in superconducting systems [101, 37] similarly bypasses the fair sampling loophole [9], which has hindered the investigation of related hybrid inequalities in optical systems [22, 26]. Additionally, since the data from each ancilla qubit is only correlated with the data from the Bell and ancilla qubits on the remote LGI branch, we can substantially relax the usual LGI noninvasive measurement assumption to the standard locality assumption needed for a Bell inequality instead.

This locality assumption, fundamental to any Bell inequality, presumes no classical interactions between remote qubits occur during the correlation measurements. The close proximity of adjacent superconducting qubits on a chip implies that such an interaction cannot be ruled out here. Thus, behavior that appears to be quantum could, at least in principle, be the result of a fast classical interaction between hidden variables in the system. While we cannot yet completely rule out these local interactions, there are several promising approaches to closing this loophole as well. The assumptions of the BLGI requires only spatial separation of the central Bell qubits. The speed and fidelity of operations in a superconducting qubit system makes

modest spatial separation sufficient, and we can sacrifice some Bell state preparation fidelity to achieve it. Techniques such as remote entanglement through measurement [99], may soon provide the spatial separation necessary to conduct a loophole-free BLGI experiment.

In the course of this work we have demonstrated the continuous and controlled collapse of an entangled state based on the strength of tunable ancilla measurements. This behavior was quantified using the simultaneous correlation measurements which make up the Bell-Leggett-Garg inequality. The violation of this inequality at the weakest measurement strengths demonstrates the viability of using weak ancilla measurements to conduct many sequential measurements of entangled states. This provides a window into the evolution of entangled states, a critical component in scaling to larger quantum systems. With the inclusion of new remote entanglement algorithms the BLGI may also lead to a loophole-free test of quantum mechanics. Lastly this demonstrates that as we scale to larger multi-qubit systems, with the fidelity and control achieved here, we gain greater access to the rich physics at the heart of quantum mechanics.

Appendix A

Supplementary information for chapter 5: four wave mixing in an LJPA

A.1 Nonlinear behavior under a strong current drive

Much like the superconducting qubit, the Lumped element Josephson parametric amplifier (LJPA) consists of a resonant circuit with a nonlinear inductance. Just like the qubit this nonlinear inductance comes from the addition of a Josephson junction or SQUID loop. As discussed in the main text, the SQUID loop is desirable because it allows us to tune the resonant frequency of the circuit through the application of an external flux. This allows us to tune the frequency of the amplifier with a dc Flux, and carry out parametric amplification with an RF flux drive. The behavior of the circuit under an RF flux drive can be modeled using the "pumpistor" theory which will be discussed in Appendix B.

Due to the difficulty of engineering a clean electrical ground, historically the DC resonant frequency is varied by flux bias from a coiled wire [52, 53, 54, 55, 56, 57]. The high inductance of such a line acts as a good noise filter, but prevents driving at the higher frequency necessary to achieve flux driven parametric amplification. There is an alternative method of operation known as four-wave mixing, in which a large pump tone at the input of the device acts as a current drive at a frequency similar to that of the signal being amplified. While the devices used in this experiment are flux driven, an understanding of four-wave mixing and strong input driving can be helpful in tuning up the device or diagnosing problems.

In standard four-wave mixing operation, the external flux is a constant and only used to vary the resonant frequency of the device. The inductance of the device is then described by the Joesphson inductance constant

$$L_{J0} = \frac{\phi_0}{2\pi I_0} \tag{A.1}$$

Where I_0 is simply the SQUID critical current given by $2I_c|\cos((\pi\phi_{ext})/\phi_0)|$. To understand the behavior of circuit under a strong RF current drive $I_{rf}\cos(\omega_d)$, we can write down the equations of motion for the phase δ across the SQUID loop, given the current relation $I = I_0\sin(\delta)$

$$\begin{aligned}
\frac{d^2\delta}{dt^2} + 2\Gamma\frac{d\delta}{dt} + \omega_r^2\sin(\delta) &= Fcos(\omega_d t) && \text{(A.2)}\\
\omega_r &= \sqrt{\frac{2\pi I_0}{\phi_0 C}} = \frac{1}{\sqrt{L_{J0}C}} && \text{(A.3)}\\
\Gamma &= \frac{1}{2RC} && \text{(A.4)}\\
F &= \frac{2\pi I_{rf}}{\Phi_0 C}. && \text{(A.5)}
\end{aligned}$$

Here ω_d is the frequency of the current drive and R is the source impedance (in this case $50\,\Omega$) of the line. The $\sin\delta$ term on the left side of the equation is what gives the system its nonlinear behavior. Fortunately we can construct a very good model of the circuit behavior by replacing the sin function with its Taylor series expansion, and retaining only the first nonlinear term. This makes the equation of motion

$$\frac{d^2\delta}{dt^2} + 2\Gamma\frac{d\delta}{dt} + \omega_r^2(\delta - \frac{\delta^3}{6}) = F\cos(\omega_d t) \tag{A.6}$$

A constant current drive such as this will produce a response in δ at the same frequency and described by the equation

$$\delta = \delta_0\cos(\omega_d t - \phi), \tag{A.7}$$

where A is the amplitude of the oscillations and phi is the relative phase to the drive signal. If we plug in this solution and use the following 2 identities

$$\cos^3(x) = \frac{3}{4}\cos(x) + \frac{1}{4}\cos(3x) \tag{A.8}$$

$$F\cos(\omega_d t) = F\cos(\phi)\cos(\omega_d t - \phi) - F\sin(\phi)\sin(\omega_d t - \phi) \tag{A.9}$$

we can regroup the terms in the equation based on their particular sinusoidal time dependence. This leaves us with

$$(\delta_0\omega_r^2 - \delta_0\omega_d^2 - \frac{\omega_r^2\delta_0^3}{8} - F\cos\phi)\cos(\omega_d t) \tag{A.10}$$

$$+(-2\delta_0\Gamma\omega_d + F\sin(\phi))\sin(\omega_d t) \tag{A.11}$$

$$-\frac{\omega_r^2\delta_0^3}{24}\cos(3\omega_d t) = 0 \tag{A.12}$$

We can neglect the $\cos(3\omega_d t)$ term as small and oscillating too rapidly around 0 to affect our response at ω_d. The remaining two equations must then satisfy

$$F\cos(\phi) = \delta_0(\omega_r^2 - \omega_d^2 - \frac{\omega_r^2\delta_0^2}{8}) \quad (A.13)$$

$$F\sin(\phi) = 2\delta_0\Gamma\omega_d, \quad (A.14)$$

such that

$$F^2 = \delta_0^2\left(\left(\omega_r^2 - \omega_d^2 - \frac{\omega_r^2\delta_0^2}{8}\right)^2 + (2\Gamma\omega_d)^2\right) \quad (A.15)$$

$$\tan(\phi) = \frac{2\Gamma\omega_d}{\left(\omega_r^2 - \omega_d^2 - \frac{\omega_r^2\delta_0^2}{8}\right)}. \quad (A.16)$$

These equations model the behavior of the nonlinear Duffing oscillator [102]. We can then plot the Duffing oscillator equation to understand the response of the circuit. Figure A.1 displays various amplitude response functions vs frequency.

A.2 From nonlinear oscillator to parametric amplification

To explain why four-wave parametric amplification occurs with a strong current drive, we must investigate the response of the system when a small signal is applied along with the pump. We can postulate that with a very small additional drive signal the drive and response go to

$$\delta \rightarrow \quad \delta + \epsilon \quad (A.17)$$

$$F\cos(\omega_d) \rightarrow \quad F\cos(\omega_d) + f\cos(\omega_s) \quad (A.18)$$

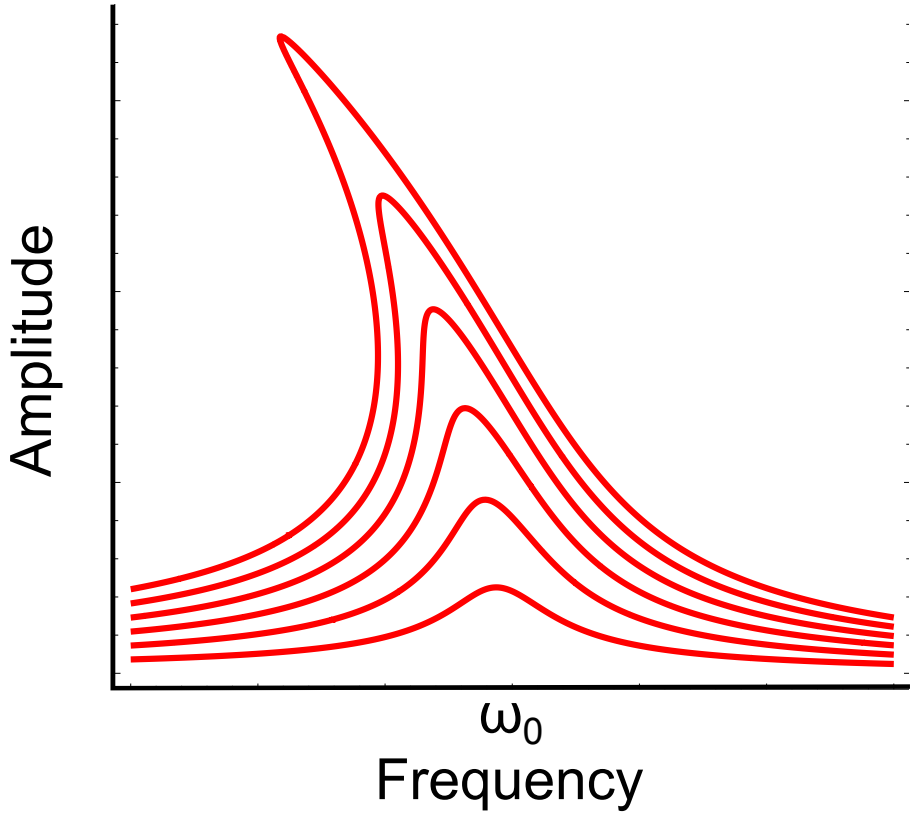

Figure A.1: Nonlinear response curve of a standard duffing oscillator. The plot includes amplitude vs frequency curves for multiple drive amplitudes: $I_{rf} = 0.01{*}I_0$, $0.02{*}I_0$, $0.04{*}I_0$, $0.08 * I_0$, $0.12 * I_0$, and $0.16 * I_0$. At low drive amplitudes the response is mostly linear in frequency and resembles the resonance peak of a standard LC oscillator. As the drive power is increased the resonance peak begins shift lower and deform at the peak. Eventually these curves become locally multi-valued with a high amplitude, meta-stable, and low amplitude state.

where ω_s is the signal frequency and ϵ is the phase response at ω_s. The equation of motion then becomes

$$\frac{d^2(\delta+\epsilon)}{dt^2} + 2\Gamma\frac{d(\delta+\epsilon)}{dt} + \omega_r^2\left((\delta+\epsilon) - \frac{(\delta+\epsilon)^3}{6}\right) = F\cos(\omega_d t) + f\cos(\omega_s) \qquad \text{(A.19)}$$

This equation breaks down into three components: the strong drive tone and the response in delta, the signal tone and the response at epsilon, and mixed terms between delta and epsilon.

To understand this circuit as a parametric amplifier we need only to calculate the response ϵ. Thus we can get rid of all the terms involving only δ and all the terms with more than one power of epsilon, since epsilon is very small compared to the pump. This reduces the equation of motion for ϵ to

$$\frac{d^2\epsilon}{dt^2} + 2\Gamma\frac{d\epsilon}{dt} + \omega_r^2\epsilon(1 - \frac{\delta^2}{2}) \quad = \quad f\cos(\omega_s). \tag{A.20}$$

If we then replace δ with the duffing oscillator solution $\delta = \delta_0\cos(\omega_d - \phi)$, we can rewrite this equation as

$$\frac{d^2\epsilon}{dt^2} + 2\Gamma\frac{d\epsilon}{dt} + \omega_r^2\epsilon(1 - \frac{\delta_0^2\cos^2(\omega_d - \phi)}{2}) \quad = \quad f\cos(\omega_s) \tag{A.21}$$

$$\frac{d^2\epsilon}{dt^2} + 2\Gamma\frac{d\epsilon}{dt} + \omega_r^2\epsilon(1 - \frac{\delta_0^2}{4} - \frac{\delta_0^2}{4}\cos(2\omega_d - 2\phi)) \quad = \quad f\cos(\omega_s). \tag{A.22}$$

From this equation we can see how the pump tone affects the circuit behavior, by re-writing the resonance frequency as

$$\omega_r \rightarrow \omega_r\sqrt{1 - \frac{\delta_0^2}{4} - \frac{\delta_0^2}{4}\cos(2\omega_d - 2\phi)}. \tag{A.23}$$

As the pump fluctuation amplitude δ_0 increases, it increases the variation in the resonant frequency for the signal tone while also decreasing the average resonant frequency. This pump modulation provides the parametric amplification in four-wave mixing amplification.

Understanding the nonlinear phase response of the LJPA, shown in Fig. A.2, is a valuable tool when first tuning up the amplifier. The phase response is particularly useful because it provides a clear indicator of the DC resonant frequency, and the frequency at which parametric amplification is likely to occur. Of particular importance is that the frequency decreases as the

amplitude of the pump increases. Thus the circuit must be first tuned to a frequency larger than the frequency of amplification, as it will be pulled lower by an increasing pump tone. By fine tuning the pump tone amplitude and dc resonant frequency, amplification with the desired gain can be achieved. Considering the excellent agreement with theoretical models, this response can also be used to gauge the relative drive power at the resonant circuit. Understanding the response and the likely drive amplitude needed for parametric amplification can be a valuable tool when diagnosing problems with the experimental system.

To understand the effect of frequency modulations at $2\omega_d$, we can Fourier transform this equation to find the frequency dependent response $\epsilon(\omega)$. Carrying out this transformation, assuming $\epsilon(-\omega) = \epsilon^*(\omega)$, and throwing out higher frequency terms $2\omega_d + \omega$ we get

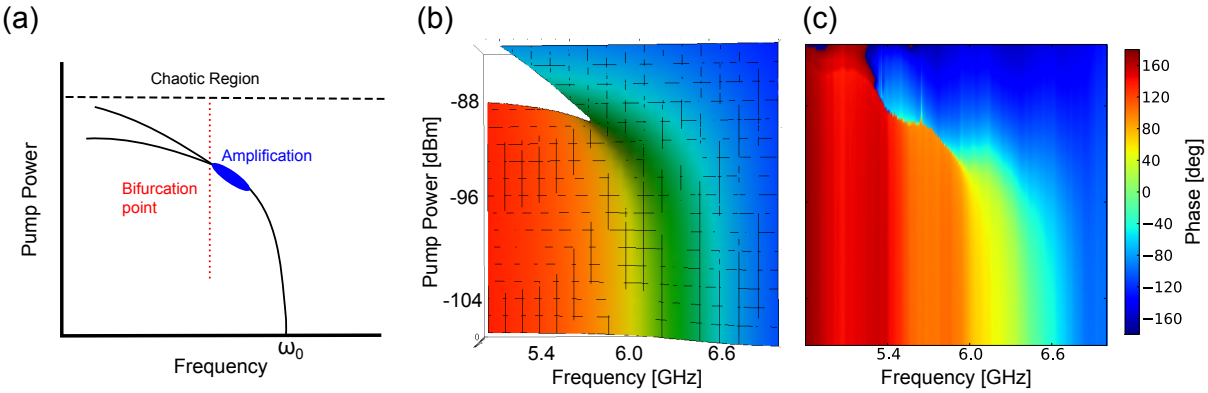

Figure A.2: Nonlinear phase response of the LJPA. (a) Schematic representation of the nonlinear phase response. At sufficient drive power the resonant frequency of the circuit begins to decrease and the phase response become sharper. This initially corresponds to a point of parametric amplification in which the driven oscillations of the nonlinear circuit act to amplify incoming signals close to the pump frequency. After this point there is a bifurcation region in which the amplifier has degenerate amplitude responses for a given drive frequency. Finally there is a chaotic region corresponding to the amplifier state hopping between wells in the cos potential. The second two plots represent theory (b) and data (c) plots of the nonlinear phase response. The two plots agree well numerically when experimental values are included for the theory model, but features in the experimental data exist due to impedance variations in the environment.

$$\left(\omega_r^2 - \omega^2 - 2i\omega\Gamma - \frac{\omega_r^2\delta_0^2}{4}\right)\epsilon(\omega) - \frac{\omega_r^2\delta_0^2}{8}\epsilon^*(2\omega_d - \omega)e^{2i\phi} = f(\omega) \quad \text{(A.24)}$$

$$\left(\omega_r^2 - \omega^2 + 2i\omega\Gamma - \frac{\omega_r^2\delta_0^2}{4}\right)\epsilon^*(\omega) - \frac{\omega_r^2\delta_0^2}{8}\epsilon(2\omega_d - \omega)e^{-2i\phi} = f^*(\omega) \quad \text{(A.25)}$$

From this we can see the coupling between the signal and idler mode in the circuit. In this case if the signal response is given by $\epsilon(\omega)$, then the idler response is given by $epsilon^*(2\omega_d - \omega_s)$ as in four-wave-mixing $\omega_i = 2\omega_d - \omega_s$.

From the equations above, we can calculate the frequency dependent signal and idler gain for a LJPA operated as a four-wave-mixing amplifier. For convenience, the resulting formulas for signal and idler gain are included below based on an in depth calculation in reference [103]. In this reference they find the signal and Idler gain in terms of the frequency detuning $\pm\Delta\omega = \omega_d \pm \omega$, in which case $\omega_s \to \Delta\omega$ and $\omega_i \to -\Delta\omega$. The gain equations are

$$G = |\frac{V_{out}}{V_{in}}|^2 \quad \text{(A.26)}$$

$$G(\Delta\omega) = |2iA(\Delta\omega)|^2 \quad \text{(A.27)}$$

$$G(-\Delta\omega) = |2iB(\Delta\omega)|^2 \quad \text{(A.28)}$$

The gain coefficient A and B are described by linear combinations of the drive terms $f(\Delta\omega)$ and $f^*(\Delta\omega)$. They are typically written in terms of the dimensionless terms

$$x = \frac{\omega_r - \omega_d}{\Gamma} \quad \text{(A.29)}$$

$$y = \frac{\omega_r\delta_0^2}{16\Gamma} \quad \text{(A.30)}$$

In these terms A and B are

$$A(\Delta\omega) = -\frac{(x-2y+\Delta\omega/\Gamma+i)}{y^2+(\Delta\omega/\Gamma+i)^2-(x-2y)^2} \quad \text{(A.31)}$$

$$B(\Delta\omega) = -\frac{ye^{2i\phi}}{y^2+(\Delta\omega/\Gamma+i)^2-(x-2y)^2} \quad \text{(A.32)}$$

Thus the frequency oscillations which result from the large pump tone, allow for parametric amplification of signal tones within the amplifier bandwidth. While this result described the amplifiers behavior it uses a simple model for the external impedance R. The next appendix covers the "pumpistor" model of three wave mixing, which provides a more intuitive description of the nonlinear circuit and its interaction with the environment.

Appendix B

Supplementary information for chapter 6: impedance matching and the environment in the pumpistor model

B.1 Taper design

We chose a Klopfenstein taper [76, 41] to transform the impedance from 50 Ω to 15 Ω over a large bandwidth while minimizing the pass-band ripple. Given the 1 μm limitations of our optical lithography process, a taper consisting entirely of a 15 Ω co-planar wave-guide (CPW) transmission line would require a 200 μm center-trace with a 1 μm gap width. For a microstrip geometry we were contrained to a low impedance imposed by our thin a-Si dielectric, which would require a 100 nm trace width for a 50 Ω line. A hybrid CPW/microstrip transmission line

shown in Fig. B.1 was adopted for the taper where a 10 μm center trace and 5 μm gap CPW was shunted by a variable density of 2 μm wide microstrip sections. The result is a 20 mm long tapered transmission line designed for a maximum reflection of -20 dB above 4 GHz.

The microstrip part of this geometry was created using multi-layer crossovers as additional shunt capacitance. We tested this model using microwave finite-element simulations to ensure that the shunt capacitance behaved as expected, and to correct for the change in inductance imposed by the crossovers. After extensive simulation we found that using a small crossover width of 2 μm and varying the density of crossovers provided the best control over impedance, as it allowed more evenly distributed shunt capacitance, prevented the inductance correction from becoming too large, and allowed the microstrip sections be applied uniformly over the meandered CPW.

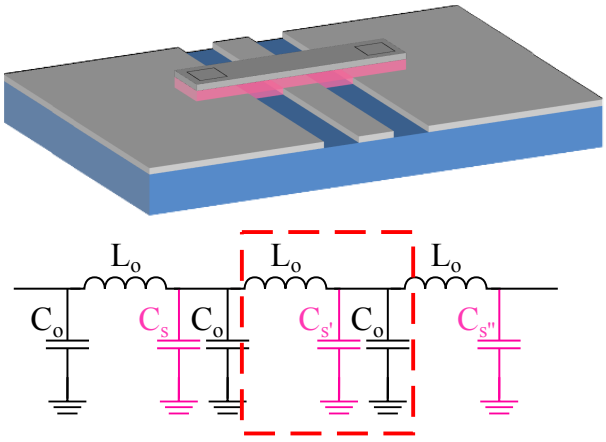

Figure B.1: The hybrid CPW/microstrip geometry. To match of a wide range of impedances with features defined by photolithography, the CPW with 10-5 μm center trace-gap widths was shunted by a variable density of shunt capactitor crossovers. As the crossover width is much lower than a wavelength, the capacitance per unit-length of the transmission line smoothly increases, continuously reducing the characteristic impedance from 50 Ω to 15 Ω. A unit cell for this taper in the dashed red box, is shown above.

B.2 Time domain reflectometry at milliKelvin temperatures

To verify that the profile of the taper followed the designed value, we employed time domain reflectometry (TDR) [104]. For this measurement, the time dependent reflection of a system is measured after the application of a fast step pulse, in order to measure the impedance of the system as a function of delay time, equivalent to the distance along the line. These measurements, shown in Fig. B.2, were carried out in an adiabatic demagnetization refrigerator (ADR) with a base temperature of $\sim$55 mK to ensure the aluminum was superconducting, otherwise the loss from the normal aluminum CPW would overwhelm the response TDR. All TDR data was taken using a Tektronix DSA8300 Digital Serial Analyzer with a 80E08B TDR/Sampling Module. The sampling module was connected directly to a CuNi line down to 4 K followed by a direct NbTi line down to the IMPA at 50 mK. Since the excitation voltage of this particular TDR sampling head is fixed, at 10 dB attenuator was applied to reduce the current at the device. The attenuated TDR data were calibrated using a 50 Ω terminator and an open at room temperature and corrected to obtain the proper impedances.

These TDR measurements were used to minimize reflections at the wire-bond due to excess inductance. As shown in Fig. B.2 excess inductance in the wire-bonds of the signal line can lead to a large impedance mismatch at the start of the taper. This mismatch can lead to standing waves which severely limit the usable frequency range of the IMPA. It was only after greatly reducing the length of the wire-bonds from 1-1.5 mm to 0.3-0.5 mm that we observed the enhanced performance reported here.

B.3 Pumpistor model

To understand the non-Lorentzian gain peaks and enhanced bandwidth in the IMPA, one must properly model the interaction of the JPA with the frequency dependent impedance environment. Since this is a reflection amplifier, the gain can be calculated by the reflection coefficient at the interface between the external circuitry and the JPA. The frequency dependent impedance of the external circuit can be modeled straightforwardly using a SPICE model with the parameters shown in Fig. B.3a. The tapered transmission line was modeled using 40 sections of equal delay transmission line corresponding to the impedance profile calculated using Ref. [41]. The mismatch due to the wire-bond was obtained using a section of transmission line at the input of the taper with a variable impedance and delay. The effect of the reflections due to the circu-

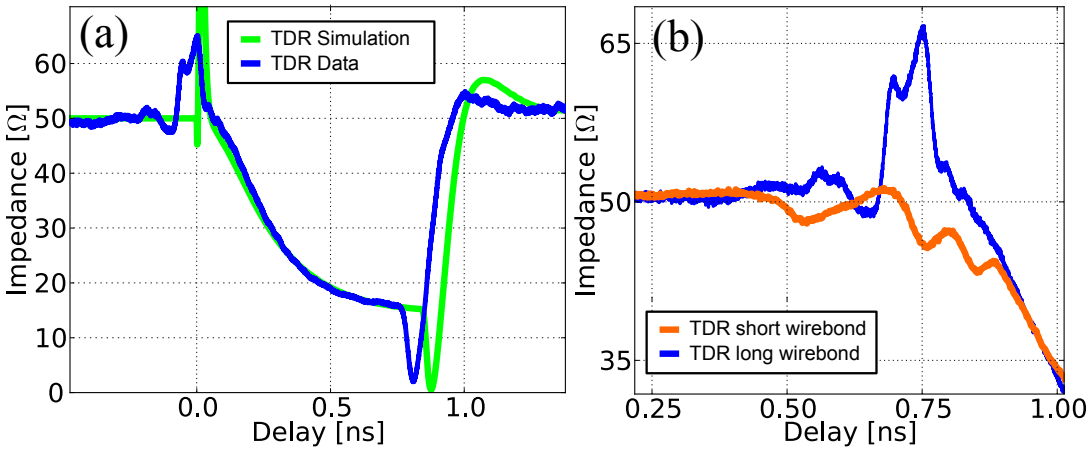

Figure B.2: TDR analysis of an IMPA sample. (a) The TDR response of experiment (at 50 mK) *vs.* theory (SPICE simulations) of the IMPA. The tapered sections agree well. Both curves end in a dip followed by a jump in impedance, corresponding to the lumped element resonator. The peaks seen before the taper begins correspond to an impedance mismatch at the wire bond due to a large series inductance ~ 1 nH. This mismatch can lead to standing waves on the taper which limit IMPA performance. (b) An expanded view of the wire-bond mismatch for a sample with long (1-1.5 mm) vs short (0.3-0.5 mm) wire bonds. The improved wire bond mismatch is similar in magnitude to that of an SMA connector seen at 0.5 ns.

lator was modeled using a resistor to ground whose value corresponds to the range of voltage standing wave ratio (VSWR) given by the manufacturer (Quinstar) specifications, at the end of a 50 Ω transmission line with variable delay.

The pumpistor model allows the flux-pumped SQUID to be treated as a linear cicuit component with the three inductances, given by Eqs. (1), (2), and (3) in the main text, where L_0 is the unbiased SQUID inductance in parallel with L_1 and L_2 which modify this bare inductance as pump power increases. To simplify the circuit analysis we express the effects of L_1 and L_2 as an equivalent parallel circuit with L_1' and L_2', such that L_1' modifies only the inductance of the circuit. Gain is introduce by the imaginary inductance of L_2' which behaves like a negative resistance, coupling power from the pump into the circuit. The parallel equivalent circuits are

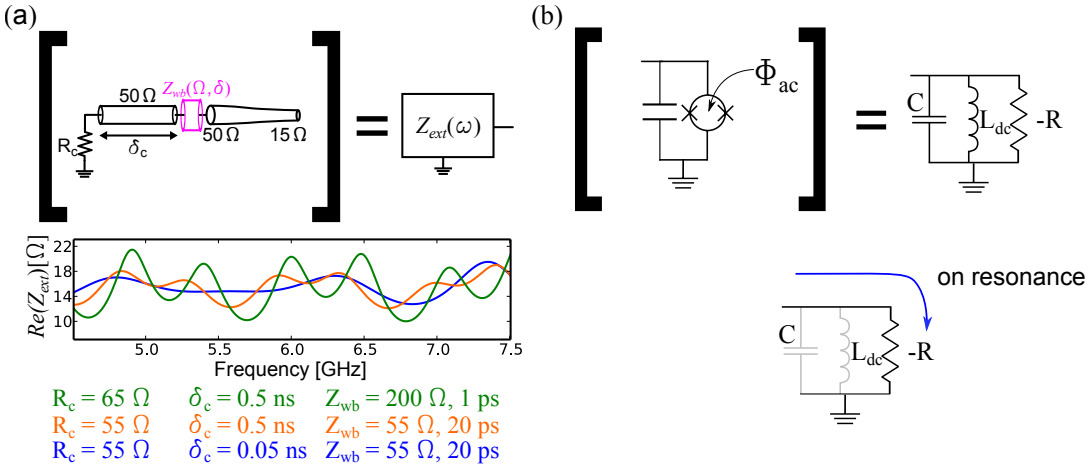

Figure B.3: Simulated frequency dependent performance for the Pumpistor model. (a) The impedance of the external circuit was calculated using the LT SPICE software package. The taper, wirebond and distance between the IMPA and circulator were modeled using transmission line segments of variable impedance and delay. The magnitude of the reflection due to the circulator was modeled as a resistor to groud with a mis-match corresponding to the VSWR specification for the circulator. (b) The JPA can be modeled as a linear circuit element using the pumpistor model. This circuit can be approxmated as a parallel LC resonator shunted by a negative resistance. On resonance, the current through the JPA will be shunted through the negative resistance and the impedance will be given by the total real component $-R$.

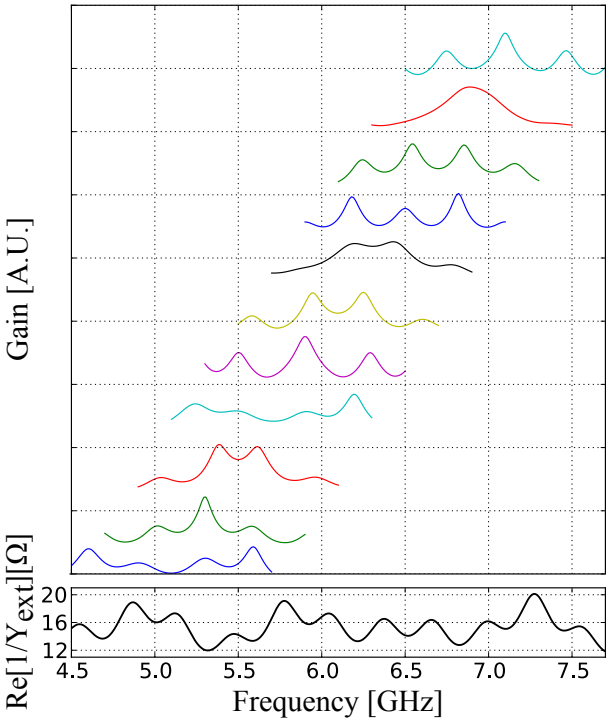

Figure B.4: Additional simulations of the pumpistor model. Frequency dependence of the calculated gain profiles (each with a max gain approximately 20 dB) for Y_{ext} corresponding to the 10 cm cable length shown in Fig. 3(b) of the main paper. These calculated gain profiles are mostly symmetric, with regimes of single, multiple and broadened peaks, and show good qualitative agreement with the data. The vertical gridlines are spaced by 20 dB.

given by

$$Q_s = \frac{\omega_s L_1}{-i\omega_s L_2} = \frac{1}{\omega_i [L_j/\cos(\pi\phi_q/\phi_0)] Y^*_{\text{ext}}(\omega_i)}, \tag{B.1}$$

$$L_1' = L_1\left(1 + 1/Q_s^2\right), \tag{B.2}$$

$$L_2' = L_2\left(1 + Q_s^2\right). \tag{B.3}$$

For resonant circuits here we use $Q_s = Q \approx 3$, so $L_1' \sim L_1$ and $L_2' = \alpha L_2 \approx 10 L_2$ to keep track of the series to parallel conversion. This allows us to write down an approximate circuit for the JPA shown in Fig. B.3, where C is the shunt capacitance of the parallel plate capacitor of the lumped element JPA, L_c is an effective inductance including L_0 and L_1 for a given bias

point and αL_2 gives a negative resistance in parallel. The circuit for these parallel admittances can be written as

$$Y_{\text{JPA}} = i\omega_s C + \frac{1}{i\omega L_c} - Y_R, \tag{B.4}$$

where Y_R is the magnitude of the JPA response given by:

$$Y_R = \frac{\pi^2 \sin^2(\pi\Phi_Q/\Phi_0)}{4\alpha\omega_s\omega_i L_{\text{j}}^2 Y^*_{\text{ext}}(\omega_i)} \left(\frac{\Phi_{ac}}{\Phi_0}\right)^2. \tag{B.5}$$

Simplifying Eqs. (B.4) with $\omega_o^2 = 1/L_c C$:

$$Y_{\text{JPA}} = \frac{1}{i\omega_s L_c}(1 - \frac{\omega_s^2}{\omega_o^2}) - Y_R \tag{B.6}$$

$$= \frac{1}{i\omega_s L_c}\frac{(\omega_o - \omega_s)(\omega_o + \omega_s)}{\omega_o^2} - Y_R. \tag{B.7}$$

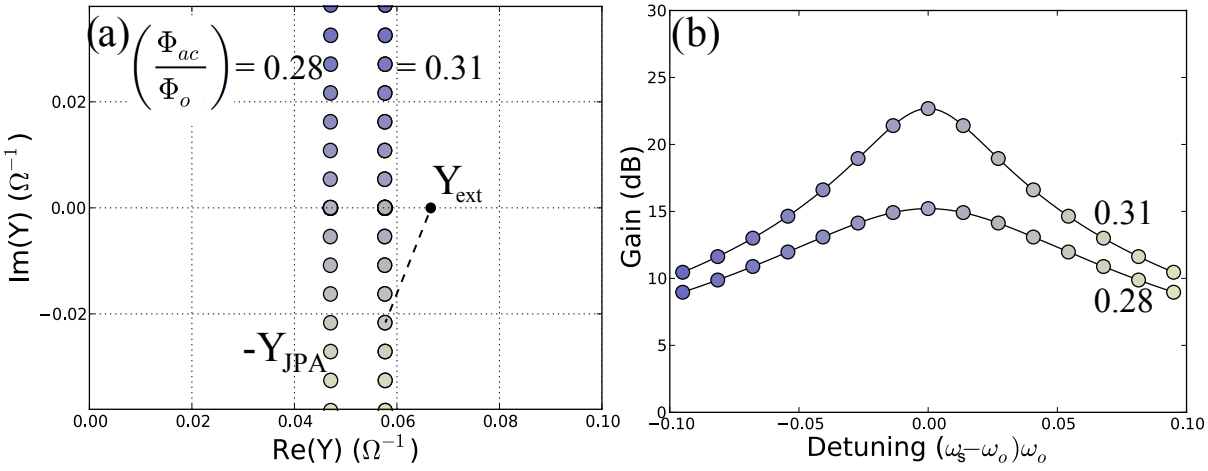

Figure B.5: The frequency dependent behavior of $-Y_{\text{JPA}}$ (open, colored circles) and Y_{ext} (black dot) in the complex plane. (a) For a constant Y_{ext}, Y_{JPA} is shown for two pump powers over a frequency range from $\omega_o - 0.1\omega_o$ to $\omega_o + 0.1\omega_o$ (each colored dot corresponds to a gain given in in panel (b)) where $\omega_o = \omega_p/2$. (b) The gain is inversely proportional to the distance between Y_{JPA} and Y_{ext} for a given frequency, indicated by the dashed line in (a). Since Y_{ext} is constant with frequency, the gain varies with the distance between the line given by Y_{JPA} and a point defined by Y_{ext}. The highest gain is found on resonance where Y_{JPA} is closest to Y_{ext}. The typical Lorenzian gain profiles are shown in (b) corresponding to the two different powers: Φ_{ac}/Φ_o = 0.28 and 0.31. Higher pump powers push $-Y_{\text{JPA}}$ to the right; as it nears Y_{ext} the gain increases and bandwidth decreases.

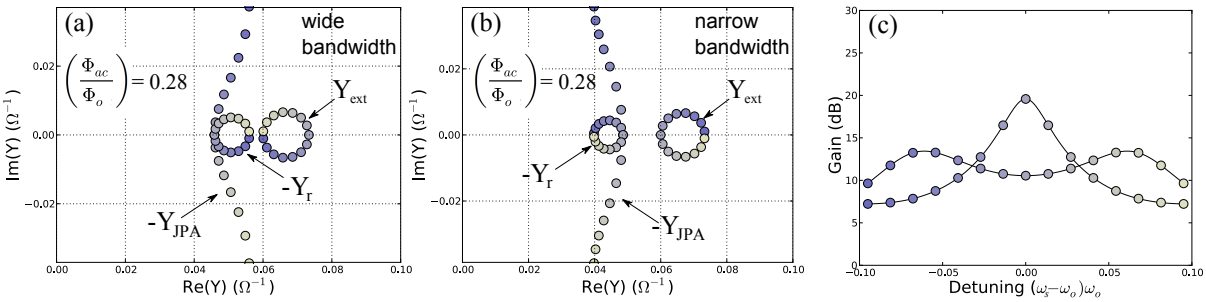

Figure B.6: The frequency dependent behavior of $-Y_{\text{JPA}}, -Y_R$ and Y_{ext} in the complex plane for a sinunsoidally varying Y_{ext}. The frequency at a given point, denoted by its color, each dot corresponds to a gain point shown in panel (c), where $\omega_o = \omega_p/2$. The gain at a given frequency is inversely propotional to the distance between $-Y_{\text{JPA}}$ and Y_{ext}. (a) In the wide bandwidth case, the profile Y_{JPA} nears Y_{ext} over a wider frequency range than otherwise. The resistive term reflects the variation in Y_{ext}, and displaces Y_{JPA}, providing a closer match to Y_{ext} over a broader range of frequencies than in Fig. B.5. In the narrow bandwidth case (b) Y_{JPA} approaches Y_{ext} over a smaller range of freuqnencies. This happens when $\omega_p/2$ is located at a local minimum of Y_{ext}. The rolloff in gain with detuning is due to the imaginary portion of Eq. (B.7) growing with increased detuning. The corresponding gain profiles for (a) and (b) are shown in (c).

With $\omega_o + \omega_s \approx 2\omega_o$, this yields Eqs. (5) from the main text.

This parallel to series conversion used to obtain Eq. (B.7) implicitly assumes Q_s is real. However, when a complex Y^*_{ext} is used to compute Q_s, the resulting correction to Y_{JPA} is negligible. It turns out the largest assumption in obtaining Eq. (B.7) is that $Q_s \approx 3$, a value constant in frequency. For this case α is predicted imprecisely over the narrow range of frequencies near resonance, as plotted in Fig. 3 of the main paper. However, α is simply a scaling factor for the pump power and Y^*_{ext}, both of which are not known precisely from experiment. These expressions are combined with the results of the SPICE model to obtain frequency dependent gain performance with good qualitative agreement to experiment as shown in Fig B.4. Only with careful and very precise measurement of reflections in the microwave chain can one yield quantitative agreement with the exact formulation.

For additional insight into the engineering of large bandwidth, interaction between the terms Y_{ext}, Y_{JPA} and $-Y_R$ (calculated using Eq. (B.7)) in the complex plane is shown in Figs. B.5 and B.6. The gain is inversely proportional to $|Y_{\text{ext}} + Y_{\text{JPA}}|$, equivalent to the distance between Y_{ext} and Y_{JPA}. By increasing pump power, $-Y_R$ increasingly deforms Y_{JPA}. Large bandwidth is achieved by minimizing the distance between Y_{JPA} and Y_{ext} over a larger range of frequencies. This is shown in contrast to the ideal case with no variation in Y_{ext}, which produces the typical Lorentzian gain profile.

B.4 "Pumpistor" predictions on saturation power

According to the "pumpistor" model for degenerate parametric amplification, saturation power depends directly on the ratio of signal amplitude to critical current and scales inversely with coupled Q. As bandwidth should also scale as $1/Q$ this would compensate an increase in amplified noise with a commensurate increase in saturation power. In the IMPA however, we see a much larger increase in bandwidth up to about 700 MHz. This large bandwidth exhibited at certain pump frequencies, might be a concern if the additional amplifier quantum fluctuations limit the saturation power. Considering the amplified quantum fluctuations at 6.7 GHz for 700 MHz of bandwidth and an average gain of 17.5 dB we have a total output power of

$$P_{out} = 10 * \log\left(\frac{6.7 * 10^9 * h * 7 * 10^8}{1 * 10^{-3}}\right) + 17.5 \approx -97.5\, dBm \tag{B.8}$$

If we compare this to the average input saturation power for a coherent signal (-108 dBm) with the average gain 17.5 dB we get -90 dBm output saturation power. Previous LJPA devices

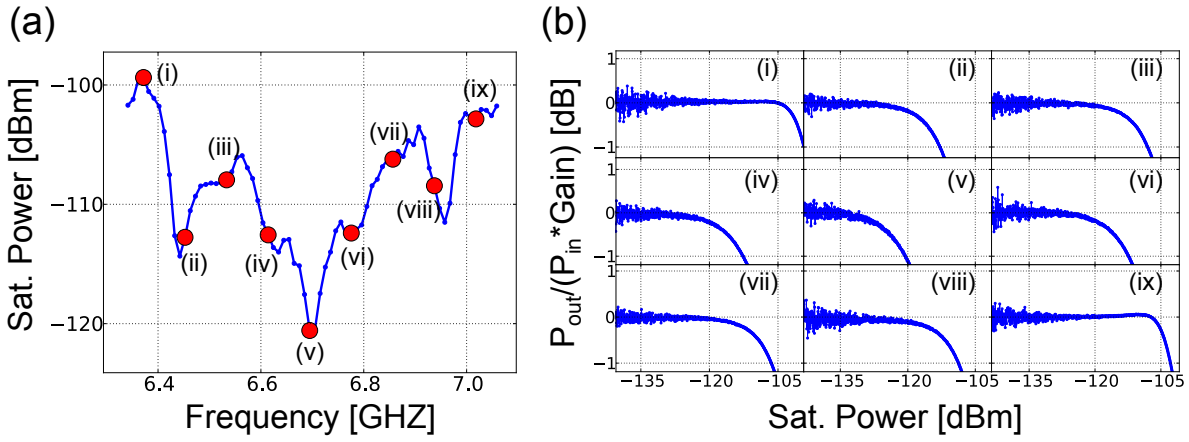

Figure B.7: (a) Graph of saturation power vs. frequency from the main text. Large (red) dots are used to denote frequencies for which a full transmission power vs input signal power curve is shown. (b) Graphs of transmission power vs. input signal power for the points depicted in (a). Here the output power has been scaled by the low signal power limit, such that the ideal transmission is 0 and -1 denotes the 1 dB compression point. The first 8 graphs display an ideal linear dependence on power before saturating to -1 dB. The final graph at the edge of the amplified range displays a slight increase in gain, up by 0.2 dB, before saturating in the normal way. In general, this small upturn is only observed at the edge of the 700 MHz span.

with a coupled-Q of 10 have displayed input saturation values of -115 dBm at 20 dB of gain, giving an output saturation power of -95 dB [69]. Thus the increase in average output power is consistent with the expected 5 dB increase going from a coupled Q of 10 to a coupled Q of 3. By lowering the coupled Q and operating the device at a slightly lower gain, the amplified quantum fluctuations are 7.5 dB below the saturation power limit for a coherent signal.

Additional nonlinearities can arise in the gain vs. signal power curve either when the signal is significantly detuned from the pump or when a non-optimal pump power and flux value is chosen. In these cases the signal can act as a secondary input pump, which first causes the gain at the signal frequency to increase with signal power before saturating and compressing below the original level. While this effect can be calibrated for in single frequency measurements, it can cause distortion in broader band or pulsed signals. If the large bandwidth of our device

was due to more complicated nonlinear dynamics it is a possible concern that certain regions of the 700 MHz span might display such non-ideal saturation behavior. We demonstrate in Fig. B.7 a series of representative curves of transmission power (scaled to 0) vs. input signal power for various frequencies within the 700 MHz span. All curves other than (ix) demonstrate ideal linear behavior before saturation. In the case of curve (ix), a light upward deviation (0.2 dB above the background) occurs before the gain compresses. These curves are generally representative of the entire span, with small non ideal behavior confined to regions sections at the very edges. Far less ideal saturation power behavior is observed outside of this region, but only where the gain falls off sharply as expected.

B.4.1 Noise measurements

The Paramp system noise values displayed in this paper were calculated using the method of signal to noise ratio improvement [55, 69] discussed in the main text. In this method the amplified noise and transmission amplitude is first measured when the amplifier is turned off. The amplifier is then turned on and the amplified noise and transmission amplitude are once again measured. By comparing the increase in transmission power (gain) to the increase in amplified noise we can measure system noise amplified by the paramp provided we know the system noise amplified by thehigh electron-mobility transistor (HEMT) . In this measurement signal loss between the paramp and the HEMT can make this ratio seem smaller and must be taken into account when measuring the amplified HEMT noise. In our setup, shown in Fig. B.8, we use a y-factor measurement [41] with a heated 50 Ω resistor on the cold plate of our refrigerator.

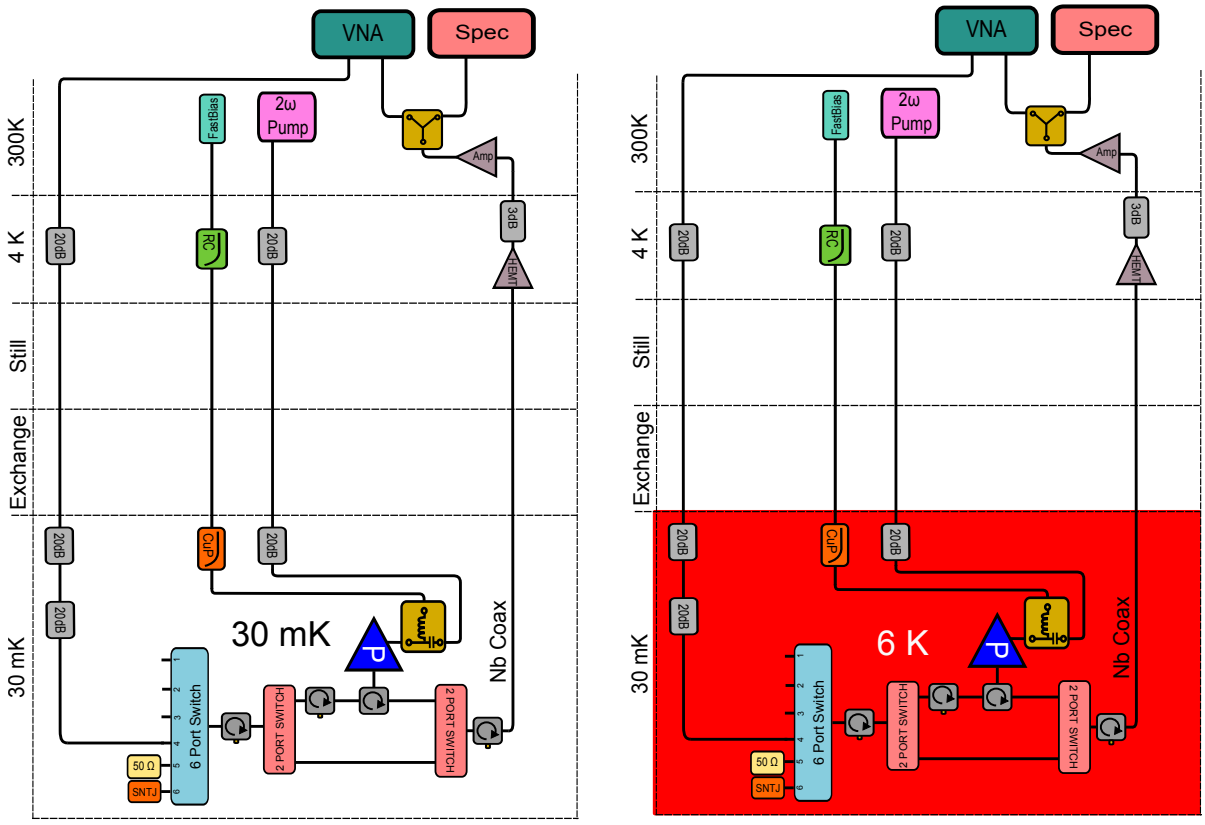

Figure B.8: Schematic for paramp experimental setup used to characterize noise. The left figure shows the experimental setup with paramp, circulators, and microwave switches at base temperature. The 50 Ω on the 6 port switch is heated to calibrate the HEMT noise. The right schematic shows the portion of the fridge heated (red) to perform a y factor measurement. When this calibration is done the 2 port switches are are set to the straight through path which provides 2 circulator channels between the 50 Ω and the HEMT, the same number of circulators between the HEMT and signals amplified by the paramp. As circulators are the dominant source of loss, the HEMT system noise seen by the paramp and the 50 Ω should be equivalent.

In this setup both the 50 Ω resistor and the paramp are connected to the HEMT by copper microwave flex cables at 30 mK, 2 circulators, and a Nb coaxial cable connected between 30 mK and the HEMT at 4 K. Due to the difficulty of heating just the 50 Ω resistor we use a method in which the entire cold plate of the refrigerator in heated to a much larger temperature (6 K) and allowed to stabilize before a measurement is performed. The HEMT amplifier is on a different plate and its temperature is held steady over the course of this experiment. This methodology, while allowing for accurate temperature measurement of the resistor, can mis-characterize the effect of loss between the resistor and the HEMT. Any dissipative loss coming from attenuation on the 30 mK plate would add noise to the signal as it was also at the higher 6 K temperature. We assume the dominant source of potential loss comes from the microwave circulators, as the superconducting and copper cables should have negligible loss at these temperatures. The circulator insertion loss was measured at room temperature to be between 0.5 and 0.3 dB. To account for this we have added 1 dB error bars to our measurement of the HEMT noise which are in turned scaled to give error bars for the signal to noise ratio improvement of the paramp.

Appendix C

Supplementary information for chapter 7: traveling wave amplifier design and theory.

C.1 TWPA theory: eoupled mode equations

A circuit diagram of a Josephson junction embedded nonlinear transmission line is shown in Fig. 1(a) in the main text. The Josephson inductance is current dependent,

$$L(I) = L_0 \left[1 + \frac{1}{2}\frac{I^2}{I_c^2}\right], L_0 = \frac{\Phi_0}{2\pi I_c} \tag{C.1}$$

where Φ_0 is the magnetic flux quantum and I_c is the critical current of the Josephson junction. Consequently, propagation along the transmission line is described by a nonlinear wave equation:

$$\frac{\partial^2 I}{\partial z^2} - \frac{1}{\tilde{c}^2}\frac{\partial^2}{\partial t^2}\left[I + \frac{1}{6}\frac{I^3}{I_c^2}\right] = 0,\ \frac{1}{\tilde{c}^2} \approx LC, \tag{C.2}$$

Eqn. C.2 is analogous to the case of light traveling in nonlinear Kerr media, in which the index of refraction is intensity-dependent. The propagation can be solved using the coupled-mode equations (CME) method from nonlinear optics. [105]

We write the pump, signal and idler as $I = 1/2\left[\sum_n A_n e^{i(k_n z - \omega_n t)} + c.c.\right]$ where A_p, A_s and A_i represent the three traveling waves of pump, signal and idler, respectively. Following the CME approach, we derive the coupled-mode equations under the slow wave approximation (SWA), [51] [106]

$$\begin{aligned}
\frac{dA_p}{dz} &= \frac{ik_p}{16I_c^2}A_p|A_p|^2 \\
\frac{dA_s}{dz} &= \frac{ik_s}{16I_c^2}\left(2A_s|A_p|^2 + A_i^* A_p^2 e^{-i\Delta k z}\right) \\
\frac{dA_i}{dz} &= \frac{ik_i}{16I_c^2}\left(2A_i|A_p|^2 + A_s^* A_p^2 e^{-i\Delta k z}\right),
\end{aligned} \tag{C.3}$$

where $\Delta k = k_i + k_s - 2k_p$ is the phase mismatch calculated from weak-signal dispersion of the transmission line. The term on the right hand side of the pump equation represents the self-phase modulation due to the AC pump current interacting with itself. Analogous cross-phase modulation processes are represented by the first term on the right hand side of the signal and idler equations; the other term presents the conversion of two pump photons to a signal photon and an idler photon. Under the undepleted pump assumption $|A_p| \gg |A_i|, |A_s|$, the pump can be solved first

$$A_p = A_p(0)e^{i\gamma k_p z}, \gamma = \frac{|A_p(0)|^2}{16I_c^2}, \tag{C.4}$$

where γ is an unit-less coefficient reflecting the strength of the nonlinear effect and $\phi_{nl} = \gamma k_p z$ is the nonlinear phase shift of the pump also referred to as the self phase modulation (SPM) in nonlinear optics. Using the pump solution, the signal and idler can be solved perturbatively. Here, we write the solution in a matrix form,

$$\begin{aligned}
\begin{bmatrix} A_s(z) \\ A_i^*(z) \end{bmatrix} &= M(z, A_p(0)) \begin{bmatrix} A_s(0) \\ A_i^*(0) \end{bmatrix}, \; M = \begin{bmatrix} u_{11} & u_{12} \\ u_{21} & u_{22} \end{bmatrix} \\
u_{11} &= \left[\cosh(gz) + i\frac{\kappa}{2g}\sinh(gz)\right] e^{i(2\gamma k_s - \frac{\kappa}{2})z}, \\
u_{12} &= \left[\frac{i\gamma k_s}{g} e^{2i\phi_0}\sinh(gz)\right] e^{i(2\gamma k_s - \frac{\kappa}{2})z}, \\
u_{21} &= \left[-\frac{i\gamma k_i}{g} e^{-2i\phi_0}\sinh(gz)\right] e^{-i(2\gamma k_i - \frac{\kappa}{2})z}, \\
u_{22} &= \left[\cosh(gz) - i\frac{\kappa}{2g}\sinh(gz)\right] e^{-i(2\gamma k_i - \frac{\kappa}{2})z}, \\
e^{i\phi_0} &= \frac{A_{p0}}{|A_{p0}|}, \; g = \sqrt{\left(\frac{k_s k_i}{k_p^2}\right)(\gamma k_p)^2 - \left(\frac{\kappa}{2}\right)^2}, \; \kappa = 2\gamma k_p + \Delta k.
\end{aligned} \tag{C.5}$$

If the transmission line has no intrinsic dispersion ($\Delta k = 0$, as is our case for the junction embedded transmission line in the low frequency limit), it can be derived from Eqn. C.5 that the maximum signal gain (occurring at $\omega_s = \omega_p$) is quadratic in ϕ_{nl} or z (thus the length of the line)[83, 107] ,

$$g \;\rightarrow\; 0, \; u_{11} = (1 + i\gamma k_p z)e^{i\gamma k_p z}, \; G_q = |u_{11}|^2 = 1 + \phi_{nl}^2. \tag{C.6}$$

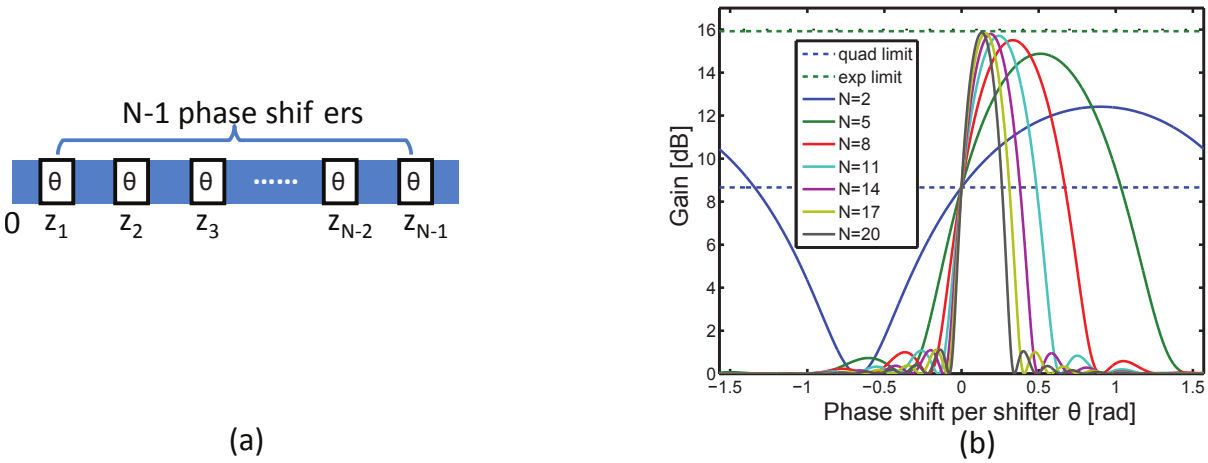

Figure C.1: (a) Configuration of $N-1$ phase shifters inserted between N nonlinear transmission line sections. (b) Comparison of enhanced gain with the quadratic gain and exponential gain limits. $\phi_{nl} = 2.5$ is assumed which corresponds to our device.

.

If additional dispersion $\Delta k = -2\gamma k_p$ is introduced (as is the case in the dispersion engineered kinetic inductance parametric amplifier [51]) so that the phase matching condition is perfectly met ($\kappa = 0$), exponential signal gain can be achieved,

$$G_e \quad = \quad \cosh^2(\phi_{nl}) \approx \exp(2\phi_{nl})/4. \tag{C.7}$$

C.2 Resonantly Phase-matched TWPA

Assume that N - 1 phase shifters (resonators) are inserted in between N sections of dispersionless line at position z_m (see Figure C.1). We treat the resonators as perfect phase shifters for which $S_{21} = 1$ at all frequencies except the pump, where we have $S_{21}(\omega_p) = e^{i\theta}$. The output

signal/idler at z_N and the total signal gain can be calculated by cascading the M matrices

$$\begin{bmatrix} A_s(z_N) \\ A_i^*(z_N) \end{bmatrix} = M(z_N - z_{N-1},\ A_p(z_{N-1}^+))M(z_{N-1} - z_{N-2},\ A_p(z_{N-2}^+))...M(z_1,\ A_p(0)) \begin{bmatrix} A_s(0) \\ A_i^*(0) \end{bmatrix}$$
$$= \hat{M}(z_N, A_p(0)) \begin{bmatrix} A_s(0) \\ A_i^*(0) \end{bmatrix},\ G_r = |\hat{M}_{11}|^2. \quad \text{(C.8)}$$

where $A_p(z_m^+)$ has included the additional phase shift θ from the phase shifter at z_m and $\hat{M}$ is the cumulative transfer matrix for signal/idler from $z = 0$ to $z = z_N$. A Matlab program is written to compute $\hat{M}$ and G_r. We are mostly interested in the dependence of G_r on the number of phase shifters N and the phase shift per shifter θ. Fig. C.1 (b) shows the calculation results, using the realistic design parameters of the device. It is clear that the gain is greatly enhanced by the phase shifters, even when only 1 phase shifter ($N = 2$) is inserted. The enhancement increases with N and approaches the exponential gain limit for large N. In fact, the enhanced gain is very close to G_e limit (green dashed line) for 7 or more phase shifters ($N > 8$). Adding resonators per unit LC ladder was recently proposed in [95] to achieve phase matching condition.

An ideal phase shifter can be approximated by a $\lambda/4$ resonator capacitively coupled to the transmission line. The resonator provides a frequency dependent phase shift as well as an amplitude dip which is maximized on resonance. With only a few resonators 5-10, it is impossible to achieve the desired phase shift without tuning the pump into the amplitude dip of the resonator. This will destroy the parametric gain through internal reflections in the transmission line. To ensure we can achieve the desired phase shift with virtually no affect on pump amplitude we must use a design with $N \geq 20$. The dependence of phase and amplitude on frequency

is shown for several numbers of resonators in Fig. C.2. As these simulations were only meant to determine phase shift vs amplitude dip, they do not include the possibility of an additional phase shift coming from the periodic placement of resonators. The simulated phase shift shown in Fig. 3(c) of the main text includes this effect and better reflects experimental conditions.

C.3 TWPA device parameters

Constructing the nonlinear sections of the TWPA requires balancing between the critical current of the Josephson junctions and the cutoff frequency of the LC ladder. If the critical current is increased it will require a larger pump to achieve the same nonlinearity. Saturation power depends directly on pump amplitude so a higher critical current for each junction is desir-

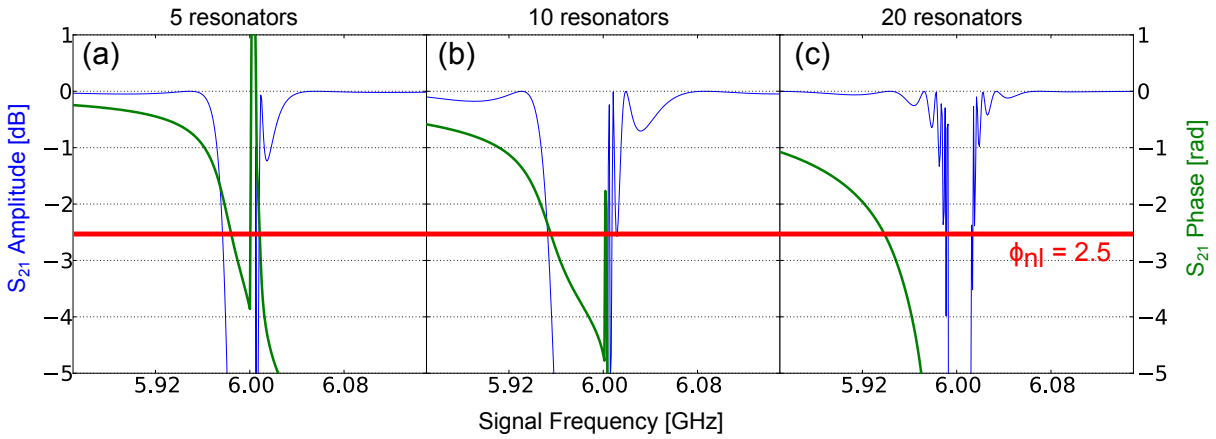

Figure C.2: Plots showing simulated signal phase and amplitude vs frequency for (a) 5 resonators, (b) 10 resonators, or (c) 20 resonators in a TWPA circuit. The plots show that while only a few ideal phase shifters are necessary for phase matching, $\lambda/4$ resonators also cause an amplitude dip which can affect pump transmission close to resonance. Adding additional resonators allows for a greater phase shift with a smaller reflected pump amplitude. The red line indicates a nonlinear phase shift of 2.5 radians which is necessary to achieve gain greater than 15 dB.

.

able. However higher critical current also means a lower inductance per section in the LC ladder which means a higher cutoff frequency given by $1/(2\pi\sqrt{L_{sec}C_{sec}})$. A lower cutoff frequency is desirable because it will prevent parasitic coupling of the pump to higher frequency modes[98]. Thus we constructed each section with three higher critical current junctions in a row, such that $L_{sec} = 3L_j$. This allowed us to use higher critical current junction while also lowering the cutoff frequency of the transmission line by a factor of three. The capacitance was then increased to maintain $\sqrt{\mathcal{L}/\mathcal{C}} \approx 50\,\Omega$ given inductance per unit length $\mathcal{L}$ and capacitance per unit length $\mathcal{C}$

As stated in the main text the critical current of each junction was designed to be $\approx 5\,\mu$A which corresponds to an inductance of 65 pH and a section inductance of 195 pH. The capacitance of each parallel plate capacitor was designed to be 117 fF leading to a cutoff frequency of 33 GHz. This cutoff frequency combined with the dispersion engineering is sufficient to prevent the propagation of shock-waves in the transmission line[98]. The geometric inductance and capacitance per unit length were extracted from simulations matching the nonlinear transmission line geometry. Combining the simulation data with the single section values give $\mathcal{L} = 3.5\,\mu$H/m and $\mathcal{C} = 1.5$ nF/m for a combined impedance of $\approx 48\,\Omega$. The impedance was designed to be less than $50\,\Omega$ initially as impedance will increase slightly when in operation do to the nonlinear inductance.

The resonators were initially designed to operate at a frequency of 7 GHz but shifted lower in frequency to 6.1 GHz due to kinetic inductance in the thin 60 nm aluminum film. Resonators being placed at the end of each nonlinear section means they are $1100\,\mu$m apart. The propa-

gation velocity coming from the inductance and capacitance per unit length means $1100\,\mu$m corresponds to $\lambda/2$ for 6.2 GHz. This is consistent with what we observe experimentally.

C.4 Measuring TWPA transmission

For the TWPA to function as an effective amplifier it must first function as a transmission line. If the individual sections are not well impedance matched, internal reflections can destroy the

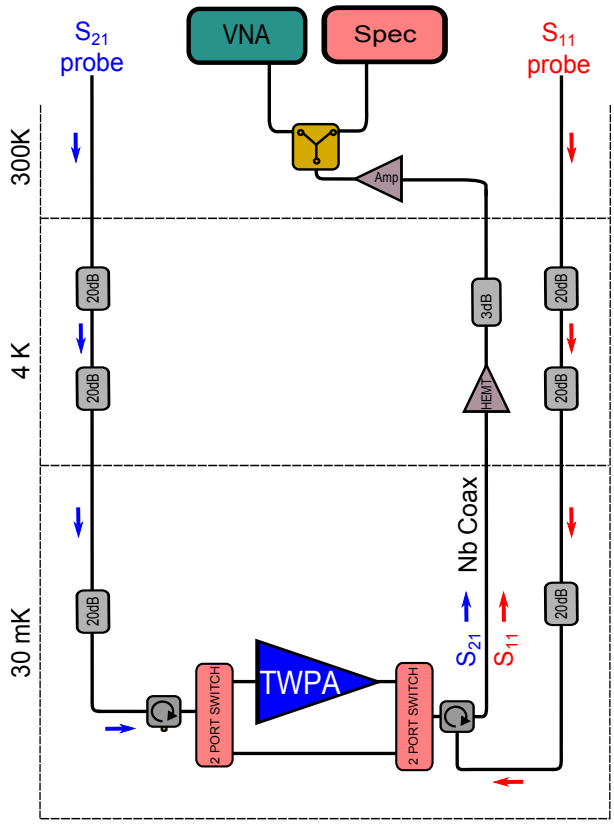

Figure C.3: Diagram of the transmission measurement experiment used to characterize TWPA transmission and reflection amplitudes. The output port of a vector network analyzer (VNA) can be attached to either port and combined with the TWPA pump. The signal output is then split at room temperature between the VNA and a spectrum analyzer (SPEC) used for noise measurements. This setup allows us to probe both S_{21} and S_{11} in a single cool down of the refrigerator using equivalent measurement paths.

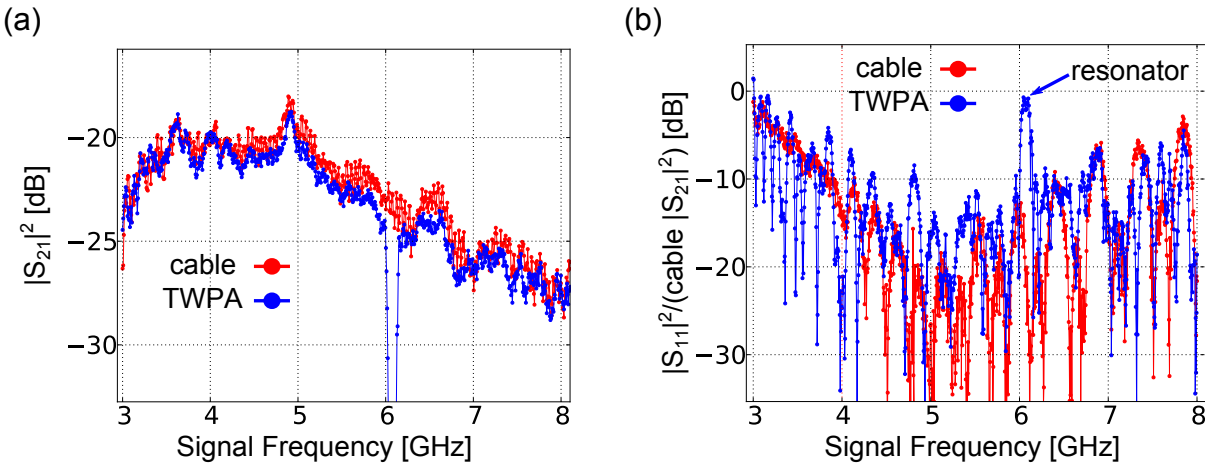

Figure C.4: (a) Measured transmission amplitude of both a low loss microwave cable (red) and the TWPA (blue). The TWPA shows a slight decrease in transmission over the range but the deviation is only 0.5 dB. (b) Measurement of reflection amplitude of the cable (red) and the TWPA (blue) scaled relative to the cable transmission from (a). The TWPA's higher reflection amplitude is consistent in magnitude with the lower transmission from part (a), which indicates the majority of the difference comes from reflection in the TWPA rather than loss in the materials.

coupling between different frequency modes. Excessive loss in the line can become a source of noise which will make quantum-limited amplification impossible. To check the transmission line behavior of the TWPA we measured its transmission (S_{21}) and reflection (S_{11}) amplitude compared to that of a standard low loss microwave cable. This experiment was carried out using two 2-port cryogenic microwave switches as well as two cryogenic microwave circulators, shown in Fig. C.3. The switches were used to swap the TWPA and cable in the transmission path to the high electron mobility transistor (HEMT) amplifier. Two equivalent microwave inputs were used to probe the transmission and reflection simultaneously. The S_{21} probe line goes through the first circulator, the TWPA, and finally the last circulator, before going to the HEMT. The S_{11} line goes to the third input of the last circulator which funnels it to the opposite end of the TWPA. Any reflected signal then makes its way to the HEMT.

The data from this experiment is shown in Fig. C.4. Figure C.4 (a) shows that the TWPA and cable have the same transmission profile over the majority of the bandwidth. There is an average decrease in transmission of 0.5 dB relative to a copper cable, except at the resonator frequency (6.1 GHz) where there is a significant amplitude dip. The S_{21} data for both devices is shown in Fig. C.4 (b) with both data sets scaled relative to S_{21} for the cable. The TWPA reflection is in general less than -10 dB relative to the cable transmission, which is consistent with -0.5 dB less transmission. These two data sets taken together suggest that any drop in transmission through the TWPA comes from reflections rather than loss in the transmission line.

Appendix D

Supplementary information to chapter 8: weak measurement calibration, sample parameters, and error analysis.

D.1 Weak measurement calibration

As discussed in the main text the ancilla readout is imperfectly correlated to the Bell qubit's state. When measuring in the Z basis, $\langle Z \rangle_\alpha = \sin(\phi)\langle Z \rangle_\beta$, shown in Fig. D.1 (a) along with the ideal curves $\pm\sin(\phi)$. To calibrate this weak measurement we must first relate the measurement angle ϕ to microwave drive power, by fitting to a measurement of $|1\rangle$ state probability vs. π-pulse amplitude. The most straight forward calibration would then be to divide $\langle Z \rangle_\alpha$ by $\sin(\phi)$ shown in the blue curves in Fig. D.1 (b), but this method causes drift in the mean at the

smallest angles.

This simple calibration fails because the raw data curves shown in Fig. D.1 (a) converge to a value slightly below zero. This means that for the weakest measurements, the simple angle calibration will under-correct a $|1\rangle$ state measurement and over-correct a $|0\rangle$ state measurement. This over-correction of the $|0\rangle$ state is problematic, since calibrated values for $\langle Z\rangle_\alpha$ not bounded by ± 1 will possibly violate the inequality incorrectly. To prevent this, we instead use a data based calibration for each ancilla using the average of the $|0\rangle$ state measurement curve. This has the advantage of bounding the mean of the calibrated result by ± 1, at the expense of accentuating the drift in the mean of the $|1\rangle$ state measurement towards 0. The results of this $|0\rangle$ state calibration are shown in the green curves in Fig. D.1 (b).

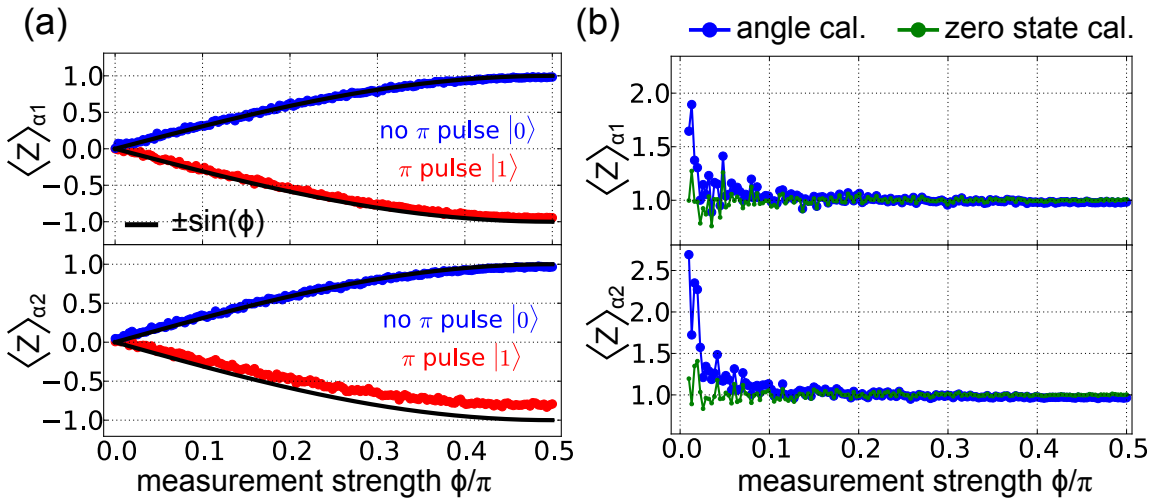

Figure D.1: (a) Raw measurement of $\langle Z\rangle$ vs. measurement strength ϕ for both α_1 and α_2 along with an ideal curve of $\pm\sin(\phi)$. Due to decoherence, measurement error, and possible calibration error the data does not perfectly follow the $\pm\sin(\phi)$ curves and converges to a value slightly below 0 at the weakest measurement strength. (b) $|0\rangle$ state calibrations done using both the $1/\sin(\phi)$ method (blue) and the point by point calibration (green). In the $1/\sin(\phi)$ calibration the mean of the $|0\rangle$ state measurement drifts above 1 at the weakest measurement angles, while the mean follows 1 for the point by point case.

To apply this calibration to the correlator terms, we must first express them in terms of the measurement operator $\langle Z \rangle$. In a superconducting system the state rotations are used to map the desired measurement basis onto the ground ($|0\rangle$) and excited ($|1\rangle$). For the ancilla measurement this is equivalent to mapping onto the Z measurement axis. Given probability P(1) of measuring the excited ($|1\rangle$) state, $\langle Z \rangle = 1 - 2P(1)$. After mapping state probabilities onto the Z measurement axis we can express the correlator as $E(\alpha, \beta) = \langle Z \rangle_\alpha \langle Z \rangle_\beta$. Expressed in this way we can see that for calibration factor $cal(\phi) \approx 1/\sin(\phi)$, $E_{cal}(\alpha, \beta) = E(\alpha, \beta) * cal(\phi)$. Extending this to the BLGI we calibrate each term depending on the ancilla qubit being measured such that $E(\alpha_1, \beta_2) \rightarrow E(\alpha_1, \beta_2) * cal(\phi_1)$, $E(\beta_1, \alpha_2) \rightarrow E(\beta_1, \alpha_2) * cal(\phi_2)$, $E(\alpha_1, \alpha_2) \rightarrow E(\alpha_1, \alpha_2) * cal(\phi_1) * cal(\phi_2)$, and $E(\beta_1, \beta_2)$ remains unchanged.

D.2 Error analysis and pulse sequence optimization

While the algorithm and weak measurement scheme are simple in design, dependence on correlations between multiple qubits makes $\langle C \rangle$ sensitive to multiple error mechanisms. As all four qubits were operated away from the flux insensitive point they were more susceptible to dephasing effects. The amplitude of $\langle C \rangle$ vs. dephasing error per qubit is shown in Fig. D.2(a). The violation amplitude is relatively robust to this error, and can sustain error rates of up to 30 percent while still exhibiting non-classical correlations. The second major error mechanism was reduced measurement visibility coming from T_1 energy decay or spurious $|1\rangle$ state population. The effect on $\langle C \rangle$ vs. single qubit measurement visibility is shown in Fig D.2(b). The correlation amplitude is more sensitive to this reduced measurement visibility and is signifi-

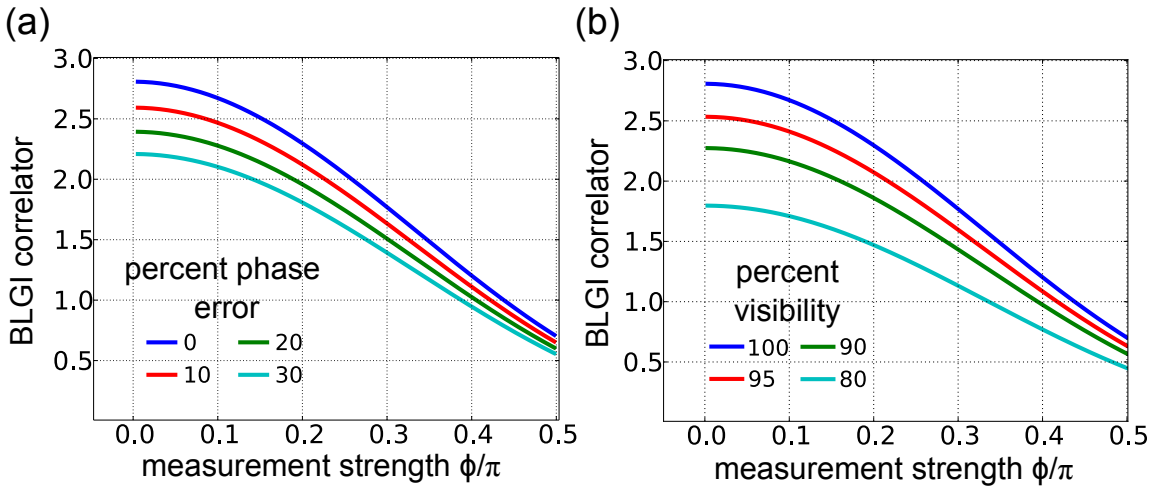

Figure D.2: Effect of error mechanisms on BLGI correlations. (a) Amplitude of $\langle C \rangle$ vs. measurement strength for various single qubit dephasing error rates. The single qubit dephasing error rate can be thought of as roughly T_2/(gate time) in the simplest case, but can be improved through the addition of echo pulses. (b) Amplitude of $\langle C \rangle$ vs. measurement strength for various single qubit measurement visibility values. The system shows a greater sensitivity to this error mechanism and cannot tolerate a visibility much below 90 percent.

cantly degraded at even 90 percent. In both cases, the presence of errors not only lowers the maximum violation possible but the highest measurement strength at which a violation first occurs. As weaker measurement angles require finer calibration and provide noisier data, it is preferable to achieve a violation at the largest measurement strength possible.

Given the sensitivity of $\langle C \rangle$ to various decoherence mechanisms it was important to reduce the BLGI pulse sequence time as much as possible for higher coherence. This is most notable during the weak measurement portion when we carry out simultaneous adiabatic CZ gates[27] between both ancilla-Bell pairs. Lastly, we introduced spin echo pulses in the middle of the algorithm which cancel out dephasing during the pulse sequence while simply transforming the original $|\Psi^+\rangle$ Bell state to a $|\Psi^-\rangle$. To maximize measurement fidelity, we used a wide bandwidth parametric amplifier [82], to ensure a high signal to noise ratio and shorter readout

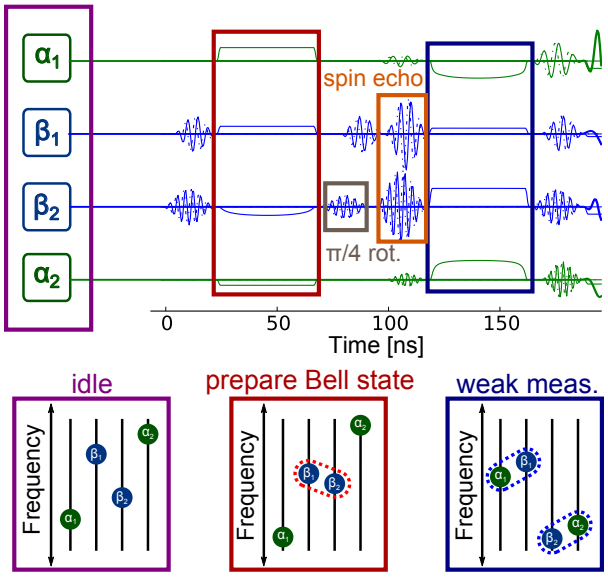

Figure D.3: (above) Full pulse sequence of the BLGI algorithm, including spin echo pulses on the Bell qubits to reduce dephasing. The weak measurements were carried out simultaneously to further streamline the algorithm. (below) Frequency diagram of the 4 qubits showing their placement in frequency space the pulse sequence, in particular the various detunings during the adiabatic CZ gates.

time. A separate measurement at the beginning of the pulse sequence was used to herald [39] the qubits to the ground state, but this was a small ($\sim$6 percent) effect. Lastly, we implemented numeric optimization of the adiabatic CZ gates using the ORBIT protocol [108] to fine tune parameters for the final data set. The full Pulse sequence and frequency placement of the qubits during the algorithm is shown in Fig. D.3.

During the numeric optimization of the pulse sequence, single qubit phases can be adjusted slightly to increase correlations, leading to a larger violation. This is equivalent to changing the final rotation angle of the detectors slightly ($\sim$ 3 degrees). The nature of the BLGI makes it immune to such rotations as loss of correlations in one correlator is naturally made up for in another. additionally, the initial detector rotation b was chosen based on the maximum of the

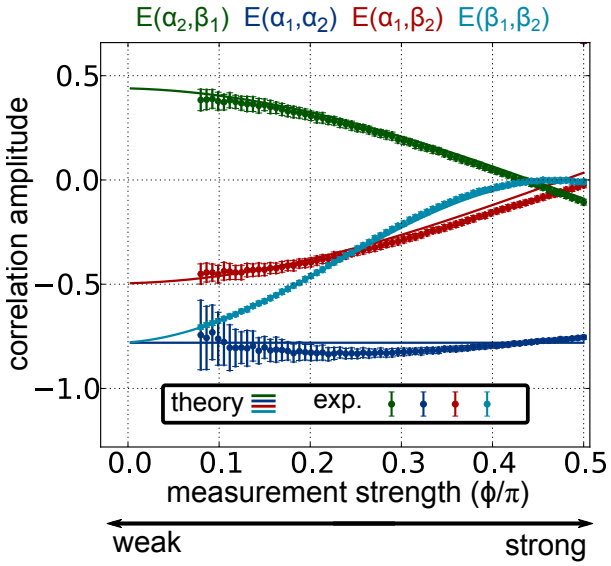

Figure D.4: Graph showing both experimental data (points) and theoretical predictions (lines) for the four BLGI terms vs. measurement strength ϕ. The data set was taken by averaging together 200 hundred traces in which each point was measured 3000 times for a total of 600,000 iterations per point. The error bars represent 10 standard deviations of the mean to demonstrate the scaling the ancilla measurement noise vs. measurement strength. Distinct differences in the behavior arise from experimental imperfections and their depedence on different qubit correlations. In particular the difference between $E(\beta_1, \beta_2)$ and $E(\alpha_1, \beta_2)$ or $E(\beta_1, \alpha_2)$ highlights the dependence of entanglement collapse on the measurement strength of both ancilla qubits.

original CHSH measurements. Due to differences in qubit coherence this does not necessarily occur at $\pi/4$, but at a slightly smaller angle. The individual BLGI correlator terms measured in this experiment along with theory curves accounting for these realistic rotations are plotted in Fig. D.4. The behavior of each individual term depends on the type of qubits being correlated. The term $E(\alpha_1, \alpha_2)$ holds roughly constant, close to the expected value of $1/\sqrt{2}$. $E(\alpha_1, \beta_2)$ and $E(\beta_1, \alpha_2)$ start close to zero, and converge to around ± 0.5. The behavior of $E(\beta_1, \beta_2)$ best matches expectations. It begins at 0 for strong ancilla measurement and converges near $1/\sqrt{2}$ at perfectly weak measurement, following a slightly s-shaped curve.

Table D.1: Parameters for the device when running the BLGI algorithm. f are frequencies. η is qubit nonlinearity. g is coupling strength. κ is resonator leakage rate.

	Q_0	Q_1	Q_2	Q_3
Qubit frequencies and coupling strengths				
f_{10}^{max} (GHz)	5.30	5.93	5.39	5.90
$\eta/2\pi$ (GHz)	-0.230	-0.216	-0.229	-0.214
f_{10}^{idle} (GHz)	4.53	5.42	4.67	5.55
f_{res} (GHz)	6.748	6.626	6.778	6.658
$g_{\mathrm{res}}/2\pi$ (GHz)	0.110	0.128	0.111	0.109
$g_{\mathrm{qubit}}/2\pi$ (MHz)	13.8		14.1	
$g_{\mathrm{qubit}}/2\pi$ (MHz)	14.5			
$1/\kappa_{\mathrm{res}}$ (ns)	675	69	555	30
Readout (RO) parameters				
RO error	0.015	0.004	0.067	0.007
Thermal $\|1\rangle$ pop.	0.013	0.007	0.028	0.01
RO pulse length (ns)	1000	300	1000	300
RO demodulation length (ns)	1000	300	1000	300
Qubit lifetime at idling point				
T_1 (μs)	26.3	24.7	39.2	21.3

D.3 Sample fabrication and characterization

Devices are fabricated identically to Ref. [**?**], and extensive calibration was documented in Ref. [81].

D.4 Device parameters

The device parameters are listed in table D.1. Note that the coupling rate g is defined such that strength of the level splitting on resonance (swap rate) is $2g$ (Ref. [109]).

Bibliography

[1] Albert Einstein, Boris Podolsky, and Nathan Rosen. Can quantum-mechanical description of physical reality be considered complete? *Phys. Rev.*, 47(10):777, 1935.

[2] John S Bell et al. On the einstein-podolsky-rosen paradox. *Physics*, 1(3):195–200, 1964.

[3] John F Clauser, Michael A Horne, Abner Shimony, and Richard A Holt. Proposed experiment to test local hidden-variable theories. *Phys. Rev. Lett.*, 23(15):880, 1969.

[4] Alain Aspect, Philippe Grangier, and Gérard Roger. Experimental realization of einstein-podolsky-rosen-bohm gedankenexperiment: a new violation of Bell's inequalities. *Phys. Rev. Lett.*, 49(2):91, 1982.

[5] Anthony J Leggett and Anupam Garg. Quantum mechanics versus macroscopic realism: Is the flux there when nobody looks? *Phys. Rev. Lett.*, 54(9):857, 1985.

[6] Clive Emary, Neill Lambert, and Franco Nori. Leggett–garg inequalities. *Reports on Progress in Physics*, 77(1):016001, 2014.

[7] Jan-Åke Larsson. Loopholes in Bell inequality tests of local realism. *J. Phys. A*, 47(42):424003, 2014.

[8] John F Clauser and Abner Shimony. Bell's theorem. experimental tests and implications. *Rep. Prog. Phys.*, 41(12):1881, 1978.

[9] Philip M Pearle. Hidden-variable example based upon data rejection. *Phys. Rev. D*, 2(8):1418, 1970.

[10] Jan-Åke Larsson. Bell's inequality and detector inefficiency. *Phys. Rev. A*, 57(5):3304, 1998.

[11] Mark M Wilde and Ari Mizel. Addressing the clumsiness loophole in a Leggett-Garg test of macrorealism. *Foundations of Physics*, 42(2):256–265, 2012.

[12] Karl Kraus. *States, effects and operations*. Springer, 1983.

[13] Yakir Aharonov, David Z Albert, and Lev Vaidman. How the result of a measurement of a component of the spin of a spin-1/2 particle can turn out to be 100. *Physical review letters*, 60(14):1351, 1988.

[14] M Hatridge, S Shankar, Mazyar Mirrahimi, F Schackert, K Geerlings, T Brecht, KM Sliwa, B Abdo, L Frunzio, Steven M Girvin, et al. Quantum back-action of an individual variable-strength measurement. *Science*, 339(6116):178–181, 2013.

[15] KW Murch, SJ Weber, C Macklin, and I Siddiqi. Observing single quantum trajectories of a superconducting quantum bit. *Nature*, 502(7470):211–214, 2013.

[16] SJ Weber, A Chantasri, J Dressel, AN Jordan, KW Murch, and I Siddiqi. Mapping the optimal route between two quantum states. *Nature*, 511(7511):570–573, 2014.

[17] Rusko Ruskov, Alexander N Korotkov, and Ari Mizel. Signatures of quantum behavior in single-qubit weak measurements. *Phys. Rev. Lett.*, 96(20):200404, 2006.

[18] Andrew N Jordan, Alexander N Korotkov, and Markus Büttiker. Leggett-Garg inequality with a kicked quantum pump. *Phys. Rev. Lett.*, 97:026805, 2006.

[19] Nathan S Williams and Andrew N Jordan. Weak values and the Leggett-Garg inequality in solid state qubits. *Phys. Rev. Lett.*, 100:026804, 2008.

[20] Agustin Palacios-Laloy, François Mallet, François Nguyen, Patrice Bertet, Denis Vion, Daniel Esteve, and Alexander N Korotkov. Experimental violation of a Bell/'s inequality in time with weak measurement. *Nat. Phys.*, 6(6):442–447, 2010.

[21] Michael E Goggin, Marcelo P Almeida, Marco Barbieri, Benjamin P Lanyon, Jeremy L O'Brien, Andrew G White, and Geoff J Pryde. Violation of the leggett–garg inequality with weak measurements of photons. *Proc. Natl. Acad. Sci. U.S.A.*, 108(4):1256–1261, 2011.

[22] Justin Dressel, CJ Broadbent, JC Howell, and AN Jordan. Experimental violation of two-party Leggett-Garg inequalities with semiweak measurements. *Phys. Rev. Lett.*, 106(4):040402, 2011.

[23] JP Groen, D Ristè, Lars Tornberg, J Cramer, PC De Groot, T Picot, Göran Johansson, and L DiCarlo. Partial-measurement backaction and nonclassical weak values in a superconducting circuit. *Phys. Rev. Lett.*, 111(9):090506, 2013.

[24] A Wallraff, DI Schuster, A Blais, L Frunzio, J Majer, MH Devoret, SM Girvin, and RJ Schoelkopf. Approaching unit visibility for control of a superconducting qubit with dispersive readout. *Phys. Rev. Lett.*, 95(6):060501, 2005.

[25] Justin Dressel and Alexander N Korotkov. Avoiding loopholes with hybrid Bell-Leggett-Garg inequalities. *Phys. Rev. A*, 89(1):012125, 2014.

[26] BL Higgins, MS Palsson, GY Xiang, HM Wiseman, and GJ Pryde. Using weak values to experimentally determine "negative probabilitie" in a two-photon state with bell correlations. *Phys. Rev. A*, 91(1):012113, 2015.

[27] R Barends, J Kelly, A Megrant, A Veitia, D Sank, E Jeffrey, TC White, J Mutus, AG Fowler, B Campbell, et al. Superconducting quantum circuits at the surface code threshold for fault tolerance. *Nature*, 508(7497):500–503, 2014.

[28] Evan Jeffrey, Daniel Sank, JY Mutus, TC White, J Kelly, R Barends, Y Chen, Z Chen, B Chiaro, A Dunsworth, et al. Fast accurate state measurement with superconducting qubits. *Phys. Rev. Lett.*, 112(19):190504, 2014.

[29] Claude Cohen-Tannoudji, Bernard Diu, and Franck Laloe. *Quantum Mechanics: Volume One*. John Wiley & Sons, 1977.

[30] Jens Koch, M Yu Terri, Jay Gambetta, Andrew A Houck, DI Schuster, J Majer, Alexandre Blais, Michel H Devoret, Steven M Girvin, and Robert J Schoelkopf. Charge-insensitive qubit design derived from the cooper pair box. *Physical Review A*, 76(4):042319, 2007.

[31] Matthias Steffen, John M Martinis, and Isaac L Chuang. Accurate control of josephson phase qubits. *Physical Review B*, 68(22):224518, 2003.

[32] Erik Lucero, Max Hofheinz, Markus Ansmann, Radoslaw C Bialczak, N Katz, Matthew Neeley, AD OConnell, H Wang, AN Cleland, and John M Martinis. High-fidelity gates in a single josephson qubit. *Physical review letters*, 100(24):247001, 2008.

[33] Erik Lucero, Julian Kelly, Radoslaw C Bialczak, Mike Lenander, Matteo Mariantoni, Matthew Neeley, AD OConnell, Daniel Sank, H Wang, Martin Weides, et al. Reduced phase error through optimized control of a superconducting qubit. *Physical Review A*, 82(4):042339, 2010.

[34] John M Martinis and Michael R Geller. Fast adiabatic qubit gates using only σ z control. *Physical Review A*, 90(2):022307, 2014.

[35] Edwin T Jaynes and Frederick W Cummings. Comparison of quantum and semiclassical radiation theories with application to the beam maser. *Proceedings of the IEEE*, 51(1):89–109, 1963.

[36] DI Schuster, Andreas Wallraff, Alexandre Blais, L Frunzio, R-S Huang, J Majer, SM Girvin, and RJ Schoelkopf. ac stark shift and dephasing of a superconducting qubit strongly coupled to a cavity field. *Physical review letters*, 94(12):123602, 2005.

[37] Appendix D.

[38] J Wenner, Yi Yin, Erik Lucero, R Barends, Yu Chen, B Chiaro, J Kelly, M Lenander, Matteo Mariantoni, A Megrant, et al. Excitation of superconducting qubits from hot nonequilibrium quasiparticles. *Physical review letters*, 110(15):150502, 2013.

[39] JE Johnson, C Macklin, DH Slichter, R Vijay, EB Weingarten, John Clarke, and I Siddiqi. Heralded state preparation in a superconducting qubit. *Phys. Rev. Lett.*, 109(5):050506, 2012.

[40] R. Barends, J. Kelly, A. Megrant, D. Sank, E. Jeffrey, Y. Chen, Y. Yin, B. Chiaro, J. Mutus, C. Neill, P. O'Malley, P. Roushan, J. Wenner, T. C. White, A. N. Cleland, and John M. Martinis. Coherent josephson qubit suitable for scalable quantum integrated circuits. *Phys. Rev. Lett.*, 111:080502, Aug 2013.

[41] David M Pozar. *Microwave engineering*. John Wiley & Sons, 2009.

[42] John Bertrand Johnson. Thermal agitation of electricity in conductors. *Physical review*, 32(1):97, 1928.

[43] RF Bradley. Cryogenic, low-noise, balanced amplifiers for the 300–1200 mhz band using heterostructure field-effect transistors. *Nuclear Phys. B-Proceedings Supplements*, 72:137–144, 1999.

[44] R Barends, J Wenner, M Lenander, Y Chen, RC Bialczak, J Kelly, E Lucero, P OMalley, M Mariantoni, D Sank, et al. Minimizing quasiparticle generation from stray infrared light in superconducting quantum circuits. *Applied Physics Letters*, 99(11):113507, 2011.

[45] Carlton M Caves. Quantum limits on noise in linear amplifiers. *Phys. Rev. D*, 26(8):1817, 1982.

[46] Stephen J Asztalos, G Carosi, C Hagmann, D Kinion, K Van Bibber, M Hotz, LJ Rosenberg, G Rybka, J Hoskins, J Hwang, et al. Squid-based microwave cavity search for dark-matter axions. *Phys. Rev. Lett.*, 104(4):041301, 2010.

[47] CA Regal, JD Teufel, and KW Lehnert. Measuring nanomechanical motion with a microwave cavity interferometer. *Nat. Phys.*, 4(7):555–560, 2008.

[48] R Vijay, DH Slichter, and I Siddiqi. Observation of quantum jumps in a superconducting artificial atom. *Phys. Rev. Lett.*, 106(11):110502, 2011.

[49] Lafe Spietz, Kent Irwin, Minhyea Lee, and José Aumentado. Noise performance of lumped element direct current superconducting quantum interference device amplifiers in the 4–8 ghz range. *Appl. Phys. Lett.*, 97(14):142502–142502, 2010.

[50] D Hover, Y-F Chen, GJ Ribeill, S Zhu, S Sendelbach, and R McDermott. Superconducting low-inductance undulatory galvanometer microwave amplifier. *Appl. Phys. Lett.*, 100(6):063503–063503, 2012.

[51] Byeong Ho Eom, Peter K Day, Henry G LeDuc, and Jonas Zmuidzinas. A wideband, low-noise superconducting amplifier with high dynamic range. *Nat. Phys.*, 2012.

[52] B Yurke, LR Corruccini, PG Kaminsky, LW Rupp, AD Smith, AH Silver, RW Simon, and EA Whittaker. Observation of parametric amplification and deamplification in a josephson parametric amplifier. *Phys. Rev. A*, 39(5):2519, 1989.

[53] I Siddiqi, R Vijay, F Pierre, CM Wilson, M Metcalfe, C Rigetti, L Frunzio, and MH Devoret. Rf-driven josephson bifurcation amplifier for quantum measurement. *Phys. Rev. Lett.*, 93(20):207002, 2004.

[54] MA Castellanos-Beltran and KW Lehnert. Widely tunable parametric amplifier based on a superconducting quantum interference device array resonator. *Appl. Phys. Lett.*, 91(8):083509–083509, 2007.

[55] M Hatridge, R Vijay, DH Slichter, John Clarke, and I Siddiqi. Dispersive magnetometry with a quantum limited squid parametric amplifier. *Phys. Rev. B*, 83(13):134501, 2011.

[56] Baleegh Abdo, Flavius Schackert, Michael Hatridge, Chad Rigetti, and Michel Devoret. Josephson amplifier for qubit readout. *Appl. Phys. Lett.*, 99(16):162506–162506, 2011.

[57] Nicolas Roch, Emmanuel Flurin, Francois Nguyen, Pascal Morfin, Philippe Campagne-Ibarcq, Michel H Devoret, and Benjamin Huard. Widely tunable, nondegenerate three-wave mixing microwave device operating near the quantum limit. *Phys. Rev. Lett.*, 108(14):147701, 2012.

[58] Archana Kamal, Adam Marblestone, and Michel Devoret. Signal-to-pump back action and self-oscillation in double-pump josephson parametric amplifier. *Phys. Rev. B*, 79(18):184301, 2009.

[59] John M Martinis, KB Cooper, R McDermott, Matthias Steffen, Markus Ansmann, KD Osborn, K Cicak, Seongshik Oh, DP Pappas, RW Simmonds, et al. Decoherence in josephson qubits from dielectric loss. *Phys. Rev. Lett.*, 95(21):210503, 2005.

[60] Manuel A Castellanos-Beltran, Kent D Irwin, Leila R Vale, Gene C Hilton, and Konrad W Lehnert. Bandwidth and dynamic range of a widely tunable josephson parametric amplifier. *Appl. Superconductivity, IEEE Transactions on*, 19(3):944–947, 2009.

[61] Tsuyoshi Yamamoto, K Inomata, M Watanabe, K Matsuba, T Miyazaki, WD Oliver, Y Nakamura, and JS Tsai. Flux-driven josephson parametric amplifier. *Appl. Phys. Lett.*, 93(4):042510–042510, 2008.

[62] I Siddiqi, R Vijay, F Pierre, CM Wilson, L Frunzio, M Metcalfe, C Rigetti, RJ Schoelkopf, MH Devoret, D Vion, et al. Direct observation of dynamical bifurcation between two driven oscillation states of a josephson junction. *Phys. Rev. Lett.*, 94(2):027005, 2005.

[63] VE Manucharyan, E Boaknin, M Metcalfe, R Vijay, I Siddiqi, and M Devoret. Microwave bifurcation of a josephson junction: Embedding-circuit requirements. *Phys. Rev. B*, 76(1):014524, 2007.

[64] EM Levenson-Falk, R Vijay, and I Siddiqi. Nonlinear microwave response of aluminum weak-link josephson oscillators. *Appl. Phys. Lett.*, 98(12):123115–123115, 2011.

[65] Peter K Day, Henry G LeDuc, Benjamin A Mazin, Anastasios Vayonakis, and Jonas Zmuidzinas. A broadband superconducting detector suitable for use in large arrays. *Nature*, 425(6960):817–821, 2003.

[66] SJC Yates, AM Baryshev, JJA Baselmans, B Klein, and R Gusten. Fast fourier transform spectrometer readout for large arrays of microwave kinetic inductance detectors. *Appl. Phys. Lett.*, 95(4):042504–042504, 2009.

[67] Yu Chen, D Sank, P O'Malley, T White, R Barends, B Chiaro, J Kelly, E Lucero, M Mariantoni, A Megrant, et al. Multiplexed dispersive readout of superconducting phase qubits. *Appl. Phys. Lett.*, 101(18):182601–182601, 2012.

[68] Prem Kumar, Orhan Aytür, and Jianming Huang. Squeezed-light generation with an incoherent pump. *Phys. Rev. Lett.*, 64:1015–1018, Feb 1990.

[69] JY Mutus, TC White, E Jeffrey, Daniel Sank, Rami Barends, Joerg Bochmann, Yu Chen, Zijun Chen, Ben Chiaro, Andrew Dunsworth, et al. Design and characterization of a lumped element single-ended superconducting microwave parametric amplifier with on-chip flux bias line. *Appl. Phys. Lett.*, 103(12):122602, 2013.

[70] R Vijay, DH Slichter, and I Siddiqi. Observation of quantum jumps in a superconducting artificial atom. *Phys. Rev. Lett.*, 106(11):110502, 2011.

[71] M Hatridge, S Shankar, M Mirrahimi, F Schackert, K Geerlings, T Brecht, KM Sliwa, B Abdo, L Frunzio, SM Girvin, et al. Quantum back-action of an individual variable-strength measurement. *Science*, 339(6116):178–181, 2013.

[72] Austin G Fowler, Matteo Mariantoni, John M Martinis, and Andrew N Cleland. Surface codes: Towards practical large-scale quantum computation. *Phys. Rev. A*, 86(3):032324, 2012.

[73] KM Sundqvist, Seckin Kintas, Michael Simoen, Philip Krantz, Martin Sandberg, CM Wilson, and Per Delsing. The pumpistor: A linearized model of a flux-pumped superconducting quantum interference device for use as a negative-resistance parametric amplifier. *Appl. Phys. Lett.*, 103(10):102603–102603, 2013.

[74] Sundqvist and Per Delsing. Negative-resistance models for parametrically flux-pumped superconducting quantum interference devices. *arxiv.org*, page 1311.2063, 2013.

[75] C Eichler and A Wallraff. Controlling the dynamic range of a josephson parametric amplifier. *arXiv:1305.6583*, 2013.

[76] RW Klopfenstein. A transmission line taper of improved design. *Proc. IRE*, 44(1):31–35, 1956.

[77] Appendix B.

[78] Leonardo Ranzani, Lafe Spietz, Zoya Popovic, and Jose Aumentado. A 4: 1 transmission-line impedance transformer for broadband superconducting circuits. *Applied Superconductivity, IEEE Transactions on*, 22(5):1500606–1500606, 2012.

[79] C. Eichler, Y. Salathe, J. Mlynek, S. Schmidt, and A. Wallraff. Quantum-limited amplification and entanglement in coupled nonlinear resonators. *Phys. Rev. Lett.*, 113:110502, Sep 2014.

[80] O-P Saira, JP Groen, J Cramer, M Meretska, G De Lange, and L DiCarlo. Entanglement genesis by ancilla-based parity measurement in 2d circuit qed. *Phys. Rev. Lett.*, 112(7):070502, 2014.

[81] J Kelly, R Barends, AG Fowler, A Megrant, E Jeffrey, TC White, D Sank, JY Mutus, B Campbell, Yu Chen, et al. surfancecode. *Nature*, 519(7541):66–69, 2015.

[82] JY Mutus, TC White, Rami Barends, Yu Chen, Zijun Chen, Ben Chiaro, Andrew Dunsworth, Evan Jeffrey, Julian Kelly, et al. Strong environmental coupling in a josephson parametric amplifier. *Appl. Phys. Lett.*, 104(26):263513, 2014.

[83] O Yaakobi, L Friedland, C Macklin, and I Siddiqi. Parametric amplification in josephson junction embedded transmission lines. *Phys. Rev. B*, 87(14):144301, 2013.

[84] JA Armstrong, N Bloembergen, J Ducuing, and PS Pershan. Interactions between light waves in a nonlinear dielectric. *Phys. Rev.*, 127(6):1918, 1962.

[85] Appendix C.

[86] AL Cullen. A travelling-wave parametric amplifier. *Nature*, 1958.

[87] PK Tien. Parametric amplification and frequency mixing in propagating circuits. *J. Appl. Phys.*, 29(9):1347–1357, 1958.

[88] see supplemental information at link for furthur discussion of the sample, measurement techniques, and mathmatical assumptions.

[89] S Wahlsten, S Rudner, and T Claeson. Parametric amplification in arrays of josephson tunnel junctions. *Appl. Phys. Lett.*, 30(6):298–300, 1977.

[90] MJ Feldman, PT Parrish, and RY Chiao. Parametric amplification by unbiased josephson junctions. *J. Appl. Phys.*, 46(9):4031–4042, 1975.

[91] B Yurke, ML Roukes, R Movshovich, and AN Pargellis. A low-noise series-array josephson junction parametric amplifier. *Appl. Phys. Lett.*, 69(20):3078–3080, 1996.

[92] O Yaakobi, L Friedland, C Macklin, and I Siddiqi. Parametric amplification in josephson junction embedded transmission lines. *Phys. Rev. B*, 87(14):144301, 2013.

[93] C Macklin and et al. *in preparation*, 2014.

[94] C Bockstiegel, J Gao, MR Vissers, M Sandberg, S Chaudhuri, A Sanders, LR Vale, KD Irwin, and DP Pappas. Development of a broadband nbtin traveling wave parametric amplifier for mkid readout. *J. Low. Temp. Phys.*, pages 1–7, 2014.

[95] Kevin O'Brien, Chris Macklin, Irfan Siddiqi, and Xiang Zhang. Resonant phase matching of josephson junction traveling wave parametric amplifiers. *Phys. Rev. Lett.*, 113(15):157001, 2014.

[96] GJ Dolan. Offset masks for lift-off photoprocessing. *Appl. Phys. Lett.*, 31(5):337–339, 1977.

[97] Aaron D O'Connell, M Ansmann, Radoslaw C Bialczak, Max Hofheinz, Nadav Katz, Erik Lucero, C McKenney, Matthew Neeley, Haohua Wang, Eva M Weig, et al. Microwave dielectric loss at single photon energies and millikelvin temperatures. *Appl. Phys. Lett.*, 92(11):112903, 2008.

[98] Rolf Landauer. Shock waves in nonlinear transmission lines and their effect on parametric amplification. *IBM Journal of Research and Development*, 4(4):391–401, 1960.

[99] Nicolas Roch, Mollie E Schwartz, Felix Motzoi, Christopher Macklin, Rajamani Vijay, Andrew W Eddins, Alexander N Korotkov, K Birgitta Whaley, Mohan Sarovar, and Irfan Siddiqi. Observation of measurement-induced entanglement and quantum trajectories of remote superconducting qubits. *Physical review letters*, 112(17):170501, 2014.

[100] Shmuel Marcovitch and Benni Reznik. Testing Bell inequalities with weak measurements. *arXiv preprint arXiv:1005.3236*, 2010.

[101] Markus Ansmann, H Wang, Radoslaw C Bialczak, Max Hofheinz, Erik Lucero, M Neeley, AD O'Connell, D Sank, M Weides, J Wenner, et al. Violation of bell's inequality in josephson phase qubits. *Nature*, 461(7263):504–506, 2009.

[102] Ivana Kovacic and Michael J Brennan. *The Duffing equation: nonlinear oscillators and their behaviour*. John Wiley & Sons, 2011.

[103] Rajamani Vijayaraghavan. *Josephson bifurcation amplifier: Amplifying quantum signals using a dynamical bifurcation*. 2008.

[104] Robert H Cole. Time domain reflectometry. *Annual Review of Physical Chemistry*, 28(1):283–300, 1977.

[105] Govind P Agrawal. *Nonlinear fiber optics*. Academic press, 2007.

[106] Saptarshi Chaudhuri, Kent Irwin, and Jiansong Gao. Simulation and analysis of superconducting traveling-wave parametric amplifiers. *arXiv preprint arXiv:1412.2372*, 2014.

[107] Saptarshi Chaudhuri and Jiansong Gao. Comment on" parametric amplification in josephson junction embedded transmission lines". *arXiv preprint arXiv:1308.2951*, 2013.

[108] J. Kelly, R. Barends, B. Campbell, Y. Chen, Z. Chen, B. Chiaro, A. Dunsworth, A. G. Fowler, I.-C. Hoi, E. Jeffrey, A. Megrant, J. Mutus, C. Neill, P. J. J. O'Malley, C. Quintana, P. Roushan, D. Sank, A. Vainsencher, J. Wenner, T. C. White, A. N. Cleland, and John M. Martinis. Optimal quantum control using randomized benchmarking. *Phys. Rev. Lett.*, 112:240504, Jun 2014.

[109] In refs. [27] and [108], the convention was used where $g/2\pi$ is the swap rate. Here we use $2g/2\pi$ as the swap rate, in accordance with others in the field.